Implementation of Fast Airborne Synthetic Aperture Radar Simulation

HUI-SHUN KAO

2004

A Dissertation Submitted to the Department of Electrical Engineering, University of Cape Town. In Partial Fulfillment of the Requirement of the Degree of Master of Science in Electrical Engineering

Declaration

I declare that this dissertation is my own, unaided work. It is being submitted in partial fulfillment for the Degree of Master of Science in Electrical Engineering in the University of Cape Town. It has not being submitted before for any degree or examination in any other university.

Signature of Author ____________________

Cape Town
January 2003

Acknowledgements

I wish to express my true and deep appreciation to my supervisor, Dr. Wilkinson. Without his constant help and encouragements, the completion of this dissertation would not have been possible.

To my family, the spiritual support of my life, thank you.

Special thanks to all my colleagues at the DIP Laboratory who share their knowledge and happiness to me. I would also like to say thank you to Professor Inggs to provide me with valuable information for the simulation data.

Abstract

Synthetic Aperture Radar (SAR) is a powerful tool to map the topographic data of the Earth surface regardless of weather and optical illumination effects. Since nowadays the modern aircraft may be fitted with SAR facility, the aim of this dissertation is to develop fast algorithms for a fast or real-time like SAR simulator which could aid in airplane pilot training. In this dissertation, a geometric approach to the topographic mapping of SAR was studied and then implemented using computer software. In particular, the effect of antenna flight path on the outcome of Synthetic Aperture Radar was examined.

To generate necessary data, a SAR simulator was implemented. The geometric relationship between radar sensor and imaging terrain forms the central core of the software. A technique to find a set of sample points on the observed scene in the antenna zero-Doppler plane was examined. A method to work out the scattering points (center position of resolution cell) was examined, which is based on the derived sample point set and the vector geometry of the observation system. Using the information of scattering points as a basis, techniques to work out radar layover and shadow maps, slant range area to ground range area conversion, backscattering coefficients of scene, SAR power image and signal distribution were derived. The values of backscattering coefficient were based on the empirical data from Ulaby and Dobson's work.

Finally, the computer generated results were compared to real SAR results to verify the accuracy and realism of the simulator. A performance evaluation for the processing speed of the simulator was discussed.

Contents

List of Figures

List of Tables

List of Symbols and Acronyms

Symbols

h	Height above (Earth) ground
ϕ	Radar beam radiation angle
V	Radar velocity
R	Distance of range
c	Propagation speed of EM wave
P_r	Received power
P_t	Transmit power
G	Antenna gain
R_{max}	Maximum allowable range to detect a returned signal
λ	Wavelength
σ	Radar Cross Section
σ^0	Backscattering coefficient
S_{min}	Minimum detectable power for the receiver
d	Antenna length (dimension length)
f_0	Carrier frequency
R_e	Radius of earth
γ	Angle between imaging target and radar position at the center of Earth
θ	Angle between surface normal and radar line-of-sight
R_g	Ground range
r_s	Slant range resolution
r_g	Ground range resolution
r_a	Azimuth resolution
B	Bandwidth
$v_t(t)$	Radar transmitted signal (time-domain)
$v_r(t)$	Radar received signal (time-domain)
$V_r(f)$	Radar received signal (frequency-domain)
$\zeta(t)$	Impulse response of the observed scene (time-domain)
$\zeta(f)$	Impulse response of the observed scene (frequency-domain)
$v(t)$	Output of I-Q downconverter (time-domain)
$V(f)$	Output of I-Q downconverter (frequency-domain)
$p(t)$	Base-banded version of the transmitted signal (time-domain)

$P(f)$	Base-banded version of the transmitted signal (frequency-domain)
t_d	Time delay of the transmitted signal
$H_{dc}(f)$	Ideal de-convolution filter
δt	Radar resolution
T	Time duration for a transmitted signal
K	Chirp rate
Δf	Total sweep frequency of a Chirp
R_0	Closest distance of range to the target (at zero-Doppler plane)
x	Distance between R and R_0
$\varphi(x)$	Two-way phase delay
D	The synthetic aperture length
A_{SR}	Slant range area
A_{GR}	Ground area
A	Signal's amplitude
Φ	Signal's phase
$\mathrm{I}(t)$	The real part of the received signal
$\mathrm{Q}(t)$	The imaginary part of the received signal
$n_I(t)$	The real part of the noise
$n_Q(t)$	The imaginary part of the noise
σ_I	Standard deviations of the received signal's real part
σ_Q	Standard deviations of the received signal's imaginary part
σ_{nI}	Standard deviations of the noise's real component
σ_{nQ}	Standard deviations of the noise's imaginary component
$E\{\|V\|^2\}$	Expected received power
$\vec{s}$	Sample points
$\vec{p}$	Scattering centres
$\vec{r}$	Range vector from antenna to $\vec{p}$
$\vec{n}$	Surface normal of $\vec{p}$
$\vec{P}_N$	Sample point on the DEM
a	Ratio for finding the sample point $\vec{s}$
$\vec{k}$	Segment constituted by $\vec{P}_N$
$\vec{A}$	Position of radar (vector)
b	Ratio for finding the scattering centre $\vec{p}$
Δr	Slant range spacing
α	Angle between the Nadir and radar line-of-sight
$\mathrm{SNR}_{\text{mid-swath}}$	Signal-to-Noise ratio at mid-swath
$E\{\|n(t)\|^2\}$	Receiver noise power

Acronyms

CPU	Central Processing Unit
DEM	Digital Elevation Model
EM	Electro-Magnetic
FM	Frequency Modulation
InSAR	Interferometric Synthetic Aperture Radar
OS	Operating System
PRF	Pulse Repetition Frequency
PRI	Pulse Repetition Interval
RCS	Radar Cross Section
SAR	Synthetic Aperture Radar
SLAR	Side-Looking Aperture Radar
SNR	Signal-to-Noise Ratio

Chapter 1

Introduction

Until the invention of new techniques such as photography and radar imaging, the topographic data that were broadly used in geological and geographical applications are acquired using conventional surveying techniques. These kinds of method are usually time consuming and tend to be erroneous by human faults.

The use of Synthetic Aperture Radar (SAR) system to obtain high quality images of the Earth surface begins in the last few decades. The system has been carried in both airborne and satellite platform. SAR is essentially a special type of side-looking imaging radar, where the fundamental difference of SAR and the ordinary side-looking imaging radar is that SAR has the capability to process the returned signals from the observed scene in such a way to achieve high azimuth resolution. As a member of imaging radar, SAR is also an active device that provides its own source to illuminate the desired targets. In contrast with passive imaging devices such as camera, where the source of illumination to the targets is light (usually from the sun) and therefore can only be used in the presence of light, Synthetic Aperture Radar can work in the environment without light source. Further more, by employ the electromagnetic (EM) wave as the imaging medium, SAR is capable of penetrating the clouds and fogs in the atmosphere; this property makes SAR extremely useful on mapping areas that were constantly governed by poor weather conditions. As an example, the Amazon area in South America has been covered by heavy clouds and fogs nearly all year round, where optical imaging is difficult to achieve in this area. As a result of this, the employment of SAR offered a choice to be used in mapping this area.

The properties described above have made Synthetic Aperture Radar in many applications such as monitoring the oceanographic trend, pattern of deforestation, urbanization, astronomical observation and Digital Elevation Modeling using Synthetic Aperture Radar Interferometry (InSAR) [7].

This introductory chapter starts with brief overview of Synthetic Aperture Radar follows by the objectives of this dissertation. A brief historical background of the development of SAR will be given as well as the scope of this thesis project. Finally the plan of development will be given.

1.1 Overview of Imaging Radar and SAR

Before a detail analysis on how SAR works, it is worthwhile to look at the imaging geometry of radar, as depicted in figure 1.1. The side-looking radar pass across the scene to be observed, emitting EM waves and receive the echoes to produce a photo-like image of the ground. The direction from the radar sensor to the targets is known as range where the direction of radar along the flight path is usually referred to as the azimuth.

Conventional side-looking radar obtains the range resolution by emitting a short EM pulse to the target; a finer range resolution may be acquired using pulse compression techniques; the azimuth resolution is obtained by the radiation of a narrow energy beam. Since the beamwidth of radar is a function of antenna dimension and frequency, this implied the larger the antenna, the narrower the beamwidth and thus the better azimuth resolution [12]. However the use of a very large antenna is practically undesirable and will increases the expense to build it. Synthetic Aperture Radar was therefore developed because of the increasing demand on higher azimuth resolution in the ground mapping area. As the name Synthetic Aperture suggests, SAR generate a virtually very large antenna from a much smaller antenna by means of signal processing. A much more details on how this is achieved will be discussed later in this dissertation.

Several constraints on imaging the ground terrain have been imposed due to the side-looking geometry. These include layover and shadowing effects. The layover effect occurred when two or more areas in the scene fall into the same range from radar. Furthermore, because the radar views the ground terrain at an angle (typically 20 to 80 degrees), some of the area in the mountainous area may be hidden from

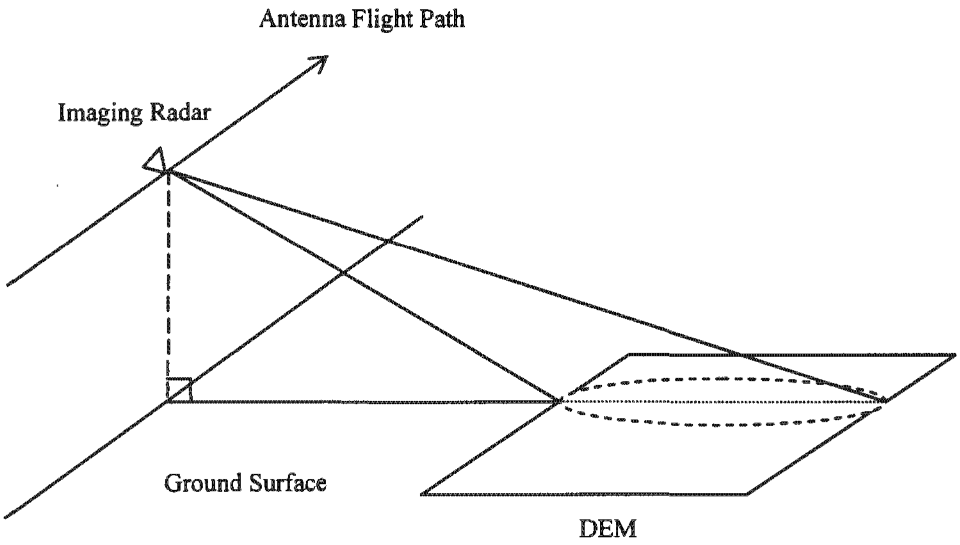

Figure 1.1 Imaging geometry of radar

direct line-of-sight, this phenomenon is usually known as shadowing.

1.2 Objectives of Dissertation

The effects of radar fly trajectory on the outcomes of Synthetic Aperture Radar can vary significantly even on imaging the same ground region. Due to this aspect, an application concerned about airplane pilot training using SAR as the support tool was initiated. With a SAR mounted on the airplane, the trainer can compare the simulated outcomes of a specified trajectory with actual airborne SAR images obtained by the pilot trainee, and determined the stability of the trainee on controlling the airplane according to these image data. Therefore the primary objective of this dissertation is to derive mathematic algorithms for a fast or perhaps "real-time" like airborne SAR simulator and examine the effect of the antenna fly trajectory on the output SAR images. The word "real-time" in this dissertation should refer to the processing speed of the simulator that is capable to catch up the speed of a real world airplane as the aircraft scanned through the scene. To accomplish this task, a number of project goals are listed below:

- Study the theory of side-looking image radar, these include the geometry of the imaging system as well as the signal processing part of the system. In particular, the method by which Synthetic Aperture Radar synthesizes a very large aperture by means of signal processing will be examined as well as some fundamental properties of SAR image.

- Derive algorithms from the radar imaging geometry that will be used for constructing the SAR simulator. A key point in the design of a real-time simulator is the trade-off between simulation accuracy and execution speed, and the algorithms developed should incorporate these considerations.

- Prototype the SAR simulators using Matlab based on the derived algorithms and if possible, rewrite the simulation in C program language for program executing speed improvement.

- Examine the outputs of simulation, which includes relationship between backscattering coefficient and incident angle, I-Q channel of the radar system and the effect of antenna fly trajectory on the resulting SAR images.

- Draw conclusions on the stability of the algorithms in regard to the speed of execution of the simulator, and the geometric and radiometric accuracy of the produced SAR images for the intended purpose of the simulator.

1.3 Brief Literature on SAR Simulator at 90's

As a preparation for the Synthetic Aperture Radar simulation design, the functionality of several SAR simulators designed recently by various institutions around the globe were examined.

The SAR simulation has favored the scientists and the engineers in many ways which include:

- For planning of future radar missions where the effects of different mapping and setup configuration can be studied by the simulation prior the initiate of the mission [24].

- The studies concerning noise and clutter rejection in the Synthetic Aperture Radar system and may contribute towards optimizing the SAR system parameters [23].

- Examining the effect of the radar illumination angle with the imaging ground and the terrain relief on SAR images [24]

The SAR image simulation can be classified into three types according to the method of implementation [24], namely the coherent system simulation, the incoherent image simulation and the SAR image-based simulation.

A coherent system simulator involves simulation of the raw SAR signal, i.e. the signal received by SAR before any processing. The simulated signal then passes through an appropriate SAR signal processor to produce the simulated SAR images. Examples of the coherent simulator were the SARAS Raw Signal Simulator by G. Franceschetti et al. [23] and the Ocean SAR Raw Signal Simulator by G. Franceschetti et al. [25].

The incoherent system simulation employs the radar incident angle to the observed scene and the Digital Elevation Model (DEM) of the ground terrain to compute the pixel values of the output SAR image directly, without simulation of the raw SAR signal. That means that this type of simulation does not model how SAR processing the returned signal and therefore greatly reduces the computing time. Examples of this type of simulation were L. Wray's SAR Image Simulator for Interferometry [3] and the SAR Image Simulation by M. Gelautz et al. [24].

The SAR image-based simulation combines an incoherent simulation with the information extracted from an actual SAR image to compute the simulated SAR images of another imaging configuration [24]. An example of this is the Image Based SAR Product Simulation by G. Domik et al. [26].

1.4 Brief History of SAR

In 1952 Wiley developed a radar he called a "Doppler beam-sharpening" system. This system operated at 75 MHz frequency, where some kind of beam sharpening technique is required if a reasonable azimuth resolution is to be achieved with antenna small enough to be carried on an aircraft. This was the first system developed of what we now know as Synthetic Aperture Radar [5].

Since then, many efforts were done on improving the system performance and hardware of SAR with the primary application in geological studies. The first commercialized SAR, the synthetic aperture GEMS was made available after 1969 [5], which based upon military radar. In the same period, a new technique derived from SAR was used for the observation of Venus [20]. The system utilizes the phase information contained in the radar images for reconstruction of topographic height map, a technique known as Synthetic Aperture Radar Interferometry (InSAR).

The proposals for using SAR as a satellite Earth observation tool were made in 1960s. However the first of such radar to fly in the space, the oceanographic satellite Seasat was launched in 1978.

Recent development of SAR includes the launched of ESR-1 satellite into the space by European Space Agency in 1991 and RADARSAT-1 satellite by Canada in 1995. A series of very flexible airborne systems carrying multi-frequency SAR were developed by several institutions, one of the most influential example might be the AirSAR by NASA/JPL [2].

1.5 Scope and Limitation

The primary data sources for simulation comparison were C-band, ERS-2 SAR images from the European Space Agency, with the imaging area at the Cape Peninsula region in South Africa. Moreover, the simulation DEM real data was provided by "Chief Directorate of Surveys and Mapping, Department of Land Affairs, South Africa".

1.6 Plan of Development

The remainders of this dissertation are organized as follow:

- Chapter 2 deals with the basics of side-looking imaging radar and the natural constraints that accompany the side-looking geometry such as layover and shadowing effects. The signal processing of the received signals as well as the pulse compression techniques used to improve the range resolution will be examine in detail.

- Chapter 3 introduces the fundamental theory and properties of SAR. One major concern in this chapter is the focusing technique on the azimuth direction, i.e. how synthetic aperture radar synthesize a large antenna using signal processing. Properties of SAR image such as backscattering model used to interpret the receiving signals and the noise-like speckle phenomenon are studied in detail.

- Chapter 4 derives the algorithms that will be use to build up the simulation. These algorithms are based mainly on the imaging geometry of SAR, and with the help of empirical observation of the backscattering coefficient model.

- Chapter 5 discusses in detail about the images produces by the simulation. Images include layover and shadow maps, the backscattering coefficient map, the received power map and a noise-like speckle map. The effects of different antenna flight path on SAR images are examined by comparing several images from different flight trajectories. The speed of the algorithms for "real-time" application is analyzed by examining the execution time of the simulator.

- Chapter 6 draws conclusions based on the findings of this project and recommends future work.

- Appendix A displays a sample log file from the simulation.

- Appendix B illustrates a complete simulation results (images) of the SAR simulator.

- Appendix C presents the full empirical data of backscattering coefficient used in this dissertation.

Chapter 2

Fundamental Theory of Imaging Radar

The fundamental principles of Synthetic Aperture Radar are based mainly upon the conventional side-looking aperture radar (SLAR). By understanding the operations of how an SLAR works, one can get some basic concepts of SAR as well as what radar imaging is. Therefore the contents of this chapter are mainly to introduce the theory of the SLAR and provide as a preparation for further study of SAR.

The chapter begins with an examination of the SLAR geometric layout and formulates some basic equations corresponding to the side-looking geometry. The constraints due to the geometry layout will be introduced. It is then follow by the discussion of the signal processing part of radar system, which includes both the transmitter and receiver. The last part of the chapter deal with the pulse compression techniques that have being used to improve the slant range resolution of radar.

2.1 SLAR Imaging Model

The Side-Looking Aperture Radar (SLAR) is a high resolution radar that aims its antenna on one side of the airborne platform along the flight path. Short pulses of EM wave are radiated within a constant interval (Pulse Repetition Interval PRI) and the echoes received are subjected to a sequence of signal processing operation to form the radar image. The following section will look at the geometric part of the system.

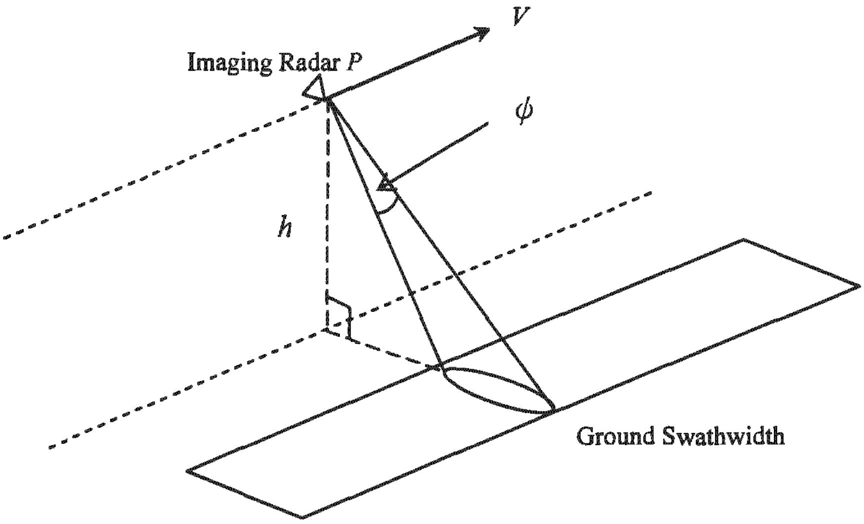

Figure 2.1 Basic imaging geometry of SLAR.

2.1.1 Side-Looking Geometry

The basic imaging geometry of an SLAR is shown in Figure 2.1. The radar moving with velocity V at altitude h is illuminating the ground terrain with pulses of EM radiation. The echoes were received sometimes later and sampled as function of delay time t. Since the propagation speed of signal is known, the range of the target R can be work out by:

$$t = 2R / c \qquad \text{or} \qquad R = ct / 2 \tag{2.1}$$

where c is the propagation speed of EM radiation (i.e. speed of light). The minimum and maximum ranges of the radar are referred to as near range and far range respectively. The difference of near and far range is the swathwidth, as show in Figure 2.1. Since the transmission and reception can not be overlap, the swathwidth is restricted by a constraint imposed by the Pulse Repetition Frequency (PRF) of the system [2], this is:

$$\text{slant swathwidth} < c / (2 \times \text{PRF}) \tag{2.2}$$

A further limitation might be imposed to the swathwidth because of the energy concern in the range direction. This is depicted below by the standard radar equation [1]:

$$P_r = \frac{P_t G^2 \lambda^2 \sigma}{(4\pi)^3 \times R^4} \tag{2.3}$$

$$R_{\max} = \left(\frac{P_t G^2 \lambda^2 \sigma}{(4\pi)^3 \times S_{\min}} \right)^{1/4} \tag{2.4}$$

where R_{max} is the maximum allowable range for the antenna to detect the return signal, P_t is the transmitted power, G is the antenna gain, λ is the wavelength, σ is the RCS of the object and S_{min} is the minimum detectable power for the receiver. It was shown that the maximum allowable range R_{max} in (2.4) is being limited by some radar parameters; a particular emphasis in (2.4) is the parameter S_{min}, the minimum detectable power for the receiver antenna. This means once a limited distance (range) has been exceed, the receiver might not be able to detect the greatly attenuated echo from the target.

A typical antenna installed on the radar has dimensions $d_a \times d_e$, where the subscripts a and e denoted azimuth and elevation respectively. The dimensions of antenna represent an important factor in mapping the scene because they determine the size of the radar illumination area on the ground. The relationship between antenna length d and the beamwidth is:

$$\phi = \lambda / d \qquad \text{[radians]} \tag{2.5}$$

$$\lambda = c / f_0 \qquad \text{[metres]} \tag{2.6}$$

where ϕ is the radiation angle in radians and λ is the wavelength of radar. Notice this relationship holds for both the azimuth and elevation lengths of antenna. A cross-section of the side-looking geometry is depicted in Figure 2.1. The layout in Figure 2.1 also implied that an airborne radar system was employed, where the Earth surface can be treated as flat. This condition is true even for long-distance airborne radar imaging. However, applications of radar imaging using the satellite platform represent a slightly different geometric layout. Because the Earth is an ellipsoid, the observation system must account for the curvature of Earth surface and a spherical geometry must be used. Since the spherical geometry of the observation system can

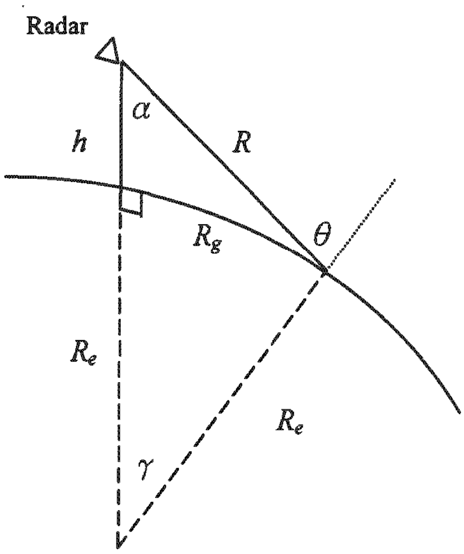

Figure 2.2 Cross-section of spherical (round Earth) imaging geometry.

be simplified into flat-earth geometry if the effect of the Earth curvature was taken off, we shall examine the spherical geometry first. This spherical geometry is based on the layout described in [2].

Figure 2.2 depicted a cross-sectional view of the round-earth radar system. From this layout, one can obtain the basic relations between each parameters:

$$R = (R_e + h)\frac{\sin\gamma}{\sin\theta} \qquad (2.7a)$$

$$R^2 = R_e{}^2 + (R_e{}^2 + h)^2 - 2R_e\,(R_e + h)\cos\gamma \qquad (2.7b)$$

$$R_g = R_e\,\gamma \qquad (2.7c)$$

$$\gamma = \theta - \alpha \qquad (2.7d)$$

$$\sin\alpha = \frac{R_e}{R_e + h}\sin\theta \qquad (2.7e)$$

where R_e is the radius of earth, h is the height above the ground, γ is the angle between target and radar position at the center of Earth, θ is the angle between surface normal and radar line-of-sight and R_g is the ground range. The above equations can be reduced to flat-earth approximations if the effect of Earth is being taken away. (2.7a, b) then become:

$$R = R_g / \sin\theta \tag{2.8a}$$

$$R^2 = h^2 + R_g^{\ 2} \tag{2.8b}$$

2.1.2 Image Resolution of SLAR

In the field of ground mapping using radar imaging, the resolution of resulting radar images is an important concern in the chosen application fields. The resolution is the capability of radar to display the returned signals from two point targets, separated by the resolution distance as two responses [18]. In side-looking aperture radar, the resolution [14] is functions of beamwidth of antenna and the system bandwidth, which were summarized by the equations:

$$r_s = c \ / \ 2B \tag{2.9}$$

$$r_g = \frac{dR_g}{dR} = \frac{r_s}{\sin\theta} \tag{2.10}$$

$$r_a = \phi_a R \tag{2.11}$$

The above three equations indicate slant range resolution r_s, ground range resolution r_g and azimuth resolution r_a respectively. Notice that the ground range resolution r_g changes nonlinearly across the swathwidth as θ, the incident angle between transmitted signal and surface normal varies. To illustrate the influence of this non-linearity on the produced radar image, a diagram that describes the specific situation is shown in Figure 2.3, which indicates that great differences on the ground range resolution will occur if θ were varying considerably. As an example, a radar operating with incident angles between 20 to 80 degrees would have a ground range resolution at far range (80 degrees) that is a factor of about 0.35 of the near ground range resolution. In radar image, such changes in resolution can have serious consequences. Terrain features and objects that are clearly distinguishable at far range

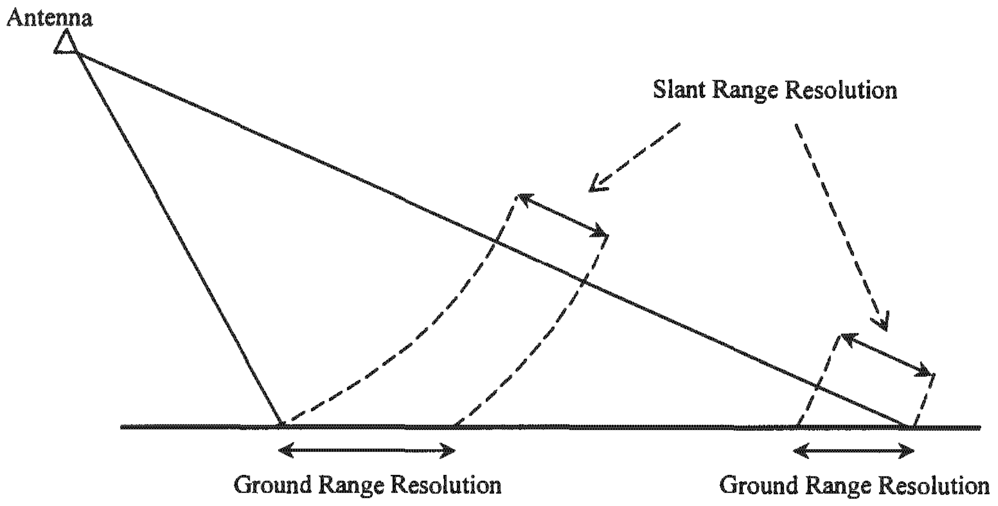

Figure 2.3 Illustration of non-linear variation of ground range across the swathwidth.

can become nearly invisible at near range. However, this effect is less significant for long-range airborne systems, such as one in the military applications.

2.1.3 Limitations on Side-Looking Geometry

Mapping the ground terrain in the side-looking manner result in some natural constraints that were related to the imaging geometry [2] [19]. The first limitation is a phenomenon called layover. Layover occurs when two or more areas on the imaging surface falls into the same slant range bin from radar, which make the radar receiver to 'treat' the echoes from these areas as one single returned from a single scatterer on the ground, i.e. point scatterers were overlaid on top of each other. Layover usually happens in areas with sudden change on the steepness of the terrain slope such as a very steep mountain or a mountain ridge. The effect of layover will result a much stronger echo received by the antenna, because instead of receiving echo from a single area, the returned signal is a combination of several areas on the ground. The second constraint occurs when radar views the terrain at an angle (typically between 20 to 80 degrees) and some of the areas in the hilly region are being hidden from the direct line-of-sight of radar, a phenomenon known as shadowing. As a contrast to layover region on the ground, shadowing often results in very weak returned or even no

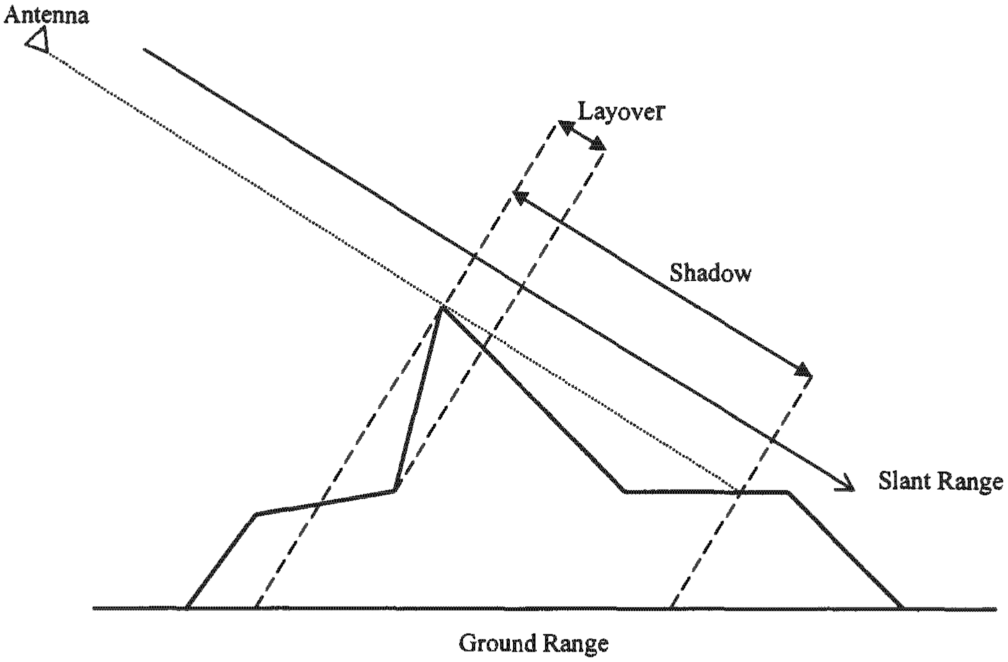

Figure 2.4 Illustration of the shadowing and layover effects.

returned to the radar receiver. Both of these two effects are shown in Figure 2.4; notice that it is possible for a ground region to have both layover and shadowing effects occurring simultaneously.

2.2 Radar Signal Processing

Having considered the geometric part of the radar system, we shall now shift the attention to the signal processing part of the radar system. The model for the radar described in this section was mainly based on the treatment by Wilkinson [9]. Figure 2.5 shows a simple model of a radar system that was commonly used in radar signal processing. It contains a transmitter which generates the EM signal and emits it to the targets and receives the echoes some time later. These returned signals are then subjected to a series of signal processing operation to form the final result.

Transmitter

The transmitted signal is a burst of RF energy modeled by the analytic signal $v_t(t)$.

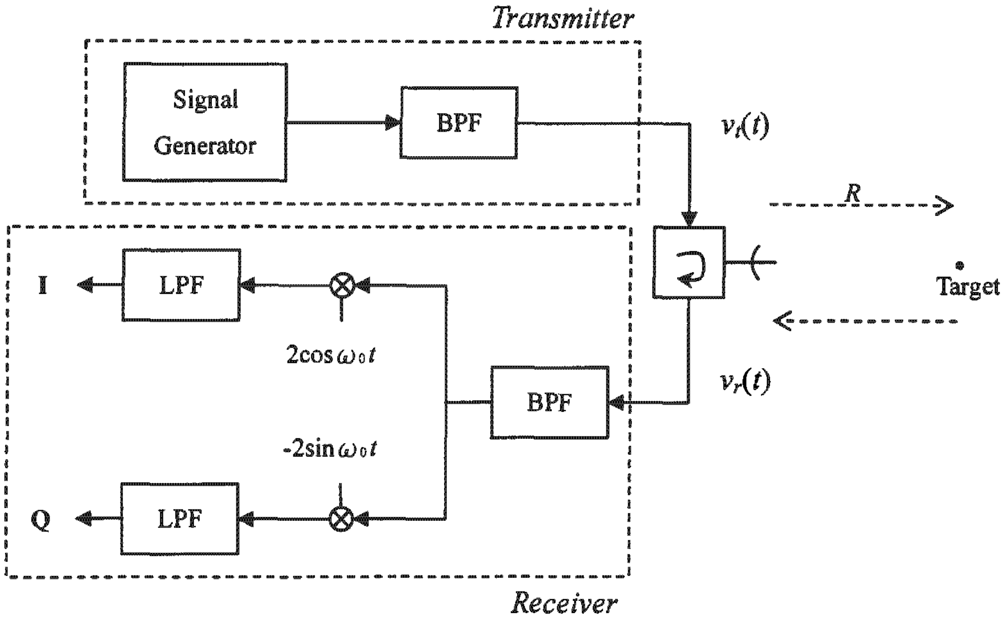

Figure 2.5 A simple model of radar system.

Receiver

The receiver signal $v_r(t)$ can be represented as the analytic (complex) signal in time and frequency domain by:

$$v_r(t) = v_t(t) * \zeta(t) \tag{2.12a}$$

$$V_r(f) = V_t(f)\, \zeta(f) \tag{2.12b}$$

where ζ is the impulse response of the scene (or targets). This is equivalent to model the response from the scene as a linear system where the convolution in the time domain is equivalent to the multiplication in the frequency domain. The output of the I-Q downconverter $v(t)$ is:

$$v(t) = v_r(t)\, exp(-j2\pi f_0 t) \Leftrightarrow V_r(f + f_0) \tag{2.13}$$

For special case with $v_t(t) = p(t)\, exp(j2\pi f_0\, t)$ where $p(t)$ is the basebanded representation of the transmitted pulse, the output of I-Q downconverter $V(f)$ in the frequency domain becomes:

$$V(f) = V_r(f+f_0) = V_t(f+f_0)\,\zeta(f+f_0)$$

$$= P([f+f_0]-f_0)\,\zeta(f+f_0)$$

$$= \zeta(f+f_0)\,P(f) \qquad (2.14)$$

(2.14) indicates that the output of the I-Q downconverter is simply a basebanded version of the transmitted pulse, i.e. shifted in the frequency domain. A series of diagrams were shown in Figure 2.6 to illustrate the transmitted-received signal as well as this frequency shift in each stage.

It is clear from (2.12) that all information about the scene is carried by $\zeta(f)$. To extract $\zeta(f)$ from (2.14), we can apply an ideal de-convolution filter $H_{dc}(f)$:

$$H_{dc}(f) = \frac{1}{P(f)} \qquad \text{for } -B/2 < f < B/2\text{, zero elsewhere} \qquad (2.15)$$

The band-limited reconstructed spectrum is

$$V(f) = \zeta(f + f_0)\ \mathrm{rect}(f / B) \qquad (2.16a)$$

$$v(t) = \zeta(t)\ exp(-j2\pi f_0\ t) * [B\frac{\sin(\pi Bt)}{(\pi Bt)}] \qquad (2.16b)$$

where rect(f / B) is a rectangular function with centre at origin. The term within the bracket in (2.17b) is also known as the sinc (or "Sa) function, and is plotted in Figure 2.7. It is noted from Figure 2.7 that the zero occurred at the integer multiples of $1/B$ from the peak of main-lobe. The band-limited output from the ideal de-convolution filter is thus the convolution of the target's impulse response $\zeta(t)$ and the sinc function. Notice the factor $exp(-j2\pi f_0\, t)$ in (2.16b) gives the phase over the main-lobe as:

$$\Phi = -2\pi f_0\, t = -2\pi\,\frac{c}{\lambda}\cdot\frac{2R}{c} = \frac{-4\pi R}{\lambda} \qquad (2.17)$$

In the case described by Figure 2.7, the radar resolution is defined as the "half-power" or the "3 dB" point from the main-lobe as:

$$\delta t \text{ at 3dB} = 0.89/B \qquad (2.18)$$

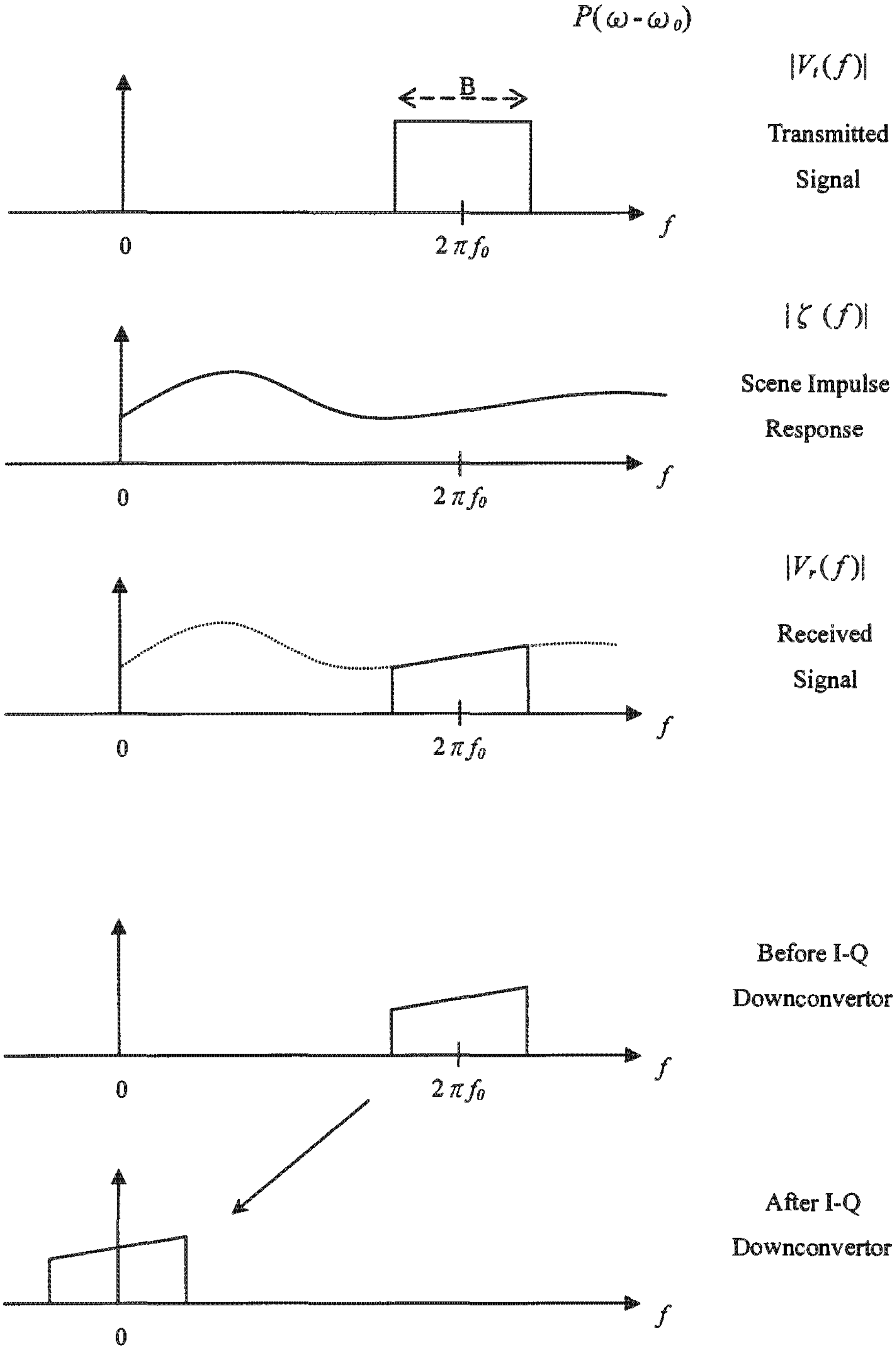

Figure 2.6 Frequency domain representation of the signal in various stages.

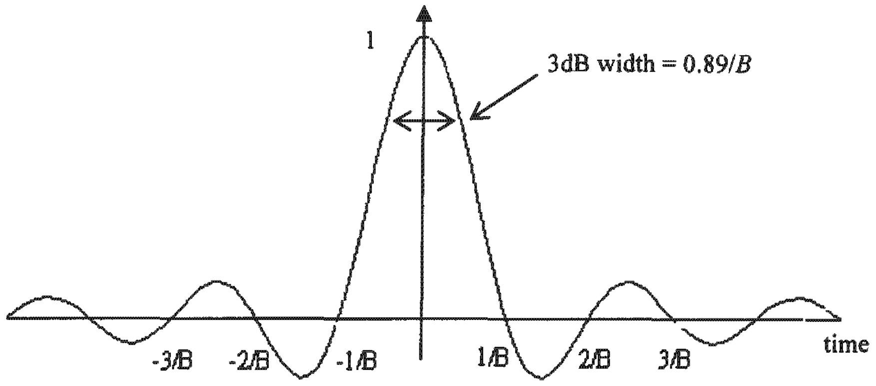

Figure 2.7 Illustration of the sinc($\pi B t$) function (also known as the Sa function).

where B is the bandwidth of the transmitted pulse. Aside from the main-lobe, the side-lobes illustrated in Figure 2.7 represent a "smearing" to the basebanded impulse response, which limits the visual resolvability of the close by point target. The magnitude of the side-lobes can be decreased by using a windowing function at the price of main-lobe broadening [9].

2.3 Pulse Compression and the Linear FM Pulse

In the field of ground mapping using image radar, the range resolution is obtained by emitting short pulses of EM wave towards to the targets. However, a compromise exists between the pulse width and the transmitted energy for the imaging radar:

- Short transmitted monochrome pulse gives fine range resolution. Equation (2.9) indicates that the range resolution is a function of bandwidth. The common relationship is that the system bandwidth of radar is inversely proportional to the transmitted pulsewidth.

- Long pulse width increases the overall transmitted energy, i.e. greater the received power that increases the maximum detection range and the signal-to-noise (SNR) ratio at the receiver, but at a cost of range resolution.

The above relationships illustrate that to obtain a finer range resolution; a price of decreasing the radar's imaging range performance must be paid. Pulse compression

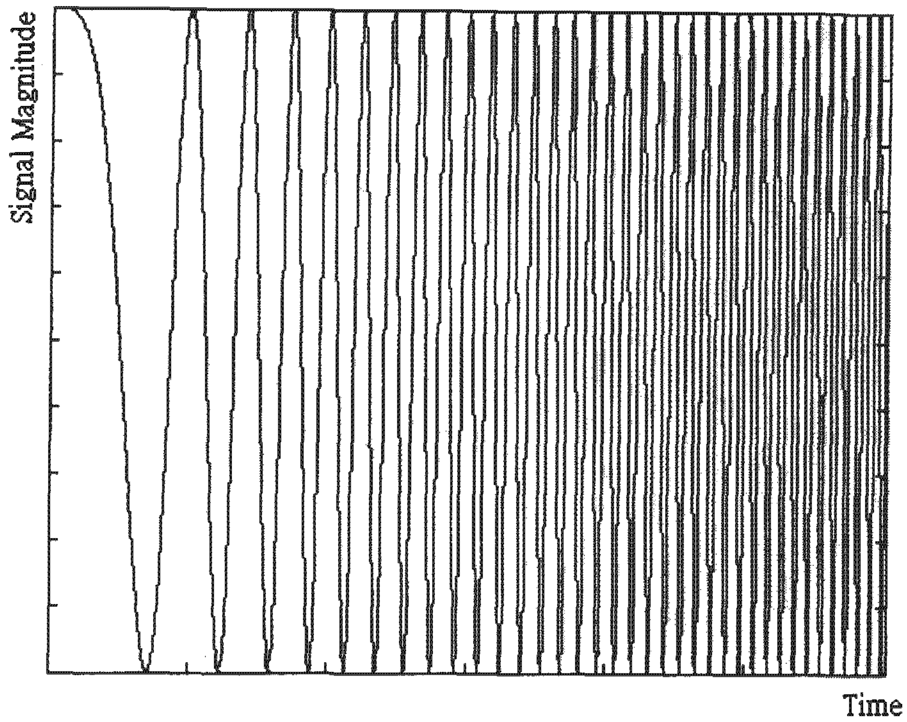

Figure 2.8 Illustration of the Linear FM Pulse.

techniques were developed under these circumstances to achieve high range resolution while maintain a suitable transmitted energy. There are generally two type of pulse compression techniques used in the modern signal processing. Brief descriptions are given below:

Discrete Coded Waveform – a long transmitted pulse is conducted from a series of short pulse segments. Coding is usually accomplished by change the phase of the carrier frequency from segment to segment. For more detail, please refer to [22].

Linear FM (Frequency Modulation) Pulse – In this technique, the instantaneous frequency of the transmitted pulse is linearly swept over a bandwidth Δf, as shown in Figure 2.8 and also known as the Chirp signal. It is this second method on which we focus in this section.

A Chirp signal may be modeled by a transmitted signal v_t with duration T [9]:

$$v_t(t) = \mathrm{rect}\,(\,t\,/\,\mathrm{T}\,)\,exp(2\,\pi f_0\,t\;+1/2\,\mathrm{K}t^2) \qquad (2.19)$$

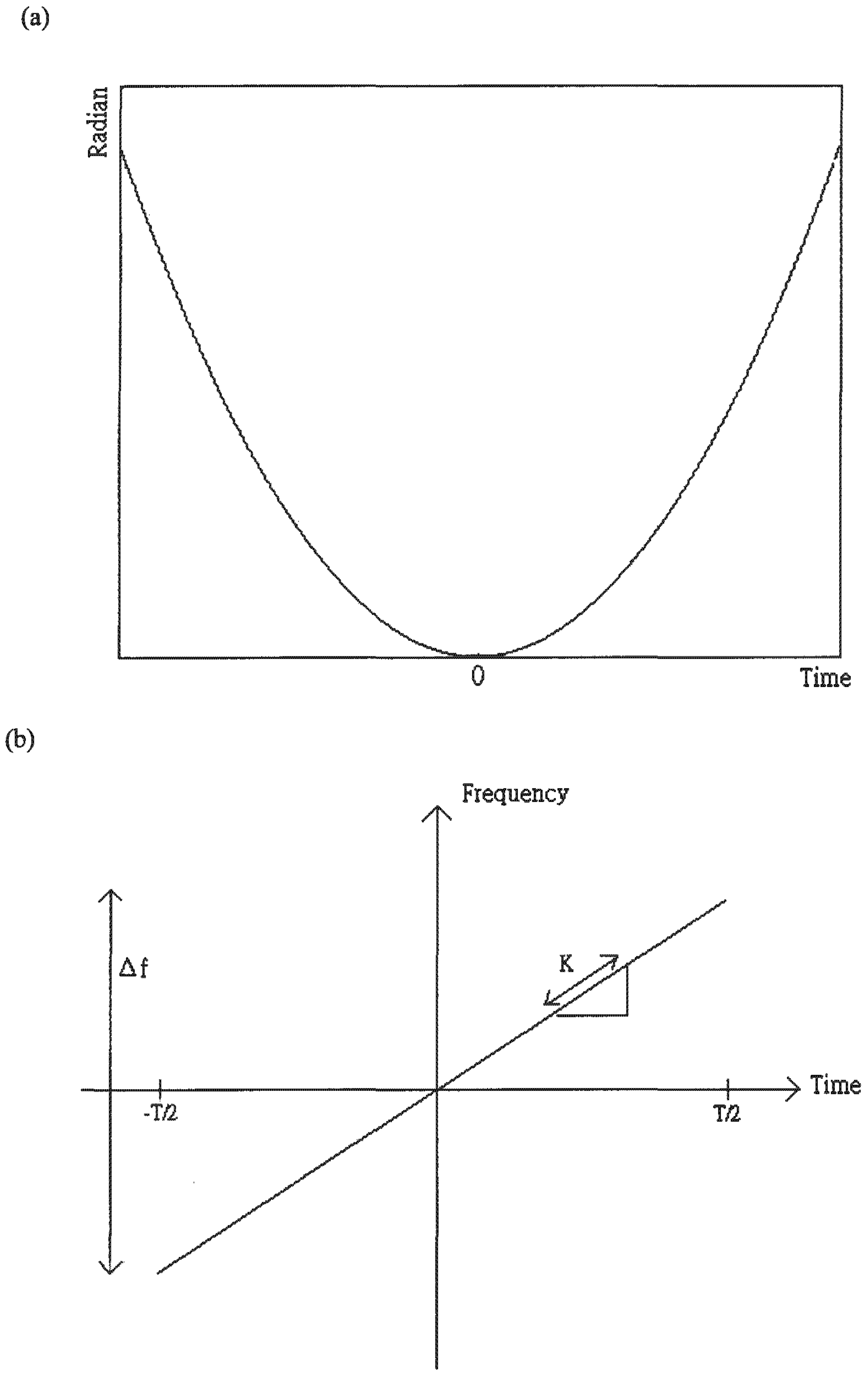

Figure 2.9 Plots of the basebanded chirp signal (a) the phase and (b) the frequency.

where rect() is a rectangle waveform. The phase of this signal is:

$$\varphi(t) = 2\pi f_0 t + 1/2Kt^2 \qquad \text{[radians]} \qquad (2.20)$$

and the instantaneous frequency of the signal is given by the time derivative of the phase:

$$f(t) = 2\pi f_0 + Kt \qquad \text{[Hz]} \qquad (2.21a)$$

$$\text{or} \qquad = (f_0 + Kt) / 2\pi \qquad \text{[Hz]} \qquad (2.21b)$$

It is clear from (2.21b) that the total sweep frequency Δf or the bandwidth for a time duration T is:

$$\Delta f = (K\,T) / 2\pi \qquad \text{[Hz]} \qquad (2.22a)$$

$$= K\,T \qquad (2.22b)$$

where K is the chirp rate in Hz s^{-1}. Figure 2.9 illustrates the corresponding phase and the sweep frequency for the linear FM pulse with positive chirp rate. Notice that an important factor that characterizes the chirp signal is the compression ratio [2]. For the original pulse length T and the compressed pulse length which is approximately equal to $1/B \sim 1/\Delta f$, the compression ratio is:

$$\text{compression ratio} = T/\delta t = T/(1/\Delta f) = K\,T^2 \qquad (2.23)$$

This factor is also known as the time-bandwidth product, the ratio that indicated the resolution after processing to the original pulse length.

Chapter 3

Principles of SAR Imaging

Having looked at the fundamental properties of the side-looking radar, we now shift our attention into the principle theory of Synthetic Aperture Radar. How SAR synthesizes a long antenna array by using a small physical antenna is an important focus in this chapter as well as the speckle phenomenon from mapping areas of distributed target.

The chapter begin with discussion of the SAR synthesize technique for the azimuth dimension. It is followed by the backscattering model used to describe the reflective property of various ground terrain types. Finally the chapter ends up with discussion of the so-called speckle phenomenon in the radar imaging field.

3.1 Azimuth Synthesize Technique of SAR

The fundamental difference between Synthetic Aperture Radar and ordinary side-looking radar is on the signal processing part of the azimuth dimension. Recall from Chapter 2, equation (2.11) showed that the side-looking radar simply take the return from the illuminated ground patch at distance R away as its azimuth resolution. As a result of this, coarse azimuth resolution arose when a small antenna is employed for long distance mapping. For example, the ERS-1 satellite employed an antenna with 10 meters azimuth length gives a beamwidth less than 1 degree, which although small, nevertheless makes a footprint of a few kilometers on the ground at a distance of about 850 km (and thus the azimuth resolution). SAR was developed because of the need for finer azimuth resolution. In this section, we will examine how SAR

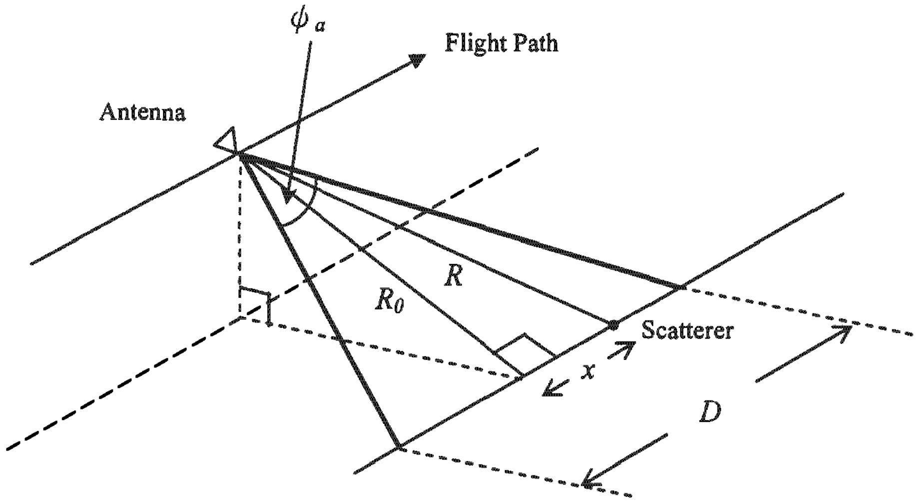

Figure 3.1 The flat earth imaging geometry of SAR.

achieves this by signal processing through the received signals. The model discussed in this section is based on Oliver and Quegan's work [2].

Consider a flat earth imaging geometry of SAR, as depicted in Figure 3.1. The antenna flies along track while passing over a point scatterer on the ground. The idea behind the synthesize technique of SAR is the exploitation of nearly quadratic range variations of the point scatterer as the antenna beam sweeps over it. An instant relation which can be seen from Figure 3.1 is:

$$R^2 = R_0^2 + x^2 \tag{3.1}$$

where R is the distance between antenna and the point scatterer, R_0 denotes the closest distance approach to the ground (at zero Doppler plane) and x is the distance in between them. For a narrow beamwidth, $x << R_0$ and (3.1) can be approximated as:

$$R \approx R_0 + x^2/2R_0 \tag{3.2}$$

The corresponding two-way phase delay at the carrier frequency is:

$$\varphi(x) = -\frac{4\pi R_0}{\lambda} - \frac{4\pi x^2}{\lambda 2R_0} \tag{3.3}$$

and the rate of change of the phase with respect to distance is given by:

$$\frac{d\varphi}{dx} = -\frac{4\pi x}{\lambda R_0} \tag{3.4}$$

Compare the above equations with the chirp signal discussed in Chapter 2, we find that these are equivalent to the linear FM in the distance variable. Applying the results of linear FM from Chapter 2 we have a spatial bandwidth:

$$B_x = \frac{1}{2\pi}\frac{4\pi}{\lambda R_0} D \tag{3.5}$$

where D is the synthetic aperture length indicated on Figure 3.1; using the properties $D = \phi_a R_0$ and $\phi_a = \lambda / d_a$, we have:

$$B_x = \frac{2}{\lambda R_0}\frac{\lambda}{d_a} R_0 = \frac{2}{d_a} \tag{3.6}$$

and so the azimuth resolution is:

$$r_a = 1/B_x = d_a/2 \tag{3.7}$$

where d_a is the antenna azimuth dimension. Equation (3.7) shows a critical result that indicates the azimuth resolution of SAR is half of the antenna azimuth dimension and independent from imaging range and radar wavelength. It further indicates that smaller antenna gives a better resolution. One question might arise of why not using a very small antenna to optimize the azimuth resolution. The answer is that other parameters of the imaging system depend on the antenna size and are subject to mutual constraints in order to achieve appropriate imaging result. These aspects include PRF, transmitted pulsewidth and swathwidth.

Figure 3.2 [21] shows two SAR images that illustrate a point scatterer before and after SAR focusing technique. Consider a point target on the ground; a long antenna array is collected by moving the antenna along a flight path, while transmitting, receiving

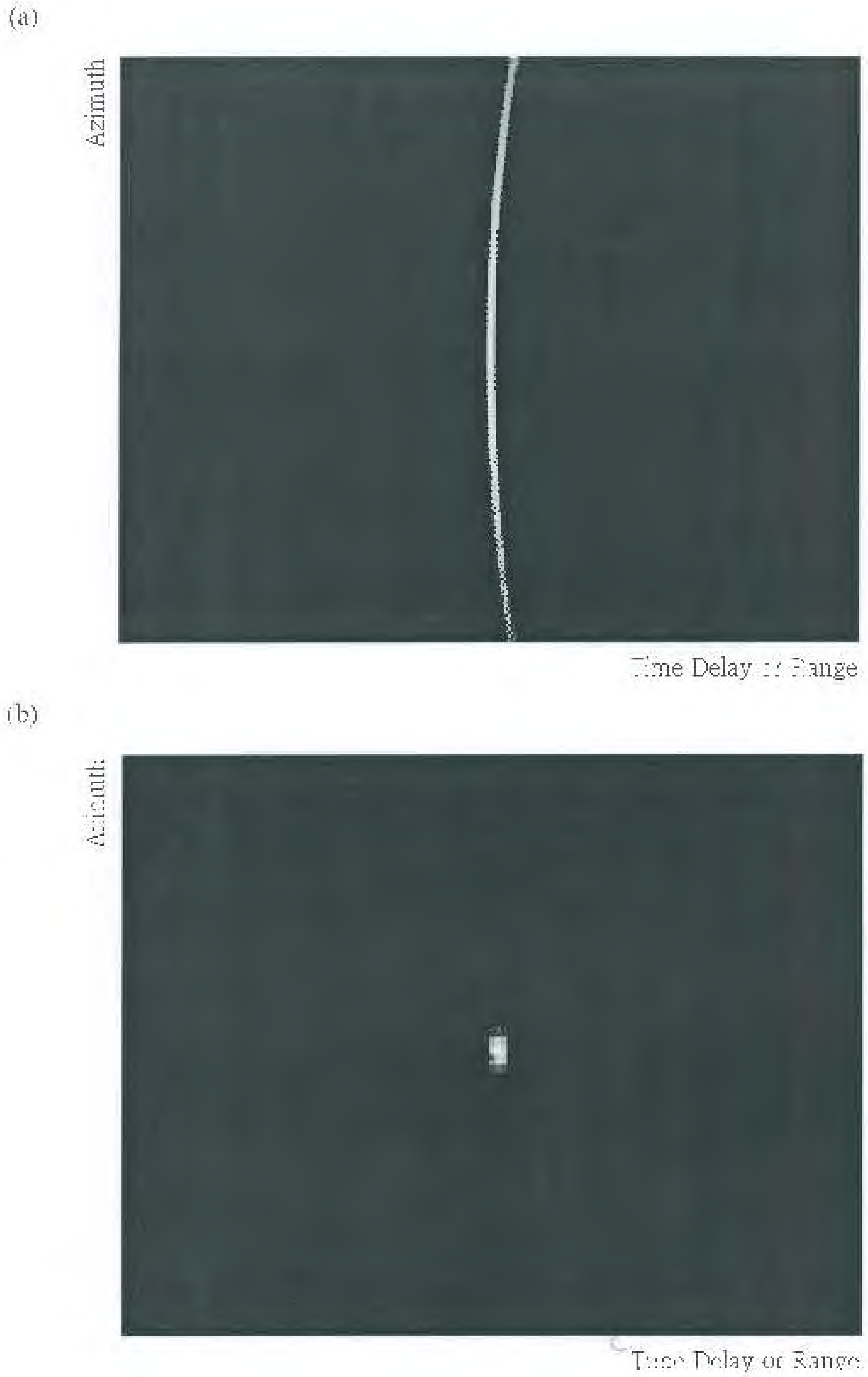

Figure 3.2 SAR image for a point target (a) unfocused SAR image (b) focused SAR image.

Type of Radar Resolution	Real Aperture Radar	Synthetic Aperture Radar
Azimuth Resolution	$r_a = \phi_a R$	$r_a = d_a/2$
Slant Range Resolution	$r_s = c / 2B$	$r_s = c / 2B$

Table 3.1 Comparison of azimuth and range resolution for Synthetic Aperture Radar and Real Aperture Radar.

the return signals at specific location of the flight path. One can clearly seen that the return signals form a nearly quadratic range arc, as shown in Figure 3.2(a); this is because the antenna is approaching the target first then moving away at late stage. Focusing of these responses is through a correlation action [15] and the final focused image is shown in Figure 3.2(b).

Also on Table 3.1 is a comparison of the azimuth and range resolution for the two different type of radar discussed in this dissertation. The difference between these two radar types is on the azimuth resolution.

3.2 Backscattering Model of the Scene

No matter how sophisticated a radar is, all radars can only measure the change of the transmitted RF waveform when the signal interacts with the physical object that scattered the energy back to the radar receiver [11]. Perhaps the most important parameter that dominates the variation of the transmitted signal is the Radar Cross Section (RCS) of the physical body, a parameter which described how the imaging target was 'seen' by the radar at a particular wavelength and polarization. The return power P_r that the radar received is given by the following equation:

$$P_r = \frac{P_t G^2 \lambda^2 \sigma}{(4\pi)^3 \times R^4} \tag{3.8}$$

where σ is the RCS of the imaging object. Since the transmitted power P_t, antenna gain G and the radar wavelength λ were constants, equation (3.8) can be simplified for mapping different type of objects at same range R as:

$$P_r = C\,\sigma \tag{3.9}$$

where C is a constant describe the rest of parameters in (3.8). The radar cross section can be further subdivided into the backscattering coefficient σ^0, and the ground area of the imaging resolution cell A_{GR} as:

$$\sigma = \sigma^0 A_{GR} \tag{3.10}$$

It is obvious from the above equations that if an accurate model of backscattering coefficient and thus the RCS of the scene were available, a realistic simulation of the radar received power will be possible. Notice that RCS of a given target is strictly a characteristic of the target itself, and its orientation with respect to the transmitter receiver system [6].

In order to model an accurate backscattering coefficient for the observed scene, two different scattering models were considered, namely the theoretical scattering model and the empirical scattering model.

Theoretical Model of Backscattering Coefficient - this model is based on mathematic calculation to describe the incident radar pulse and the scattering surface of the scene to work out the expected received energy. However, these models were restricted on their applicability to generalize the imaging surface, and were not adopted for use in this dissertation [3].

Empirical Model of Backscattering Coefficient – this model is based on Ulaby and Dobson's work [8]. The empirical model for backscattering coefficient was obtained by real world radar observation of distributed target through various type of ground terrain at different signal incident angles, as shown in Figure 3.3. The model can be further categorized into the use of different waveform polarizations and carrier frequencies.

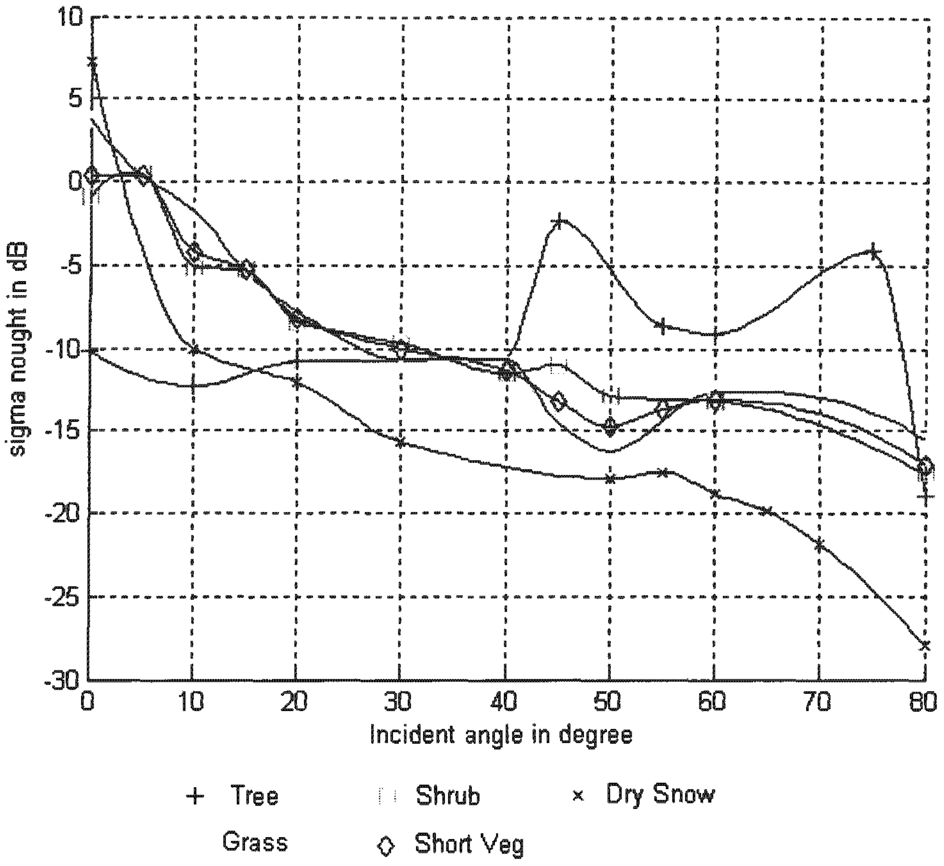

Figure 3.3 Empirical model of the backscattering coefficient (σ^0) for various terrain types at C band, VV polarization.

3.3 Application of Speckle

When imaging an area that is populated with distributed target, a noise-like variation arises on the resulting radar image, as shown in Figure 3.4. This noise-like quality is referred to as speckle, a phenomenon due to the phase interference effect from scatterers within a distributed target. Before we examine this effect, we should first understand what is mean by distributed target. A distributed target is a homogeneous region contains a large number of randomly positioned point scatterers in the resolution cell. The concept of distributed target can be apply to model most natural scatterers such as forest, grass land or rock surface.

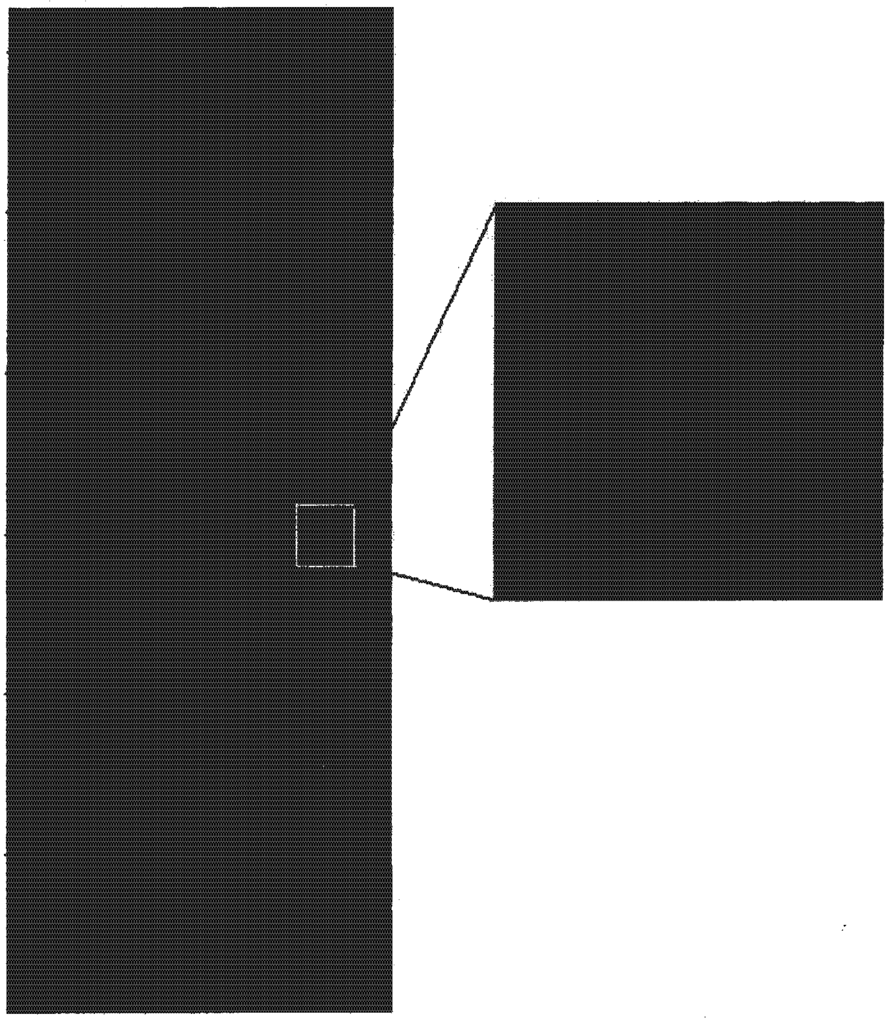

Figure 3.4 Illustration of speckle on a simulated Cape Peninsula SAR image.

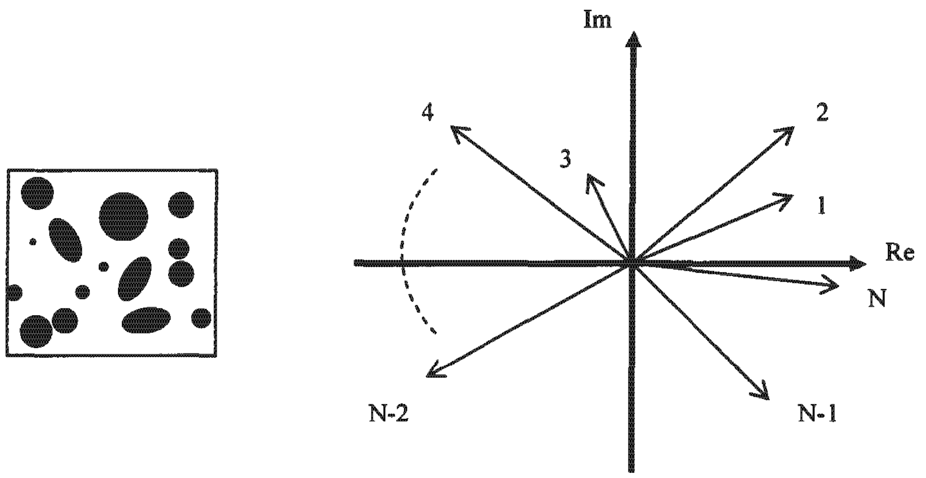

Figure 3.5 An example of discrete point scatterers within a resolution cell and the corresponding phasor diagram.

For a remote sensing imaging radar, the size of an individual scatterer on the ground is usually much smaller than the size of the resolution cell. Due to the randomly orientation and irregular shape of the ground surface elements, the returns from multiple scatterers within a resolution cell add up incoherently to give a net backscattering coefficient which is a random variable as illustrated by the vectors in Figure 3.5. The return signal in a resolution cell is thus:

$$A\, exp(j\Phi) = \sum_{k=1}^{N} A_k\, exp(j\Phi_k) \qquad (3.11)$$

where A is the signal's amplitude and Φ is the phase. It is clear from (3.11) that each scatterer contributes a phase and amplitude change for the backscattered signal. Thus two adjacent ground patches with the same scattering properties can produce different backscattered signal due to their different geometric layout and thus appear differently on the produced radar image. In fact, speckle can be understood as an interference effect in which the principal source of the noise-like quality of the observed data is the distribution of the phase term Φ_k [8].

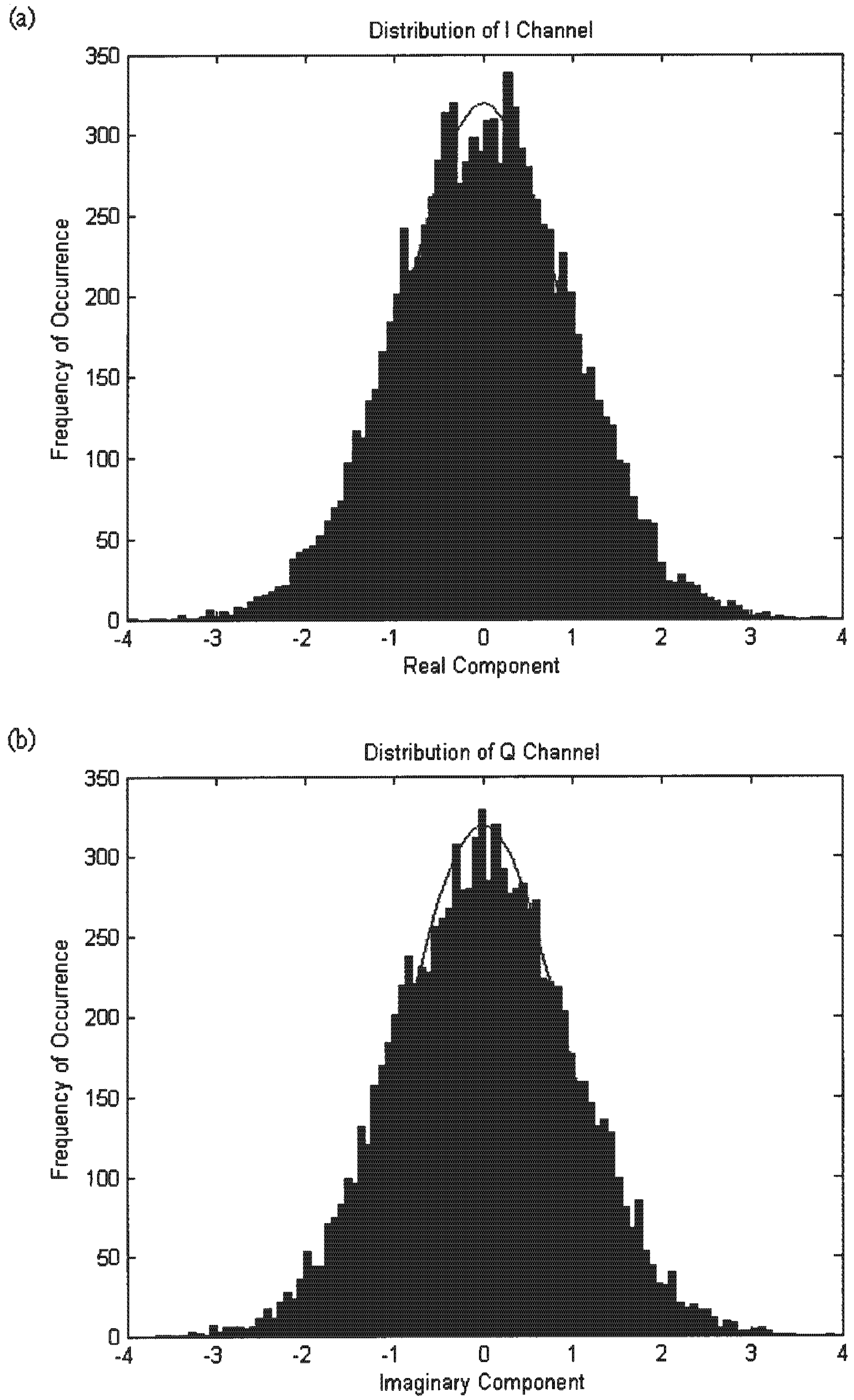

Figure 3.6 Signal distribution of (a) In-phase component (b) Quadrature-phase component generated by Matlab simulation.

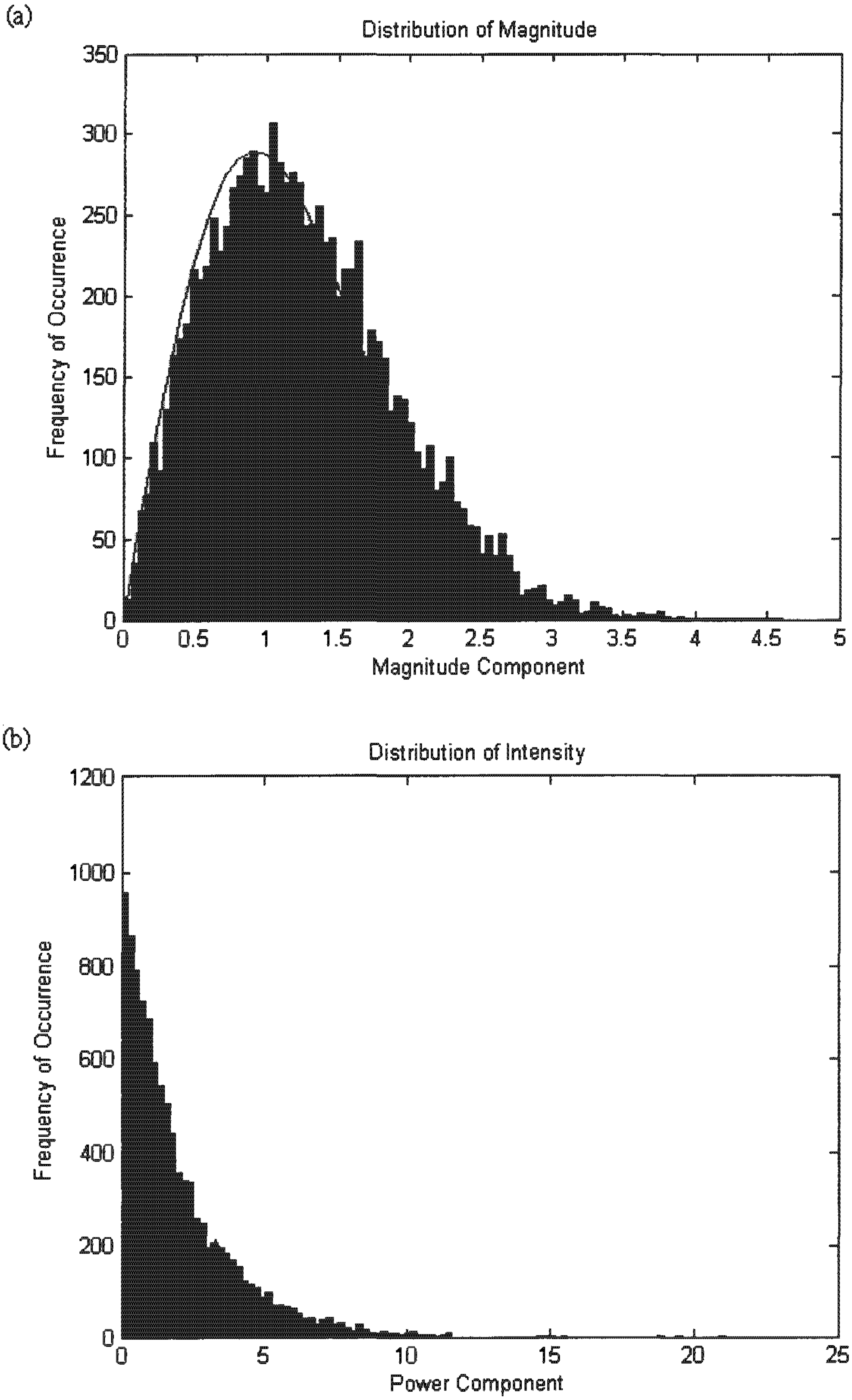

Figure 3.7 Signal distribution of (a) magnitude component (b) intensity component.

There are scattering statistics concerned about the signal distribution of the returns from distributed target. Brief descriptions were given below:

- The observed in-phase and quadrature-phase component are Gaussian distributed random variables with zero mean, as shown in Figure 3.6. These histograms were generated by Matlab simulation with the solid line in the figure represents the Gaussian probability density function with zero mean.

- The amplitude A have a Rayleigh distribution, as shown in Figure 3.7(a). Again, this histogram was made from Matlab simulation with a solid line indicated the Rayleigh distribution.

- The intensity or the power A^2 has a negative exponential distribution, as indicated in Figure 3.7(b). The figure was generated by Matlab simulation which shows a negative exponential function pattern.

3.4 Additive Receiver Noise

In a real world Synthetic Aperture Radar imaging, noise is always present in the radar received signal. The source of this noise is a combination of both the machine noise generated by the radar sensor and the thermal noise received by the antenna. To model this noise, consider Figure 3.8 which shows a received signal with a random noise $n(t)$ added on it. The received signal in complex baseband form with the random noise $n(t)$ can be written as:

$$\begin{aligned} \tilde{v}(t) &= \mathrm{I}(t) + j\mathrm{Q}(t) + n_I(t) + jn_Q(t) \\ &= [\mathrm{I}(t) + n_I(t)] + j[\mathrm{Q}(t) + n_Q(t)] \qquad (3.12) \end{aligned}$$

where I(t) and Q(t) are the real and imaginary part of the received signal, $n_I(t)$ and $n_Q(t)$ are the real and imaginary part of the noise. Uses (3.12), the expected received power $E\{|V|^2\}$ with noise is:

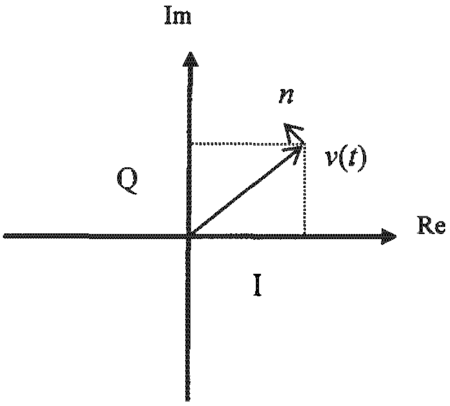

Figure 3.8 The received signal with the additive noise term (*n*).

$$E\{|V|^2\} = E\{\ |\ \mathrm{I}(t) + j\mathrm{Q}(t) + n_I(t) + jn_Q(t)|^2\ \}$$

$$= E\{\ (\mathrm{I}(t) + n_I(t))^2 + (\mathrm{Q}(t) + n_Q(t))^2\ \}$$

$$= E\{\ \mathrm{I}(t)^2 + n_I(t)^2 + 2\mathrm{I}(t)n_I(t) + \mathrm{Q}(t)^2 + n_Q(t)^2 + 2\mathrm{Q}(t)n_Q(t)\ \} \qquad (3.13)$$

The term $2\mathrm{I}(t)n_I(t)$ and $2\mathrm{Q}(t)n_Q(t)$ in (3.13) are statistically un-correlated, i.e. $2\mathrm{I}(t)n_I(t) = 0$ and $2\mathrm{Q}(t)n_Q(t) = 0$. Equation (3.13) becomes:

$$E\{|V|^2\} = E\{\ \mathrm{I}(t)^2 + n_I(t)^2 + \mathrm{Q}(t)^2 + n_Q(t)^2\ \}$$

$$= [\sigma^2_I + \sigma^2_{nI}] + [\sigma^2_Q + \sigma^2_{nQ}] \qquad (3.14)$$

= [variance on real part] + [variance on imaginary part]

where $\sigma_I = \sigma_Q = \sqrt{\dfrac{E\{|V|^2_{NO-NOISE}\}}{2}}$

where σ_I and σ_Q are the standard deviations of the in-phase (real) and quadrature-phase (imaginary) component for the received signal, σ_{nI} and σ_{nQ} are the standard deviations of the in-phase and quadrature-phase component for the noise. Equation (3.14) gives us a way to model the received power with the noise. This relationship will thus be uses for the SAR simulator to model the receiver noise in the following chapter.

Chapter 4

Development of the SAR Simulator

The aim of this chapter is to develop the SAR simulator that creates realistic SAR images from the scene's digital elevation model (DEM). To accomplish this task, simulation algorithms are derived based on the knowledge of Synthetic Aperture Radar system.

Recall the primary objective of this dissertation is to design fast algorithms for a SAR simulator. One important issue that addresses the simulation design is thus the trade-off between the simulation accuracy and the executing time of the simulation software. Two types of simulation approach were considered. The first method is the signal-based approach (as the coherent system described in Chapter 1), which model the returned signals from the targets and focused them to form the SAR images. This method has the advantage of creating accurate results but was extremely time consuming because large amount of data were needed for the simulation. The second method is the geometry-based approach (as the incoherent system described in Chapter 1), which produced the focused SAR images directly from the input DEM. The advantage of this second method is the great reduce of simulation execution time but produces slightly inaccurate results compare to the first method. Since large scale terrain features are preferred rather then small scale details on the ground and the simulation speed was an important concern for this project, the geometry-based approach for the SAR simulator was chose for this dissertation.

The chapter begins with a model that describes all the necessary inputs and outputs of the simulation system. This is followed by the technique that used to obtain a set of sample points from the scene's DEM and then use this information to find out the scattering points on the ground terrain as well as the properties of these scattering

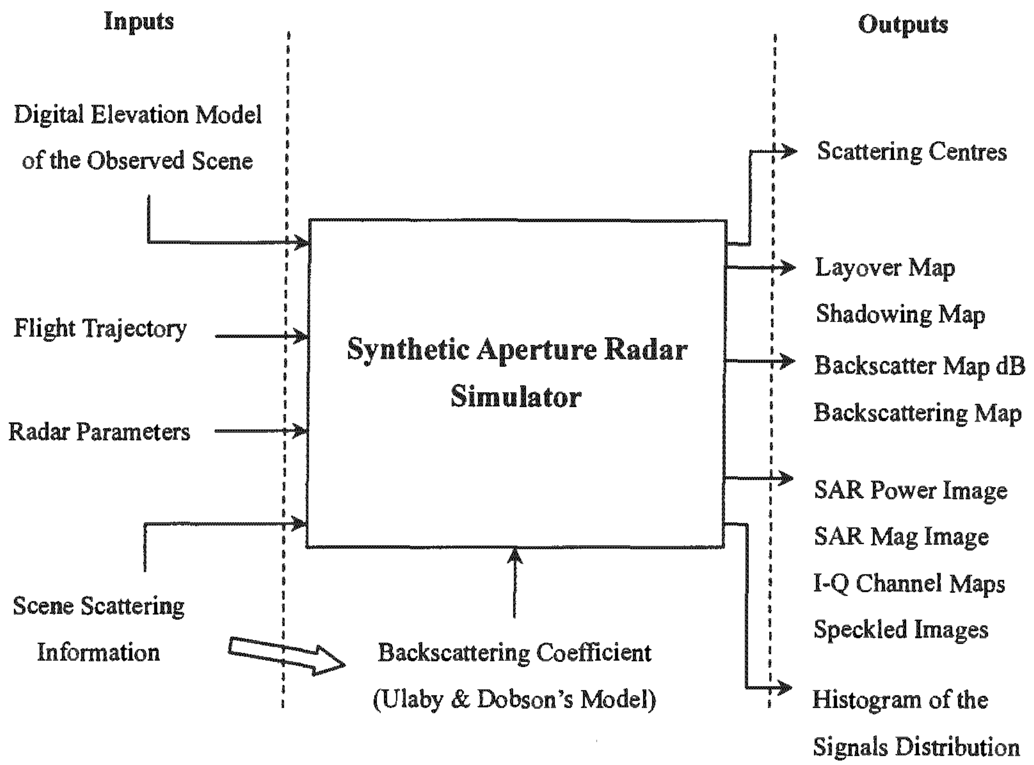

Figure 4.1 Forward Model of the Synthetic Aperture Radar simulator with Inputs and Outputs.

points. The techniques of making the radar shadowing and layover maps were discussed. Finally, the last part of this chapter focused on the procedure of creating the SAR images from the simulation data.

4.1 SAR Simulation Model

4.1.1 Simulator IO System

Before commencing the development of simulation algorithms, one should consider the basic structure of the simulator. In other words, what the simulator should generate and what are its inputs. Figure 4.1 shows the basic model for the SAR simulator and indicated the expected inputs and outputs of simulation. Brief descriptions were given below for each component.

Inputs of Simulation

- Digital Elevation Model of the scene is a set of digital data representing the observed terrain height map in the conventional xyz coordinate system (with x and y represents the spatial coordinates of a point target and z indicates the height). In the SAR simulator, the DEM can either be created by the user (i.e. a Gaussian Mountain etc.) or by using the real terrain's data.

- The flight trajectory of antenna was represented by the state vectors, which indicated the spatial positions of radar at some specific times.

- Radar parameters include the pulse repetition frequency (PRF), system carrier frequency, antenna beam looking angle and image resolution etc. that the simulator required to accomplished the simulation job.

- The scattering information of scene informs the simulator what is the type of terrain on the imaging area. Furthermore, the backscattering model σ^0 employed in the simulation was from Ulaby and Dobson's publication [8].

Output of Simulation

- The layover and shadow maps are images that reveal the regions of layover and shadowing when the radar mapping through the scene.

- The map of backscattering coefficient (σ^0) display the reflective properties of the ground terrain at specific carrier frequency and waveform polarization.

- The simulated SAR images, which include the expected received power, signal magnitude (amplitude), the in-phase and quadrature-phase images in the slant range, zero-Doppler plane relative to the antenna flight path.

- The histograms of the signal distribution should have the same result discussed in Chapter 3. That is, Gaussian distributed random variables with zero mean for the in-phase and quadrature-phase components, Rayleigh distribution for signal magnitude and a negative exponential pattern for received power.

4.1.2 The Central Part of SAR Simulator

Once the inputs and outputs of the SAR simulator were defined, we should now consider the central part of the simulator. That is, the required actions of the simulator in order to obtain the desired outputs. Recalled from Chapter 3, radar can only measure the change of the transmitted power when the signal interacts with some physical object, this altered power or the expected received power $E\{|V|^2\}$ is therefore the goal of the simulator. Using equation (3.9), the relationship of the received power $E\{|V|^2\}$ and the Radar Cross Section of target σ is [13]:

$$E\{|V|^2\} \propto \sigma \tag{4.1}$$

In addition, the RCS can be expressed to the product of backscattering coefficient σ^0 and the corresponding ground area A_{GR} as:

$$\sigma = \sigma^0 A_{GR} \tag{4.2}$$

(4.1) and (4.2) immediately tells that the RCS of an object is an important factor for the SAR simulator, and in order to obtain the RCS of a physical object on the imaging ground, the corresponding backscattering coefficient and ground patch area are required. A brief simulation plan was given below to describe the procedures to achieve this:

1. For each antenna azimuth sample position, find the intersection of the zero-Doppler plane with the DEM. This will defined a cross-section represented by a set of sample points $\vec{s}$ on the observed scene, as illustrated in Figure 4.2.

2. Use the sample point set $\{\vec{s}\}$ to work out the backscattered points $\vec{p}$ on the ground terrain that separates each other by slant range spacing. Some properties of backscattered points must be found, which includes their range $\vec{r}$ with respect to radar and the surface normal $\vec{n}$.

3. Convert a small patch in the slant range image domain into the ground range image domain. This is equivalent to:

$$A_{SR} \rightarrow A_{GR} \tag{4.3}$$

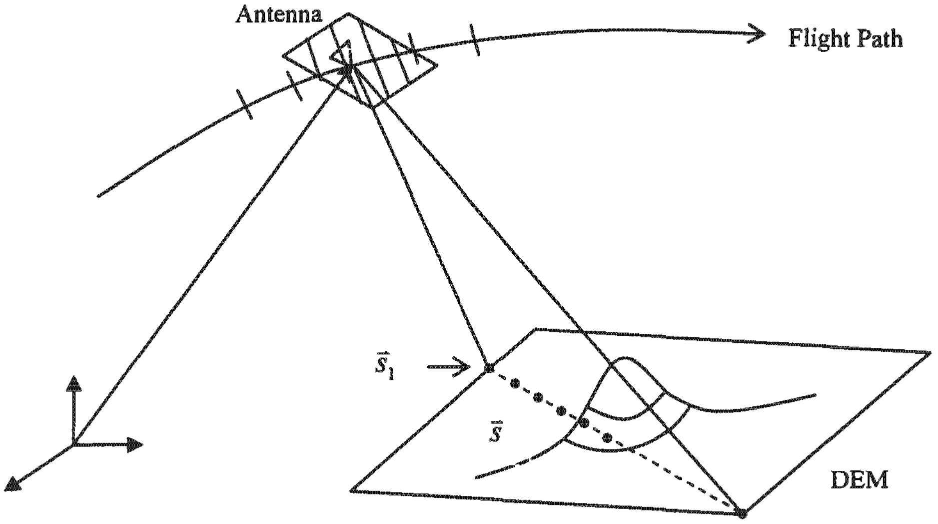

Figure 4.2 Illustration of the intersection of the antenna zero-Doppler plane and the Digital Elevation Model of the observed scene.

4. Find the corresponding σ^0 from the empirical model of the backscattering coefficient. This will require information of system carrier frequency, type of terrain on the imaging ground and the signal incident angle to the target.

5. The expected received power $E\{|V|^2\}$ is thus a product of backscattering coefficient and the relative ground patch area:

$$E\{|V|^2\} = \sigma^0 A_{GR} \tag{4.4}$$

4.2 Technique of DEM Interception

The first task to build up the SAR simulator is to find a set of sample points on the imaging area that are perpendicular to the instantaneous velocity of antenna. The work presented in this section was based an approach proposed by Dr. Andrew J. Wilkinson

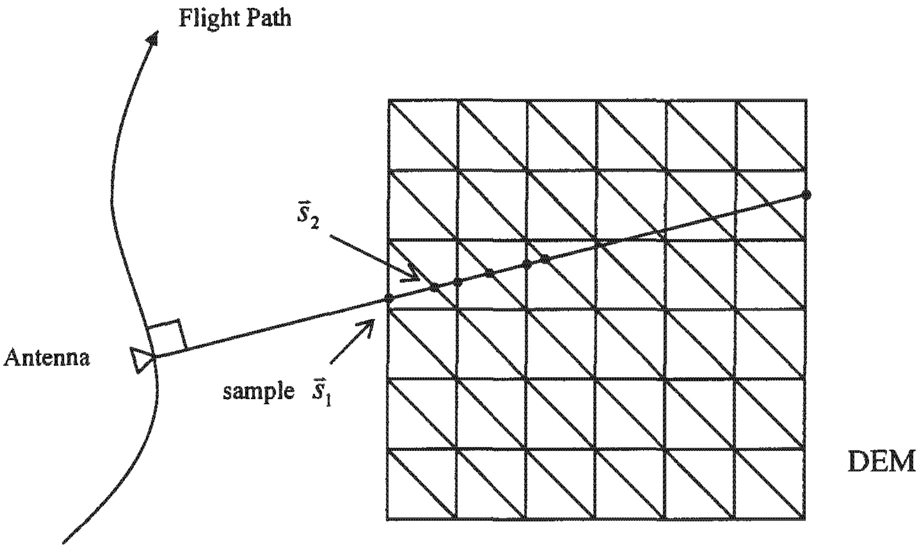

Figure 4.3 Illustration of the image radar cutting through the observed DEM.

and implemented by Freek van Leijen [16]. Unfortunately none of the geometric theory was documented in [16], and the vector mathematics was redeveloped and implemented as part of this project. Consider a radar flying on a specified path while imaging a portion of ground, as indicated in Figure 4.3, where the observed scene can be treated as a piecewise set of triangular patches. The goal in this section is to find a way to cut through the scene while collecting sample points $\vec{s}$ on the DEM (black dots in Figure 4.3). To solve this problem, we need equations that describe the intersection of a line and a plane.

4.2.1 Mathematic Description

Figure 4.4 is a vector diagram which illustrates the above mentioned situation. A plane perpendicular to the antenna velocity vector $\vec{v}$ intersects a line segment from $\vec{P}_N$ to $\vec{P}_{N+1}$ on the observed DEM at point $\vec{s}$. The line segments are the side of the DEM triangles which are intersected by the zero-Doppler plan. In practice, the algorithm processes each triangle in term from near range to far range across the DEM. The required sample point $\vec{s}$ can be written as:

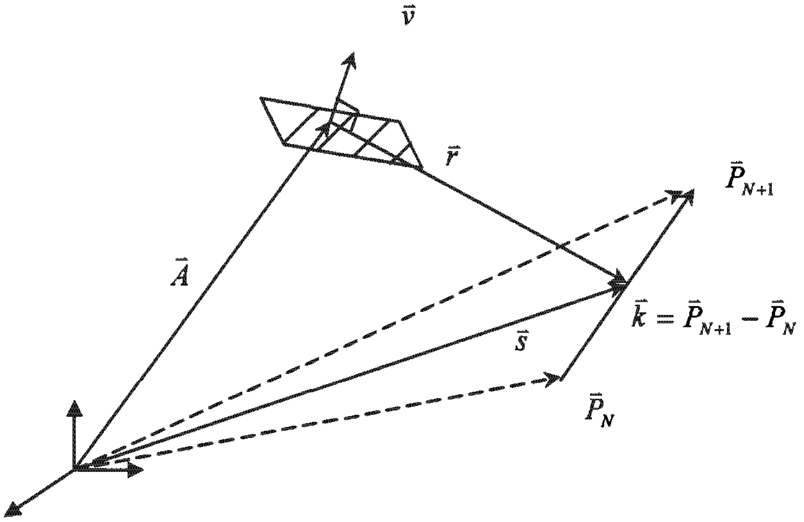

Figure 4.4 Vector diagram for intersection of a line and a plane.

$$\vec{s} = \vec{P}_N + a\vec{k} \tag{4.5}$$

where $\vec{k} = \vec{P}_{N+1} - \vec{P}_N$

where a is fractional number denoted the ratio of the line segment $\vec{k}$, and $\vec{P}_N$ and $\vec{P}_{N+1}$ are the DEM's sample points. Notice that the only unknown in equation (4.5) is the fractional ratio a, and if we can somehow replace this unknown with other known parameters, we will have a mathematic description for the line-plane intersection. Using vector geometry, two equations can be derived relating to the range $\vec{r}$ as:

$$\vec{r} \bullet \vec{v} = 0 \tag{4.6}$$

$$\vec{r} = -\vec{A} + \vec{s} \tag{4.7}$$

where $\vec{A}$ is the position of radar. Substituting (4.7) into (4.6) and replacing the sample point $\vec{s}$ with the parameters in (4.5):

$$a = ((\vec{A} - \vec{P}_N) \bullet \vec{v}) \ / \ (\vec{k} \bullet \vec{v}) \tag{4.8}$$

Equations (4.5) and (4.8) together forms the required mathematic description of a plane intersects with a line. Notice that (4.8) assumed $\vec{r} \bullet \vec{v}$ equal to zero, i.e. $\vec{r}$ lies in the zero-doppler plane.

4.2.2 Geometric Point of View

The equations derived in section 4.2.1 were only for intersection of a single line segment on the observed scene. To apply these equations into the whole DEM and find the desired sample point set, one requires a systematic algorithm related to the geometric layout of the DEM.

For a rectangular DEM, there exist six possible line-plane intersections to cut through the scene, where these intersections can be further classified into three types of category according to their starting 'edge', as shown on the left side of Figure 4.5. Next to each of the edge cutting diagrams were three small sketches that indicate the algorithm to walk through the scene. Although intersections through different edges required different cutting methods, the fundamental idea behind them was the same, namely the intersections from a vertical segment, a horizontal segment and a slanted segment from the sides of the triangular patches. Descriptions on how to "cut" through the scene were given below using the corner symbols I ~ IV as indicated in Figure 4.5. Furthermore, the starting segment was always consisted by the corner symbol { I , II }:

- For intersections start from Edge 1 as shown in Figure 4.5(a), employ the following methods:
  - Start from a 'vertical segment' has possible intersection to segments { I , III } and { II , III }.
  - Start from a 'horizontal segment' has possible intersection to segments { III , II }, { I , IV } and { II , IV }.
  - Start from a 'slanted segment' has possible intersection to segments { I , III }, { IV , II } and { III , II }.

- For intersections start from Edge 2 as shown in Figure 4.5(b), employ the following methods:
  - Start from a 'vertical segment' has possible intersection to segments { III , II }, { I , IV } and { II , IV }.

  - Start from a 'horizontal segment' has possible intersection to segments { I , III } and { II , III }.
  - Start from a 'slanted segment' has possible intersection to segments { I , IV }, { III , II } and { IV , II }.

- For intersections start from Edge 3 as shown in Figure 4.5(c), employ the following methods:
  - Start from a 'vertical segment' has possible intersection to segments { III , I }, { II , IV } and { III , II }.
  - Start from a 'horizontal segment' has possible intersection to segments { III , II } and { III , I }.
  - Start from a 'slanted segment' has possible intersection to segments { I , IV }, { III , II } and { I , III }.

Notice that the positions of the above mentioned corner symbols in Figure 4.5 can be exchanged into any position (and any other symbols) provides a suitable re-index were employed.

The use of the geometric algorithm described in Figure 4.5 together with the help of equations (4.5) and (4.8), forms the essence of the DEM interception technique. One important parameter need to be take care of is the fractional ratio a in equation (4.8). Since a represent the ratio of the line segment $\vec{k}$, the value of a can not be exceed one or less than zero. That is

$$0 \leqq a \leqq 1 \tag{4.9}$$

Only values falling into this range will be considered as a true intersection of the desired line-plane intersection. For those that greater than one or less then zero it can be calculated that the zero-Doppler plane does not intersect the line along the segment between the two points of consideration, thus will be treated as false alarm and discarded.

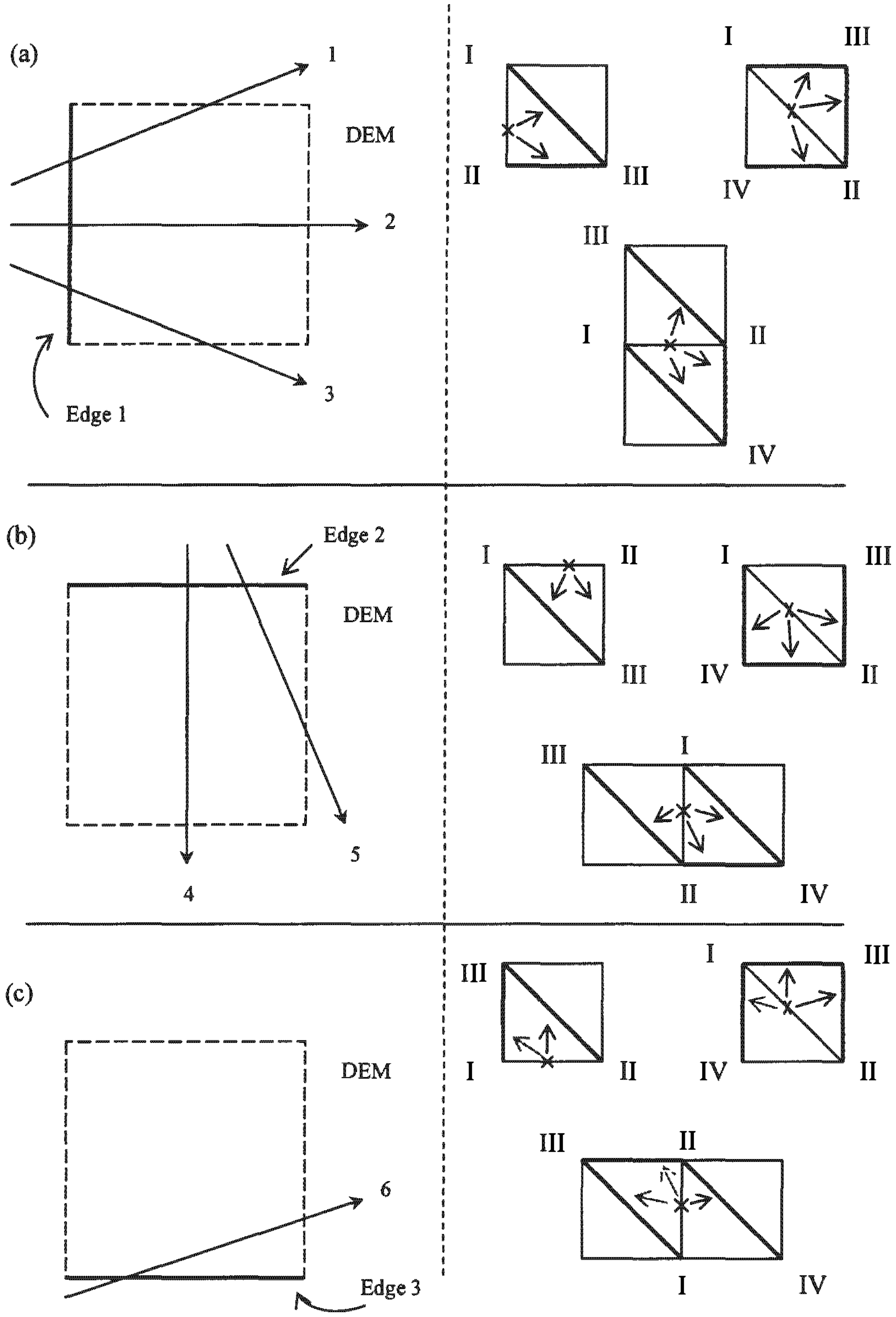

Figure 4.5 Six possible line-plane intersections and their corresponding schemes to walk through the scene.

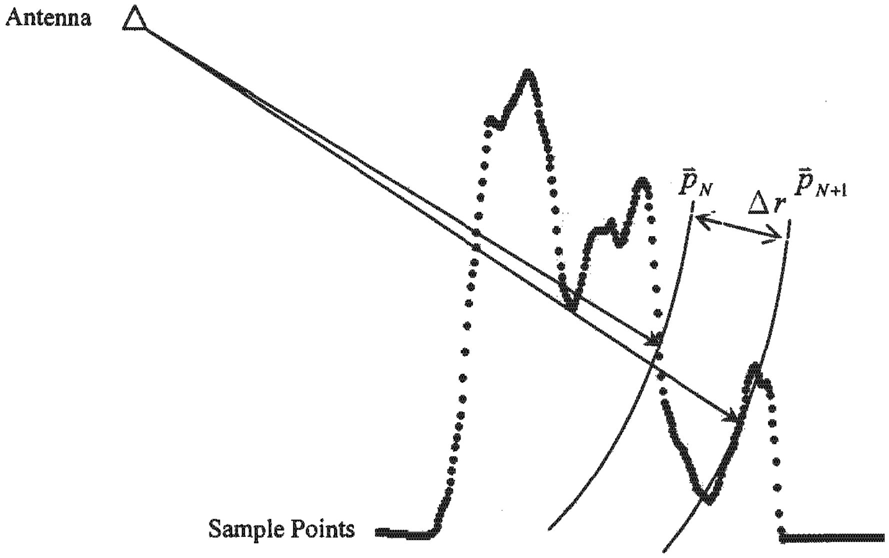

Figure 4.6 Illustration of taking scattering centres from the sample point set.

4.3 The Scattering Centre

After the sample points $\{\vec{s}_i\}$ have been collected along the intersection of the zero-Doppler plane, the next task is to find the scattering centres $\vec{p}$ from the sample point set, as depicted in Figure 4.6. The scattering centre can be defined as the spatial position of a ground patch (or more precisely, the centre position of a ground patch) that backscattered the transmitted energy to the receiver and separate each other by slant range and azimuth resolution spacing. Notice that the sample points obtained from last section are actually a cross-section of the observed terrain's height map with irregular inter-point spacing.

4.3.1 Position of Scattering Centre

To work out the scattering centre $\vec{p}$, consider Figure 4.7 showing the intersection of a constant range arc with a line segment from $\vec{s}_N$ to $\vec{s}_{N+1}$. The position of the scattering point is:

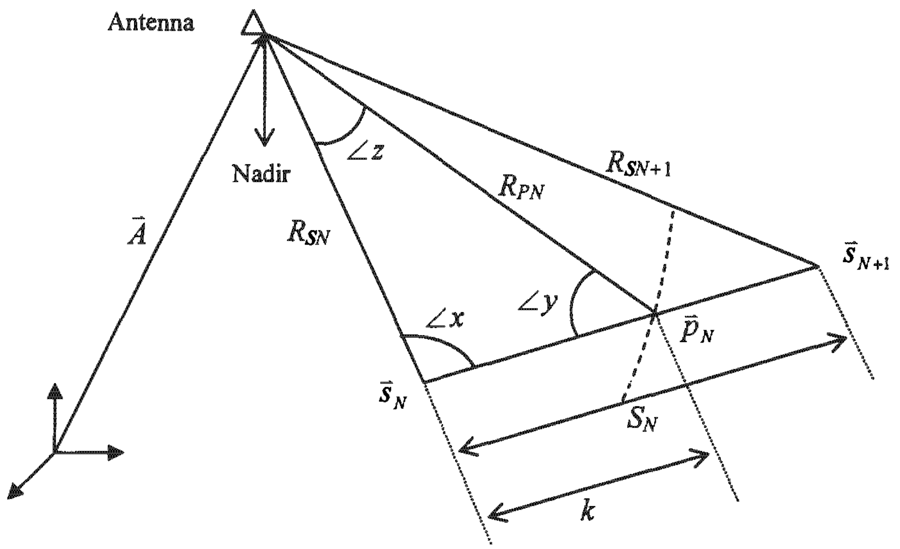

Figure 4.7 The vector geometry for finding the scattering centres.

$$\vec{p}_N = \vec{s}_N + b(\vec{s}_{N+1} - \vec{s}_N) \tag{4.10}$$

where b represents the ratio of the line segment consisted by $\vec{s}_N$ and $\vec{s}_{N+1}$. Use the law of Cosines we can find the angle $\angle x$ as:

$$R_{SN+1}^2 = R_{SN}^2 + S_N^2 - 2R_{SN}S_N\cos(\angle x) \tag{4.11a}$$

$$\rightarrow \quad \angle x = \cos^{-1}\left(\frac{R_{SN+1}^2 - R_{SN}^2 - S_N^2}{-2R_{SN}S_N}\right) \tag{4.11b}$$

Employ the law of Sines for a triangle to find $\angle y$:

$$\frac{\sin(\angle x)}{R_{PN}} = \frac{\sin(\angle y)}{R_{SN}} \tag{4.12a}$$

$$\rightarrow \qquad \angle y = \sin^{-1}\left(\frac{R_{SN}}{R_{PN}}\sin(\angle x)\right) \qquad (4.12b)$$

We then have $\angle z$. Use the Sines law again to fine the length of k:

$$k = R_{PN}\frac{\sin(\angle z)}{\sin(\angle x)} \qquad (4.13)$$

and thus the fractional ratio b is:

$$b = k \;/\; S_N \qquad (4.14)$$

Equations (4.10) through (4.14) form the mathematic description of the position of the scattering centre. The following algorithm steps described how the task was achieved:

1. Start from Near Range to Far Range; analyze the intersection of the range arc to the line segment consisted by the sample point set $\{\bar{s}\}$.

2a. If intersection was found, that is:

$$0 \leqq b \leqq 1 \qquad \text{for a valid scattering centre}$$

record the scattering centre $\bar{p}_n$ and update the length of the range arc R_{PN} by the slant range spacing Δr ($R_{PN} = R_{PN} + \Delta r$).

2b. If the intersection was not found, analyze next line segment.

4.3.2 Properties of Scattering Centre

The properties of the scattering centre include the range from the radar sensor $\bar{r}$ and the surface normal $\bar{n}$.

The range can be found directly from the geometry shown in Figure 4.6 as:

$$\bar{r}_N = \bar{p}_N - \bar{A} \qquad (4.15)$$

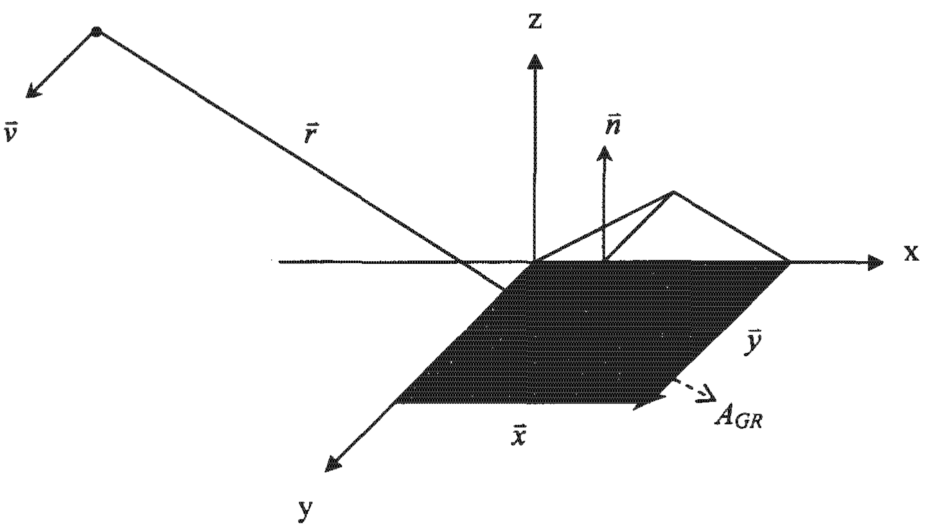

Figure 4.8 Mapping the slant range area into the ground range area.

where $\vec{A}$ is the position of radar.

For the surface normal, consider the triangular ground patch layout in Figure 4.3. One can use the cross product of two vectors to work out their surface normal. However, attention must be paid for the way cross product was performed according to the right-hand rule, e.g. ($\boldsymbol{a} \times \boldsymbol{b}$) = - ($\boldsymbol{b} \times \boldsymbol{a}$).

4.4 Slant Range to Ground Range Domain Conversion

The purpose of this section is to find the projection of a small patch in the slant range image domain into the ground range image domain. The work present in this section was based on Wilkinson's work [17].

Consider Figure 4.8, $\hat{r}$ (unit vector of $\vec{r}$) and $\hat{v}$ (unit vector of $\vec{v}$) forms a small parallelogram in the slant range domain, the objective here is to project these two vectors and thus the small parallelogram onto the ground range domain as $\vec{x}$ and $\vec{y}$. The area of the resulting patch is thus $A_{GR} = |\vec{x} \times \vec{y}|$. Consider the parameter $\vec{x}$, the vector is perpendicular to $\hat{v}$ and $\hat{n}$ (unit vector of $\vec{n}$):

$$\vec{x} \bullet \hat{v} = 0 \tag{4.16}$$

$$\vec{x} \bullet \hat{n} = 0 \tag{4.17}$$

Thus the unit vector of $\vec{x}$ is:

$$\hat{x} = \frac{\hat{v} \times \hat{n}}{|\hat{v} \times \hat{n}|} \tag{4.18}$$

To find $\vec{x}$, consider that the projection of $\vec{x}$ onto the direction defined by $\hat{r}$ is equal to the image patch length of 1, this is:

$$\vec{x} \bullet \hat{r} = 1 \tag{4.19a}$$

$$\hat{x} \bullet \hat{r} = \frac{1}{|\vec{x}|} \tag{4.19b}$$

Use (4.18) and (4.19b), we have:

$$\vec{x} = |\vec{x}|\, \hat{x} = \frac{\hat{v} \times \hat{n}}{\hat{v} \times \hat{n} \cdot \hat{r}} \tag{4.20}$$

Employ similar method to find $\vec{y}$:

$$\vec{y} \bullet \hat{r} = 0 \tag{4.21}$$

$$\vec{y} \bullet \hat{n} = 0 \tag{4.22}$$

$$\hat{y} = \frac{\hat{r} \times \hat{n}}{|\hat{r} \times \hat{n}|} \tag{4.23}$$

and $$\hat{y} \bullet \hat{v} = \frac{1}{|\vec{y}|} \tag{4.24}$$

so $\vec{y}$ equals to:

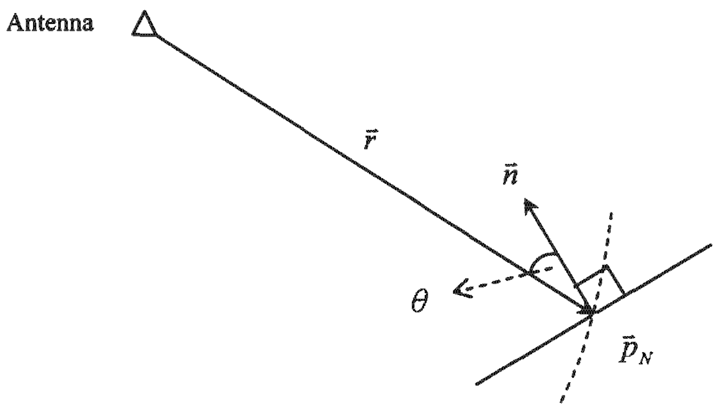

Figure 4.9 Image geometry to obtain the signal incident angle.

$$\vec{y} = |\vec{y}|\,\hat{y} = \frac{\hat{r}\times\hat{n}}{\hat{r}\times\hat{n}\cdot\hat{v}} \tag{4.25}$$

The Area of the parallelogram defines by $\vec{x}$ and $\vec{y}$ is thus:

$$A_{GR} = |\vec{x}\times\vec{y}| = \frac{|(\hat{v}\times\hat{n})\times(\hat{r}\times\hat{n})|}{(\hat{v}\times\hat{n}\cdot\hat{r})^2} \tag{4.26}$$

4.5 Backscattering Coefficient of Target

The final step to simulate the radar received power is to work out the backscattering coefficient σ^0 of the scattering centre. To find out σ^0, consider the empirical model described in Chapter 3, which indicated that the backscattering coefficient of a physical body is a function of signal incident angle at specific terrain type, carrier frequency and waveform polarization. Since the position of scattering centre $\vec{p}$ and the corresponding range $\vec{r}$ have being worked out in the previous section, the signal incident angle can be found from dot product and the geometry described in Figure 4.9 as:

$$\theta = \cos^{-1}(\hat{n} \bullet (-\hat{r})) \tag{4.27}$$

where θ is the signal incident angle with respect to the surface normal.

The backscattering coefficient σ^0 in the SAR simulator were represented in numeric form in decibel scale with the corresponding incident angle in degree. Once the signal incident angle has been worked out, the backscattering coefficient can be worked out by looking up the empirical data by means of mathematic interpolation for the specific incident angle and terrain type.

A complete set of the empirical model for backscattering coefficients σ^0 used in this dissertation can be found at Appendix C; these figures were drawn from Matlab program and were based on the information obtained from Ulaby and Dobson's publication [8].

4.6 Geometric Related Maps

In this section, we will look at the algorithm developed to create two types of radar image that were related to the geometric layout of the observed scene, namely the shadowing map and the layover map.

4.6.1 Radar Shadowing Map

Consider a shadow region on the imaging ground as shown in Figure 4.10. The parameter that determined whether a region were under the effect of shadowing is the looking angle α. When the radar scanned through an observed scene, α will always increase unless shadowing occurred. Based on this property, an algorithm for radar shadowing map can be derived as follow:

1. Record the looking angle of the first scattering centre into α_{temp}.

2. Compare α_{temp} with the looking angle of next scattering centre.

3a. If the compared looking angle is greater than or equal to α_{temp}, store it as the new α_{temp}.

3b. If the looking angle is smaller than α_{temp} (shadowing occurred), mark the position of the compared scattering centre as shadowing region.

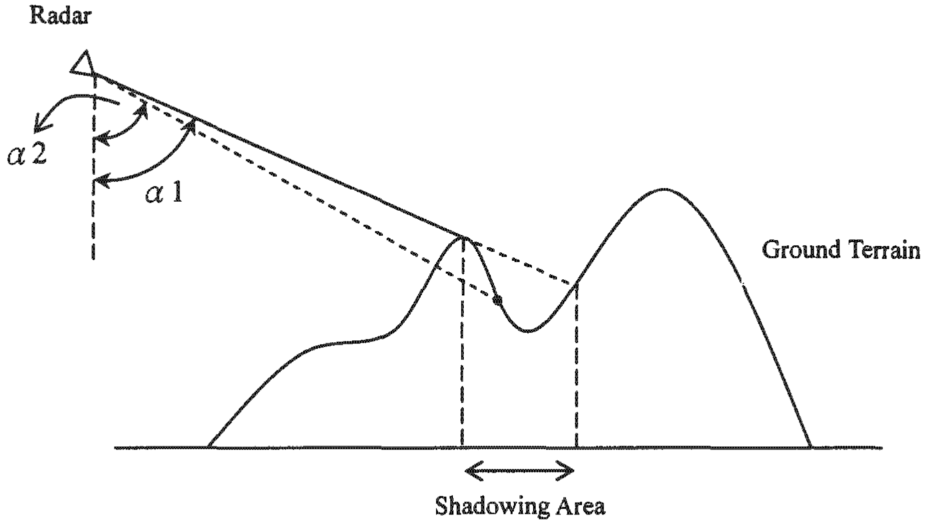

Figure 4.10 Illustration of the make for radar shadowing map.

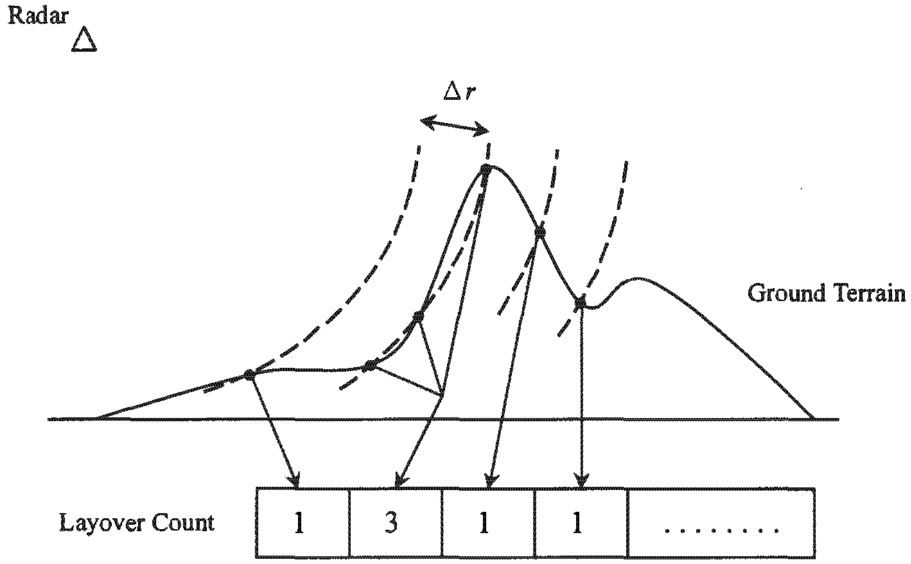

Figure 4.11 Illustration of the make for radar layover map.

4. Repeat step 2 to 3 until the last scattering centre was examined.

4.6.2 Radar Layover Map

Consider a radar sensor scanned through the ground terrain as shown in Figure 4.11, where some regions on the scene were overlaid on top of each other in the slant range domain. The parameter that determined whether the regions was overlaid is the distance range R_{PN} of the scattering centre, and it is clear from Figure 4.11 that the layover regions have the same range distance to the antenna. Thus a layover map can be created by examine the distance of the scattering centres with respect to the radar and count for the number of overlaid through out the available scattering centres, as illustrated in Figure 4.11.

4.7 Other Aspects of the Simulator

In this section, other aspects of the SAR simulator will be examined. These includes model of antenna flight trajectory and observed scene's DEM, the range dependency of received signal and the receiver noise.

4.7.1 Model of Antenna Flight Trajectory and Scene's DEM

The antenna flight trajectory within the SAR simulator was modeled by the state vectors. The antenna state vector is a set of xyz coordinates depicted the position of the radar sensor at some specific time (t). In this project, the simulator uses 5 state vectors to model the complete antenna flight trajectory.

For the case of satellite SAR simulation, the antenna state vectors were obtained from the European Space Agency ERS-2 satellite real data. These data were originally in the Earth-centred co-ordinate system. To make use of these state vectors in the simulation, a co-ordinate system transformation was performed from Earth-centred ellipsoidal co-ordinate system into the flat-Earth xyz co-ordinate system by using a software called "XForm". XForm is a multi-purpose co-ordinate transformation package designed for the African environment by Charles Merry and Bruce Merry. The state vectors was transformed using XForm from Earth-centred Ellipsoidal co-ordinate system into the Gauss Conform Orthometric co-ordinate system, a system with the coordinates arranged in (y , x , height) order above the sea level. This co-ordinate system was also known as the “Lo” system.

The Digital Elevation Model of the scene was obtained from the “Chief Directorate of Surveys and Mapping, Department of Land Affairs, South Africa”. The DEM of the observed scene on the other hand comes with the “Lo” co-ordinate system and can thus be applied into the simulation without any co-ordinate transformation.

4.7.2 Range Compensation

In the previous sections, the primary goal is to work out the radar cross section σ in order to model the received power of SAR. For accurate model of the received power, the range dependency of the received pulse must be included into the calculation. Using the radar equation for a SAR system as described in [27] and [28], the signal-to-noise ratio for an image pixel with homogenous distributed target can be represents as:

$$\mathrm{SNR} \propto \frac{\sigma^0}{R^3} \tag{4.28}$$

where σ^0 is the backscattering coefficient of the imaging target and R is the range from antenna to the target. Equation (4.28) shown that the signal-to-noise ratio of SAR is proportional to the backscattering coefficient and inverse proportional to the range. Thus the SNR decreases if the distance of the imaging target is further away from the radar sensor. To compensate for this range effect, the resulting expected received power $E\{|V|^2\}$ will be multiplied by the range term R^3.

4.7.3 Model for the Receiver Noise

When the transmitted pulses were scattered back to the antenna receiver, a random noise was added into the received power. Consider Figure 4.12(a), which shows the radar received power and the receiver noise. It is clear that at near range the noises have less effect to the received power. However, as the range of the imaging target increases (so the backscattered power was weaken due to range effect), the noises start to take over the radar received power. An important concern in this section is how to deal with the range compensation with the receiver noise. Since the received

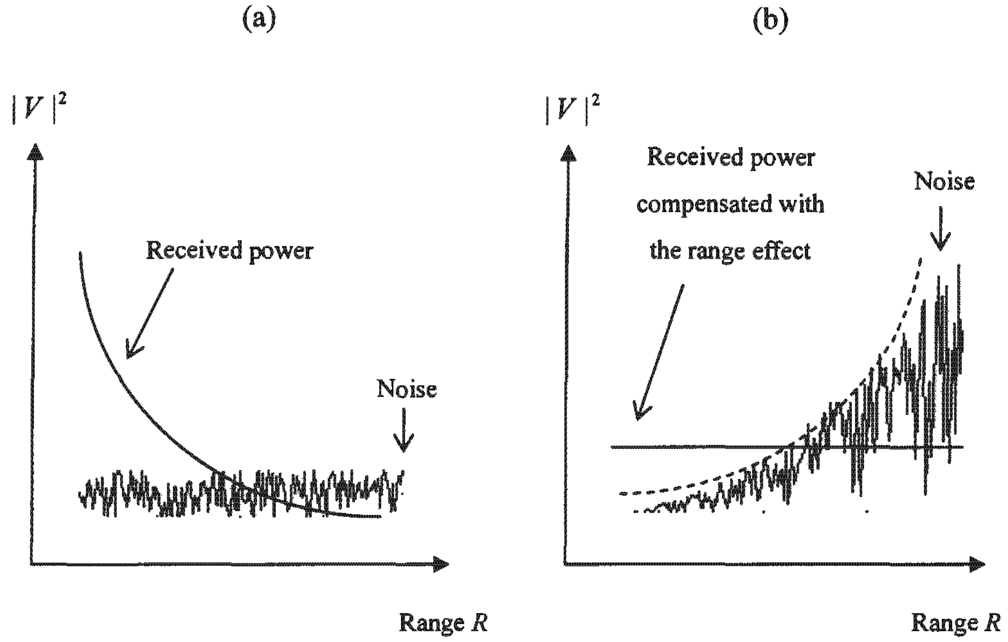

Figure 4.12 Radar received power in the presence of receiver noise (a) before range effect compensation and (b) after range effect compensation.

power needs to compensate the range effect, the receiver noise at far range will inevitably be increases by the range compensation process. The situation was depicted in Figure 4.12(b) with the dashed line shows the envelope of the enlarged receiver noise. To model this noise in the simulation, the following algorithm was employed:

1. Defined the required signal-to-noise (SNR) ratio at the mid-swath of the imaging area and the corresponding backscattering coefficient σ^0 in the simulation, assume flat surface at the mid-swath. The backscattering coefficient was an estimation from the mid-swath angle and the information at Appendix C.

2. The relationship between the SNR, radar received power and the average noise power is:

$$\mathrm{SNR}_{\text{mid-swath}} = \frac{E\{|V|^2_{scene}\}}{E\{|n(t)|^2\}} \tag{4.29}$$

Where $E\{|V|^2_{scene}\}$ is the signal power from the scene at mid-swath and $E\{|n(t)|^2\}$ is the corresponding noise power. Since the backscattering coefficient σ^0 was defined, one can calculate the expected received power of the scene as $E\{|V|^2_{scene}\} = \sigma = \sigma^0 A_{GR}$, where σ is the radar cross section and A_{GR} is the corresponding ground area. The average noise power is thus:

$$E\{|n(t)|^2\} = \frac{E\{|V|^2_{scene}\}}{SNR_{mid-swath}} \tag{4.30}$$

3. The calculated noise power $E\{|n(t)|^2\}$ was for the case at mid-swath with flat surface terrain on the ground. To extended the algorithm into the whole range bins and included the range effect compensation while still maintain the signal-to-noise ratio at mid-swath as defined in step 1, the following equation were used.

$$\text{Overall power at the } i\text{th range bin} = (E\{|V|^2\}_i + E\{|n(t)|^2\}) \cdot \left(\frac{R_i}{R_{mid}}\right)^3 \tag{4.31}$$

where $E\{|V|^2\}_i$ is the expected received power at the ith range bin, R_i is the range distance at the ith range bin and R_{mid} is the range distance at the mid-swath. Both R_i and R_{mid} can be obtained from the properties of the scattering centre at section 4.3. The important part in equation (4.31) that shapes the receiver noise $E\{|n(t)|^2\}$ into the exponential form as depicted in Figure 4.12(b) is the $(R_i / R_{mid})^3$ term. If $R_i = R_{mid}$, the bracket term becomes unity which gives the desired $\mathrm{SNR}_{\text{mid-swath}}$. If R_i were greater than R_{mid}, the noise power increases with the exponential of the normalized range compensation. If R_i were smaller than R_{mid}, the noise power decreases.

4. Repeat for each range line for the above methods.

The above mentioned algorithm was for model of the receiver noise as depicted in Figure 4.12(b). An important assumption for the above algorithm is to assume flat surface at the mid-swath, which gives the correct estimation (by using the Ulaby and Dobson's model [8]) of the backscattering coefficient σ^0.

4.8 Simulator Structure

Based on the algorithms derived through this chapter, a simplified block diagram described the constitutions of the SAR simulator was presented in Figure 4.13. Descriptions were given below for each block.

- System Input Parameters - the simulation basic inputs which include the state vectors of the antenna flight path, simulation range and azimuth spacing, signal-to-noise ration at the mid-swath of the imaging area, terrain type of the imaging area (DEM), antenna incident angle to the scene etc.
- (Real) DEM Data - The DEM data were contain in a text file with the xyz coordinates in the "Lo" system described in the previous section.
- Pre-define Output Data - inform the simulator the preferred output images at the end of the simulation.
- Scan for Sample Points - find the sample point set $\{\bar{s}\}$ (if intersection occurred) as described in section 4.2.
- Surface Normal - work out the surface normal $\bar{n}$ for the sample point set $\{\bar{s}\}$.
- Position in Space - calculate the scattering centre $\bar{p}$ from the sample point set $\{\bar{s}\}$ and the corresponding properties of the scattering centre such as the range from antenna $\bar{r}$ and the normal vector $\bar{n}$.
- Shadow and Layover Maps - work out the region of shadowing and layover using the algorithms described in section 4.6.
- Slant Range Area to Ground Range Area - conversion of a small path from slant range image domain into ground range image domain using the algorithm described in section 4.4.
- Backscattering Coefficient - find the backscattering coefficient σ^0 of the imaging target. This involves incorporation with the Ulaby and Dobson's empirical model [8] and by using the information provided from the "System Input Parameters"

file (terrain type of the imaging area, radar carrier frequency) as well as the range and normal vector obtained from "Position in Space".

- Expected Received Power - calculate the expected received power by using the equation $E\{|V|^2\} = \sigma^0 A_{GR}$, where σ^0 is the backscattering coefficient and A_{GR} is the corresponding ground area. The receiver noise was also calculated and added into the received power.

- Sort I-Q Channel - sort for the histogram of the I-Q downconverter channel.

- Plot the Results - draw the SAR images from the simulation results.

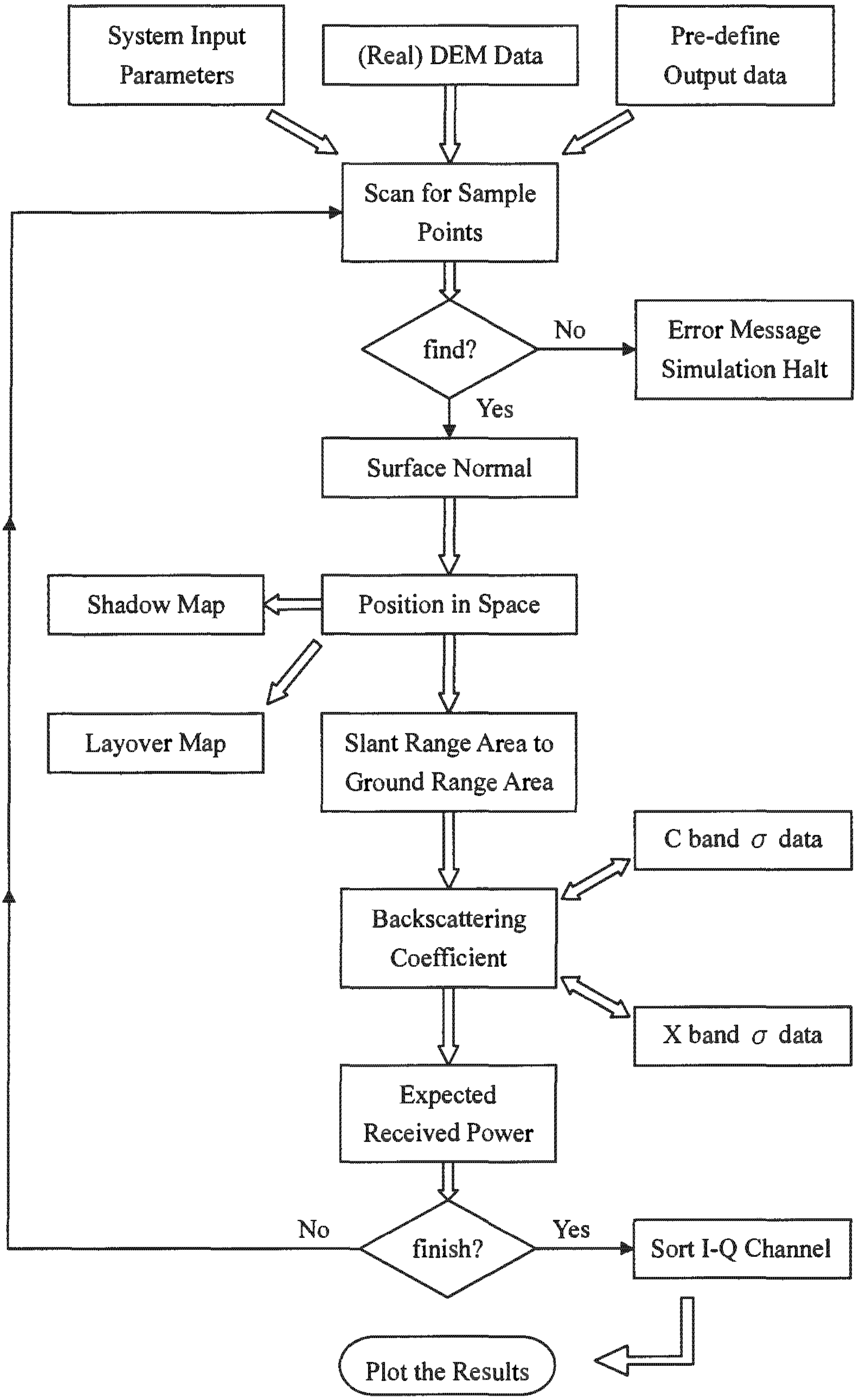

Figure 4.13 Block diagram of the SAR simulator.

Chapter 5

Analysis of the Simulation Results

The purpose of this chapter is to provide complete descriptions to the images and the results generated by the SAR simulator. These include maps of layover and shadowing, backscattering coefficient image, SAR magnitude and power images. Comparisons of the simulated and the real SAR images were performed to test the accuracy and subjective realism of the simulator.

The chapter starts by describing the testing data used to perform the SAR simulation. This is followed by examinations of the observed scene's backscattering coefficient and the corresponding SAR images. The effects of antenna fly trajectory on the produced SAR image will be discussed by compare several images made from different flight path. Finally, the running time of the simulator written in two different programming environments will be examined.

5.1 Simulation Data

The Digital Elevation Model used in this dissertation for SAR simulation is the Cape Peninsula region in South Africa, as shown in Figure 5.1. The DEM data were provided by "Chief Directorate of Surveys and Mapping, Department of Land Affairs, South Africa". The size of the DEM is 22 × 111 km with 200 meter sample spacing. Further manipulation of the DEM is possible to reduce the sample spacing into smaller size by mean of mathematic interpolation. The SAR simulation was run by using the parameters listed in Table 5.1.

Figure 5.1 A top view of the Cape Peninsula Digital Elevation Model.

Simulation Parameter	**Airborne**	**Satellite**
Altitude	10 km	796 km
Wavelength	X-band	C-band
Waveform Polarization	HH	VV
DEM Dimension (row-col)	550 – 110	550 – 110
DEM Pixel Size (range-azim.)	200 m – 200 m	200 m – 200 m
Number of State Vectors	5	5
Incident Angle at mid-swath	37.5 degree	23 degree
Simulated Range Spacing	8 meters	8 meters
Simulated Azimuth Spacing	20 meters	65 meters
Signal-to-Noise ratio (mid)	100 (20 dB)	100 (20 dB)
Imaging Terrain Type	Grass Canopy	Soil and Rock Surface

Table 5.1Reference parameters used in SAR simulation for Section 5.2.

The chosen parameters for the airborne simulation were created by the author since there is no available real data for the airborne SAR at hand. However, some of the parameters employed such as the radar wavelength, waveform polarization and antenna height etc. were using the reference parameters from [2] to make the SAR simulation more close to general airborne case. For satellite case, the reference parameters were from European Space Agency using the "C-band ERS-2 satellite Gamma Interferometric SAR" real data.

One parameter that draws the attention in Table 5.1 was the use of large simulated sample spacing (particularly the satellite azimuth sample spacing) for the simulation. The primary reason for this is to reduce the processing time of the simulation when imaging a large ground terrain. Since the source data (the input DEM) provides the terrain information at each 200 metres spacing, the values of the sample spacing used in simulation as indicated in Table 5.1 were within a reasonable interval and will generally produces visually similar large-scale SAR images as if smaller sample spacing were used.

5.2 Simulated SAR Images

In this section, we will look at the results of two different SAR simulations, namely airborne and satellite SAR simulation of the Cape Peninsula area in South Africa.

5.2.1 Airborne SAR Simulation

The size of the produced airborne SAR images are 980×850 pixels (azimuth×range, approximately 19.6 km×10 km), with the imaging area covered by distributed grasses canopy. The parameters used in this simulation were indicated at Table 5.1. Notice the radar beamwidth of this simulation was large (35 degree, from 20 degree near range to 55 degree far rang); this is for demonstration of imaging a broad area only. Descriptions for each figure are given below:

- The flight path of the imaging sensor and the region of observation are shown in Figure 5.2(a). There are five state vectors for the radar sensor on the image that marked by crosses, each of them represents the position of the radar sensor at particular times. Figure 5.2(b) illustrated the imaging area in 3-D form with the arrow on the left hand side shows the antenna moving direction. This image was drawn from the collection of the scattering centres $\{ \bar{p} \}$ as the antenna scanned through the scene. The area was chosen for demonstration of shadowing effect at far range mountain region and with area containing both flat plain and mountains as shown in Figure 5.2(b).

- Figure 5.3 displays the map of the backscattering coefficient $10\log\sigma^0$ (in Decibel scale) of the imaging ground with the corresponding layover and shadowing images. Notice that the observed scene was under the effect of shadowing at far range field. This is clear from the layout of the 3-D image in Figure 5.2(b) as the height of the mountains gradually increases at far range side. The layover effect only occurred on the tip of the north-west side of the image. It is probably caused by the change of the steepness of the mountain.

- The simulated backscattering coefficient σ^0 of the scene was shown in Figure 5.4 together with the simulated power image. Notice that the power image displayed in Figure 5.4 was speckle-free, that is, the randomly distributed property of the distributed target is not included at this stage. Also notice that the mountain region corresponding in Figure 5.2(b) gives high reflection and thus appeared

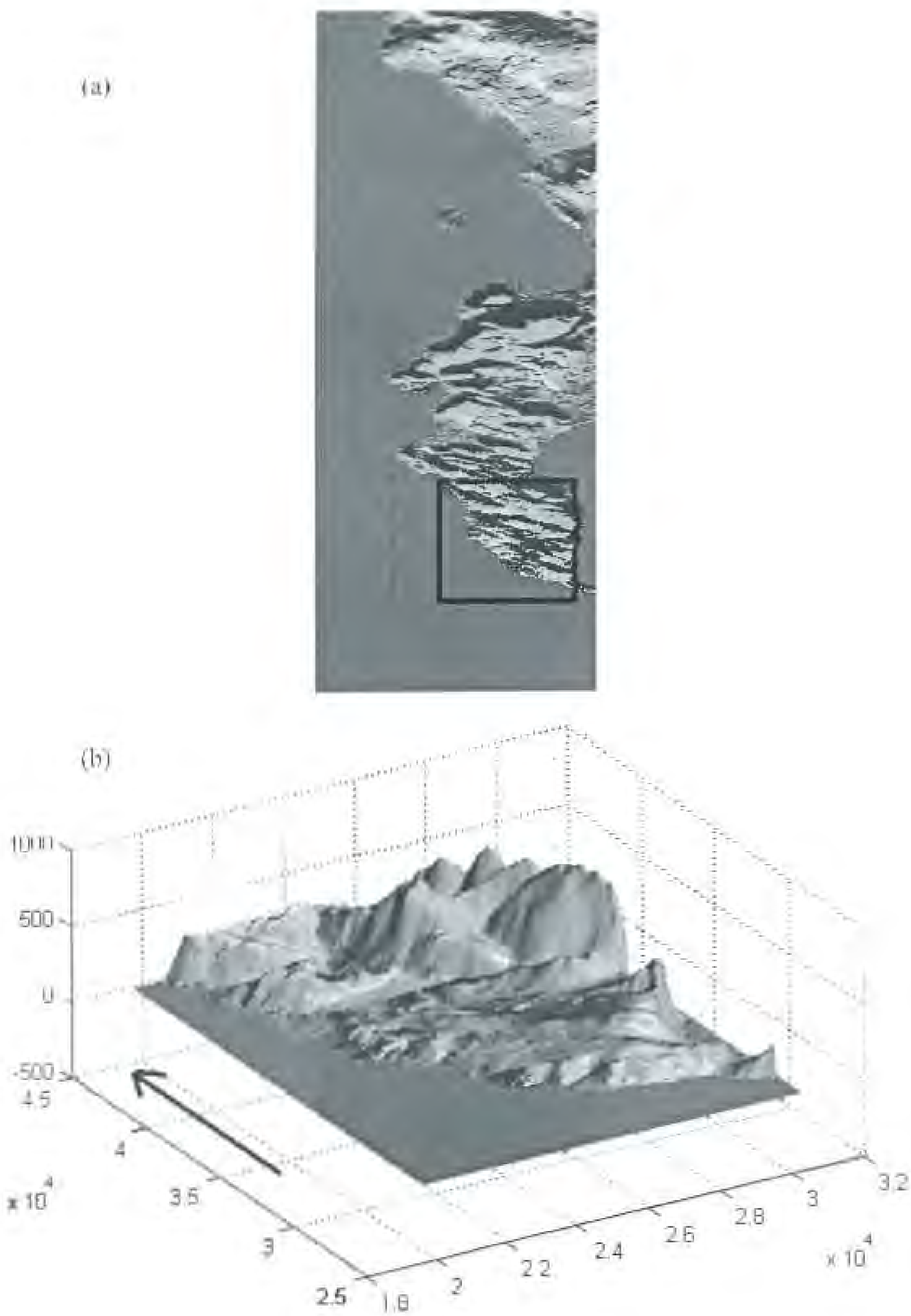

Figure 5.2 (a) Antenna fly trajectory and the area of imaging for airborne SAR. (b) The scattering centres showing the imaging area in 3-D form.

Figure 5.3 Illustration of the (a) backscattering coefficient in dB scale ($10\log \sigma^0$) and (b) the shadowing area of the observed scene and (c) the region of layover.

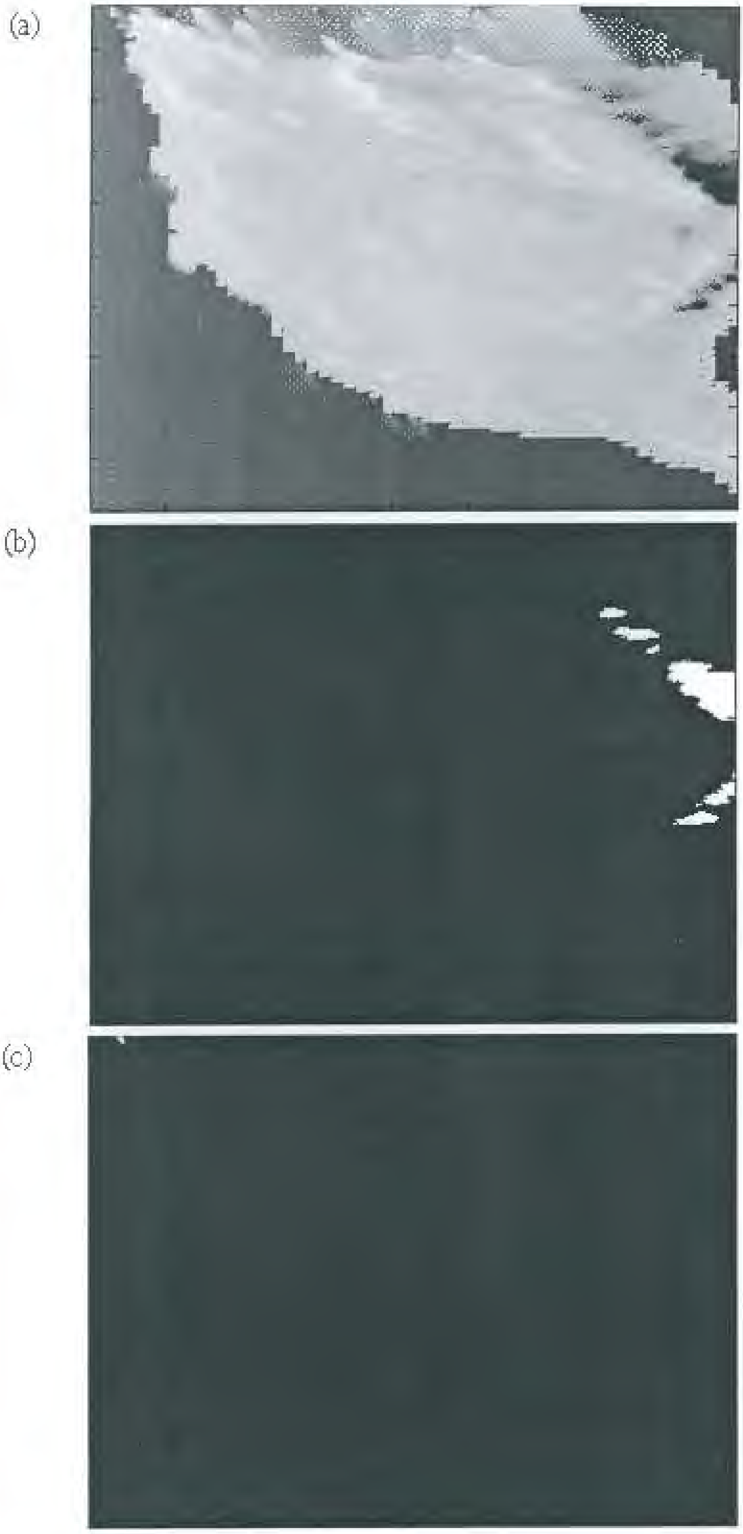

Backscattering Coefficient

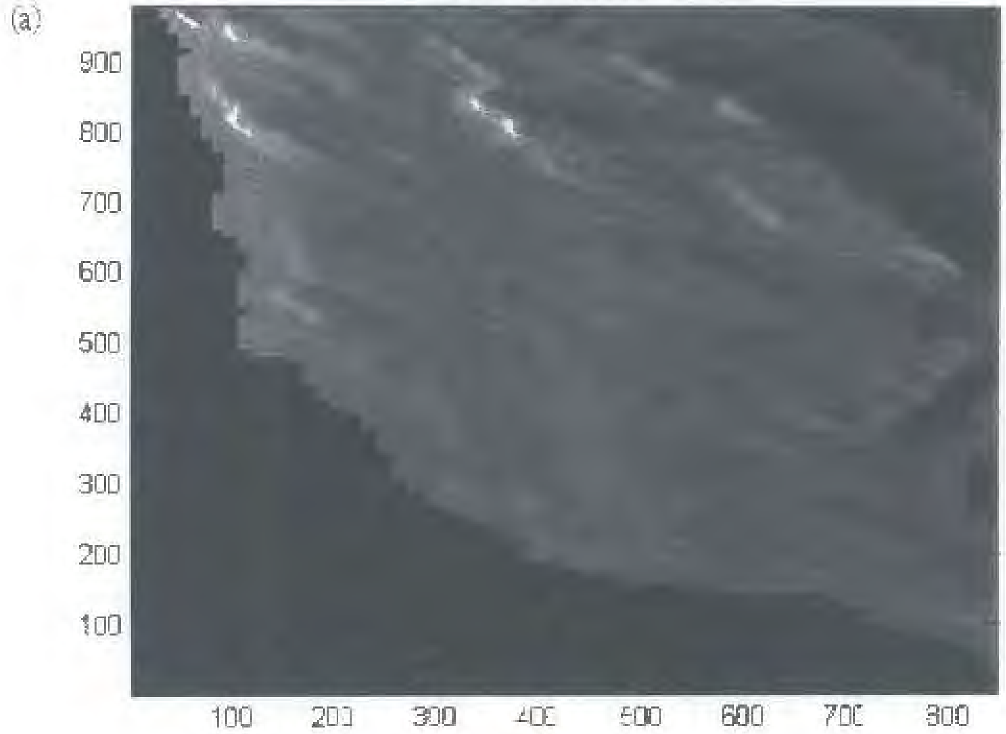

Expected Received Power

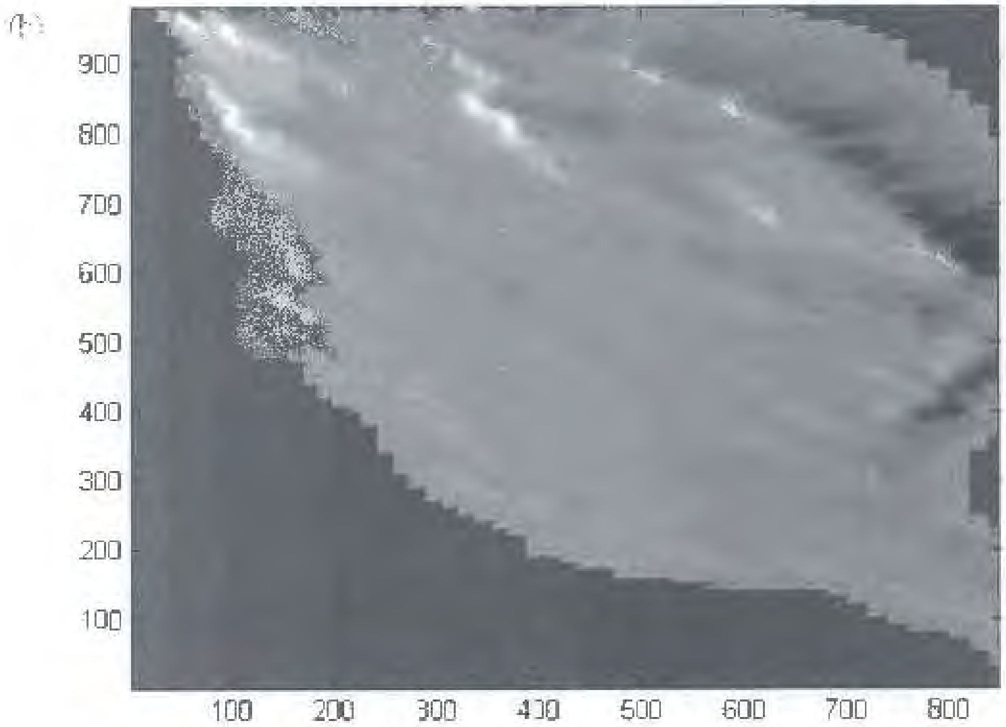

Figure 5.4 (a) the backscattering coefficient σ^0 and (b) the speckle-free power image (RCS $\sigma = \sigma^0 A_{res}$) of the scene.

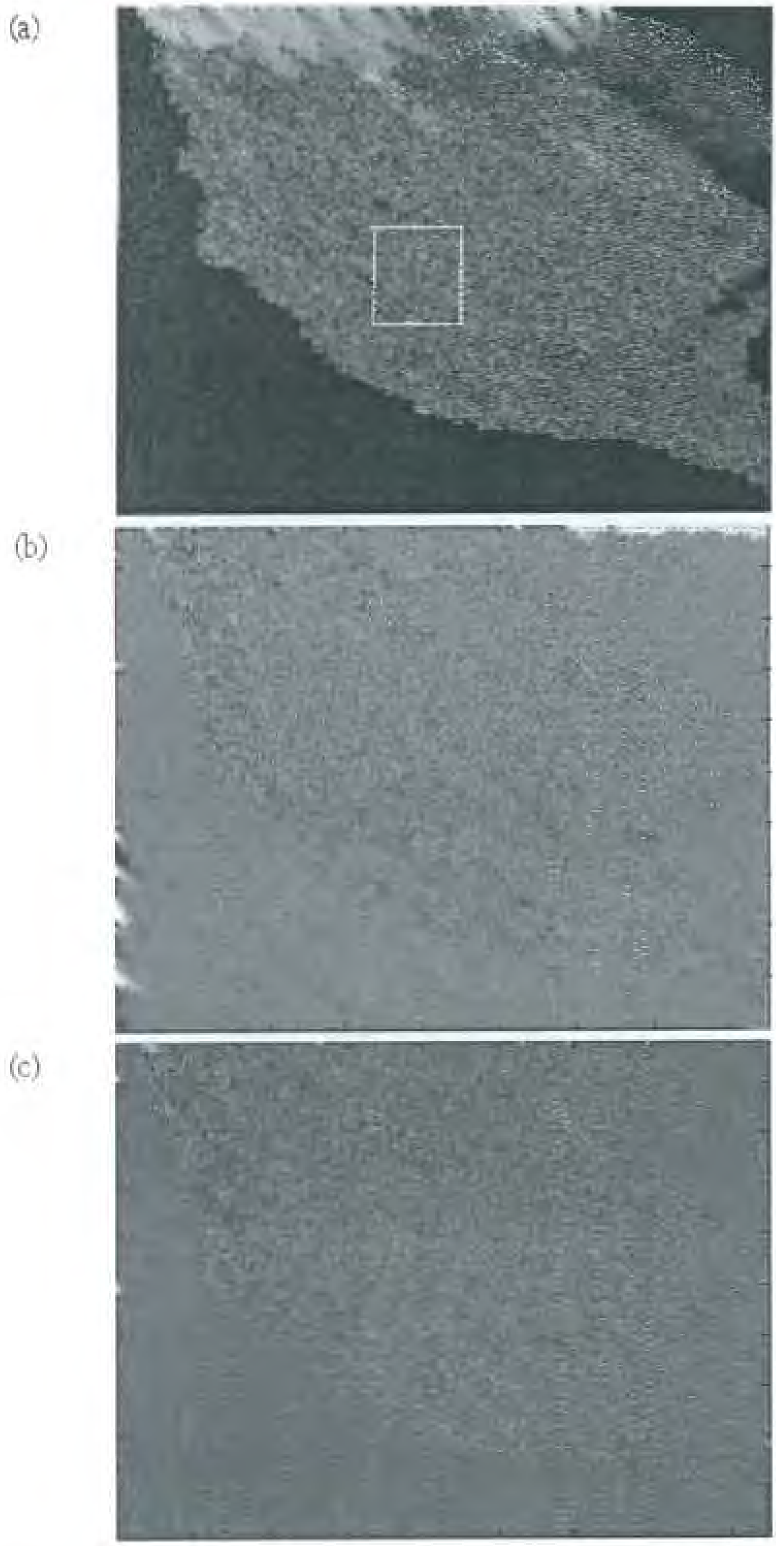

Figure 5.5 (a) the simulated power image and the corresponding (b) in-phase component (c) quadrature component.

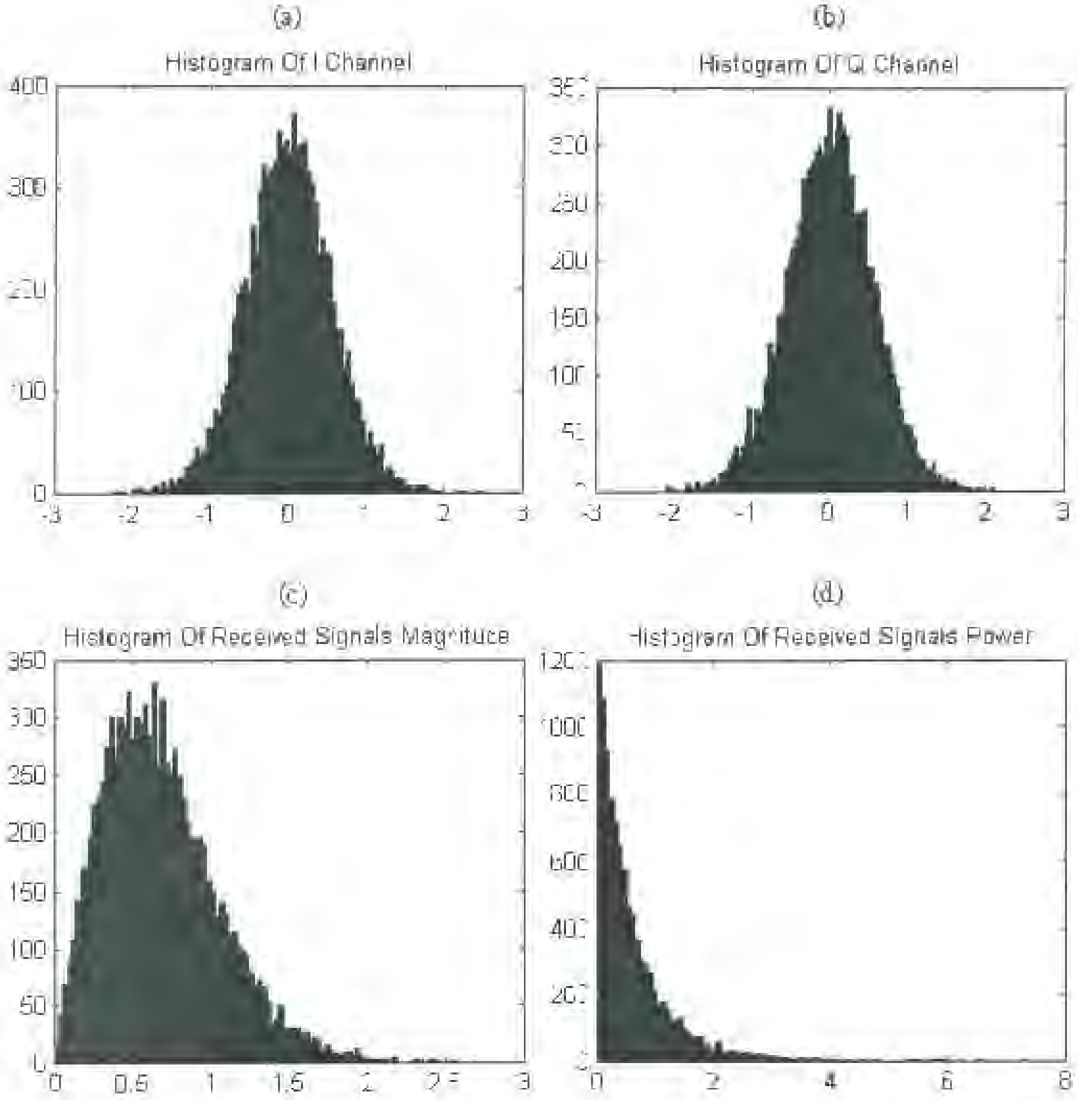

Figure 5.6 Histograms of signal distributions of a small portion enclosed by the rectangular region in Figure 5.5. (a) in-phase component, (b) quadrature-phase component, (c) magnitude component and (d) intensity component.

brighter on both images as well as the shadow region gives darker appearance.

- Figure 5.5 shows the speckled power image and the maps of the in-phase (real) and quadrature-phase (imaginary) component. Observe that the real and imaginary images show some structure of the scene but appear extremely noisy. Also the enclosed rectangular region in Figure 5.5(a) was used for accumulating the signal distribution properties for Figure 5.6.

- The signal distribution of various components was represented as histograms that show in Figure 5.6. These histograms were collected from the rectangular region in Figure 5.5(a) and followed the theoretical distribution described in Chapter 3.

5.2.2 Satellite SAR simulation

The satellite SAR simulation has image size of 1255×850 pixels (azimuth×range, approximately 82 km×18 km), with the scene covered by distributed rocks and soils. The parameters used in this simulation were indicated in Table 5.1. The incident angle at mid-swath is 23.27 degree and the radar beamwidth is approximately 1 degree. Descriptions of each figure were shown below:

- Figure 5.7 illustrates the region of observation of the satellite SAR simulation. Due to large scale contraction for the satellite imaging, the positions of radar are omitted from the image. However, an arrow was shown in Figure 5.7 to show the position of antenna related to the imaging area as well as the direction of flight. The flight trajectory in this simulation was based on the "C-band ERS-2 satellite Gamma Interferometric SAR" real data from European Space Agency with the sensor 796 km above the Earth's surface.

- The backscattering coefficient image 10log σ^0 in decibel scale, the shadow and layover maps for the simulated satellite case were shown in Figure 5.8. Observe that layover effect happened extensively along the areas near mountain ridge on the observed scene. The shadowing effect only occurred in the west region on the image, probably because a high steepness mountain was encountered.

- Figure 5.9 display the backscattering coefficient σ^0 map with the corresponding speckle-free power image. The mountain ridge appears brighter and the opposed side appears darker in both images.

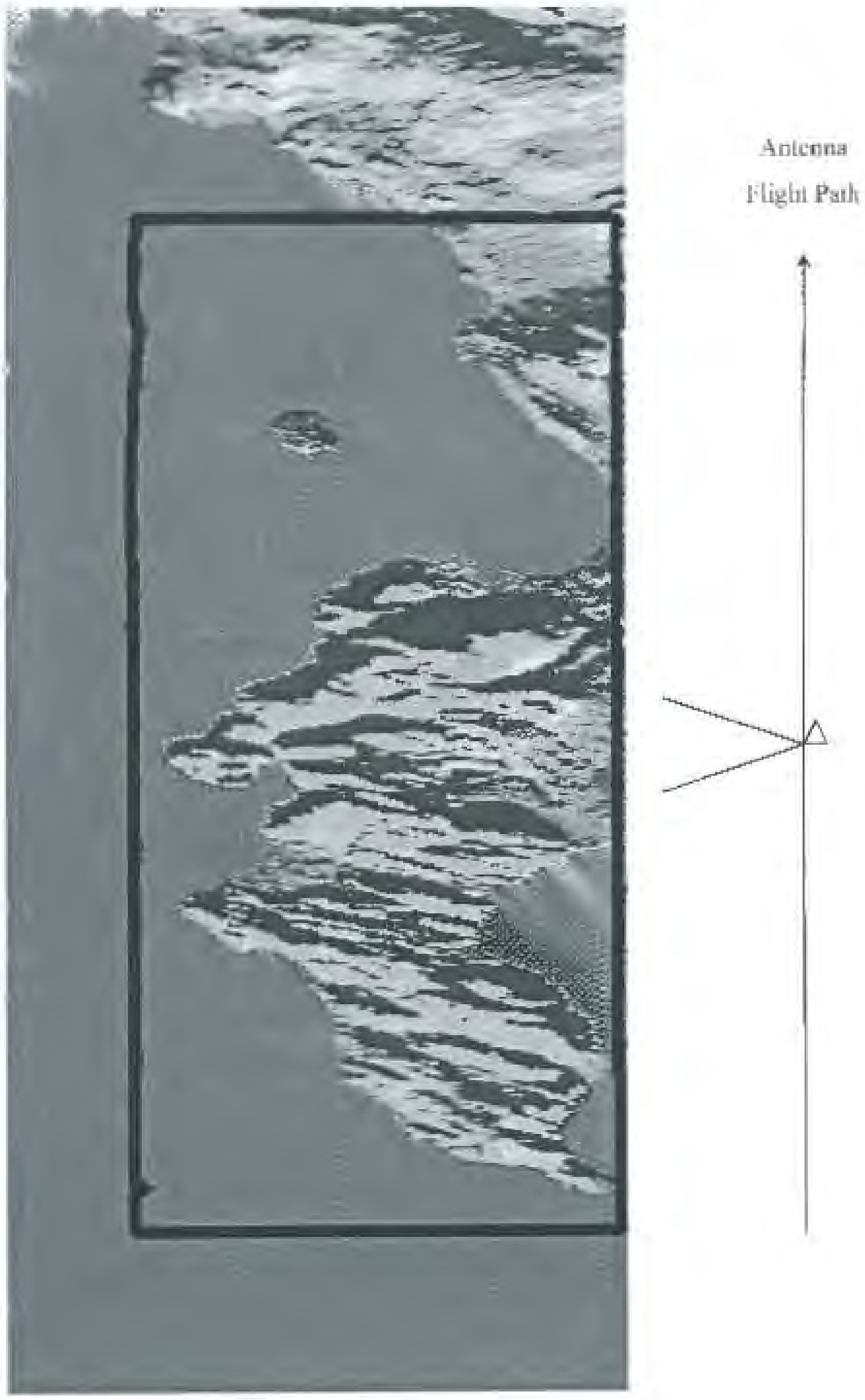

Figure 5.7 Imaging area of the satellite SAR simulation.

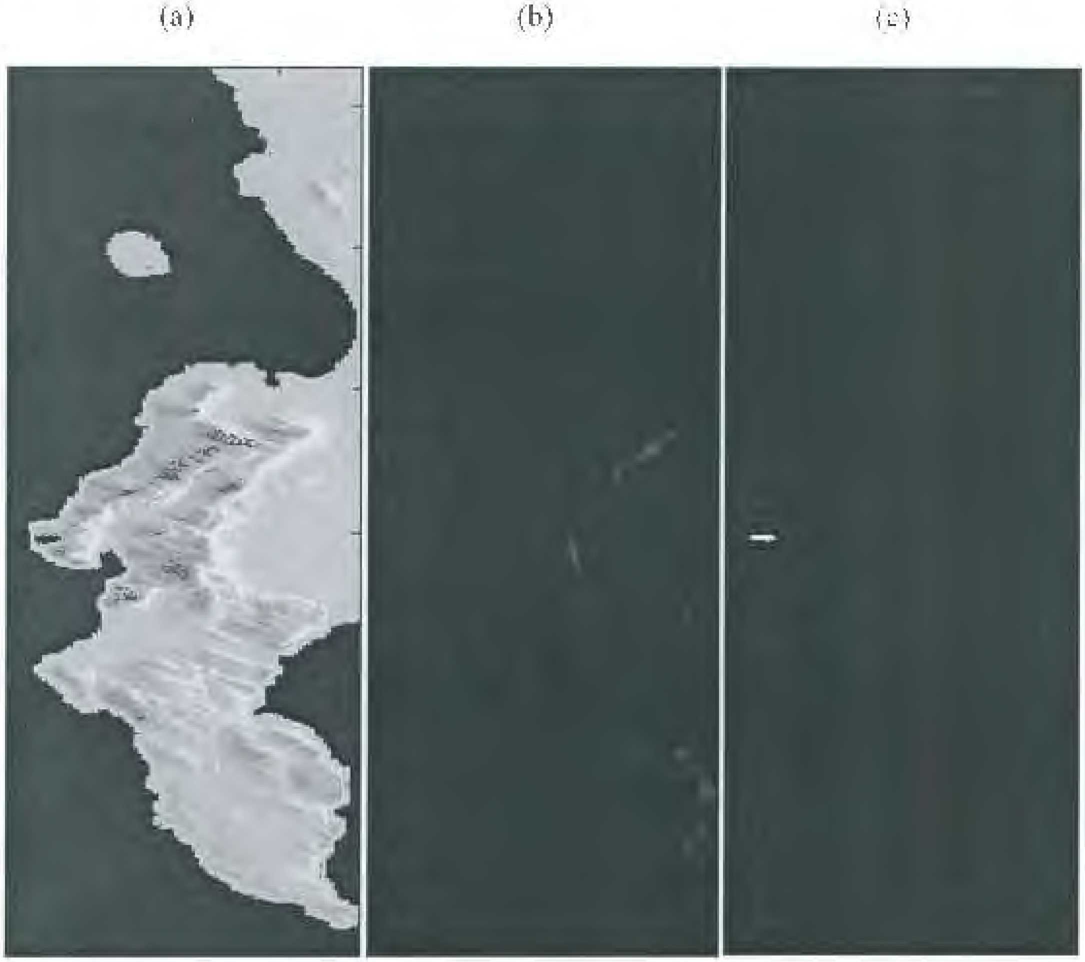

Figure 5.8 (a) backscattering coefficient of scene in dB scale 10log σ^0, (b) layover region and (c) the shadow map.

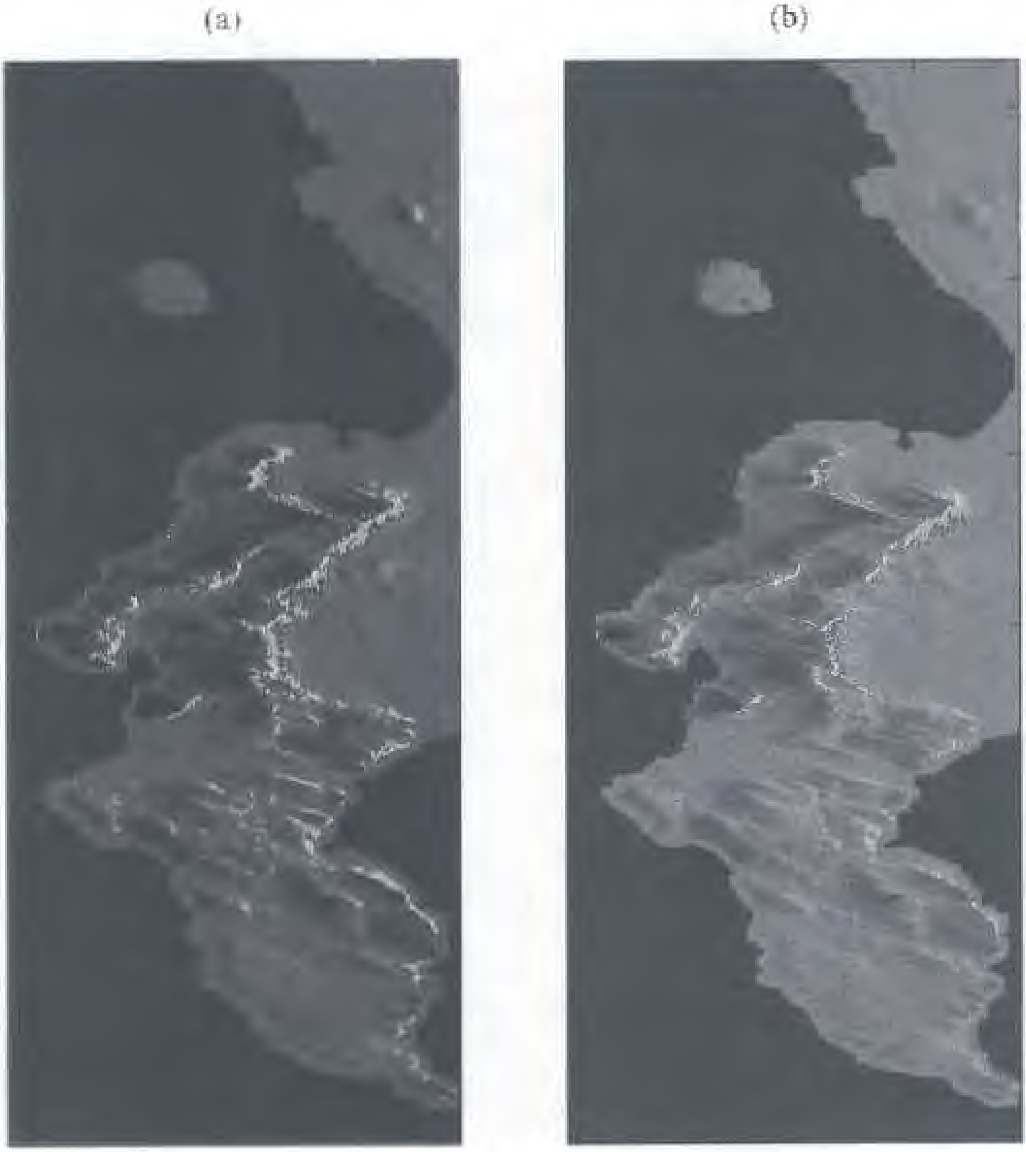

Figure 5.9 (a) the backscattering coefficient σ^0 image and (b) the speckle-free power (RCS $\sigma = \sigma^0 A_{GR}$) image.

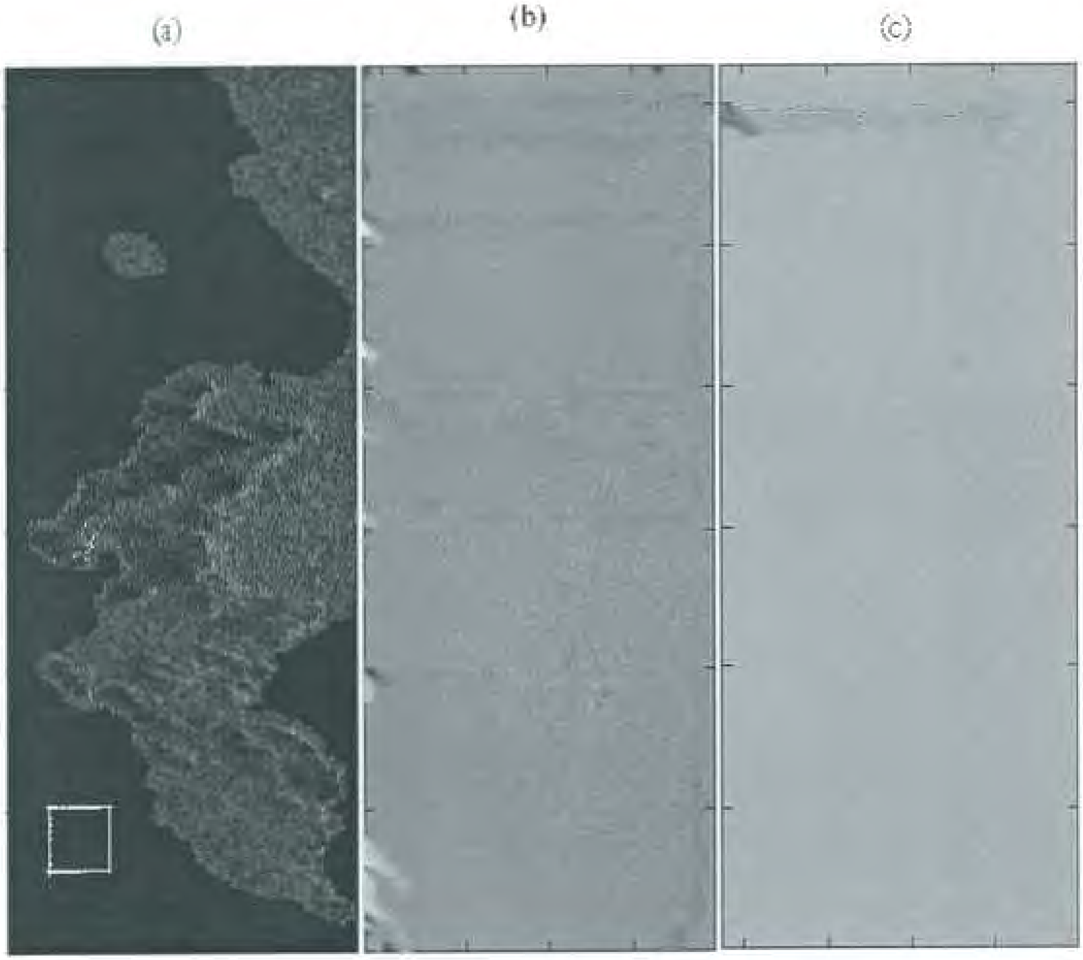

Figure 5.10 (a) the SAR power image, (b) in-phase and (c) quadrature-phase images.

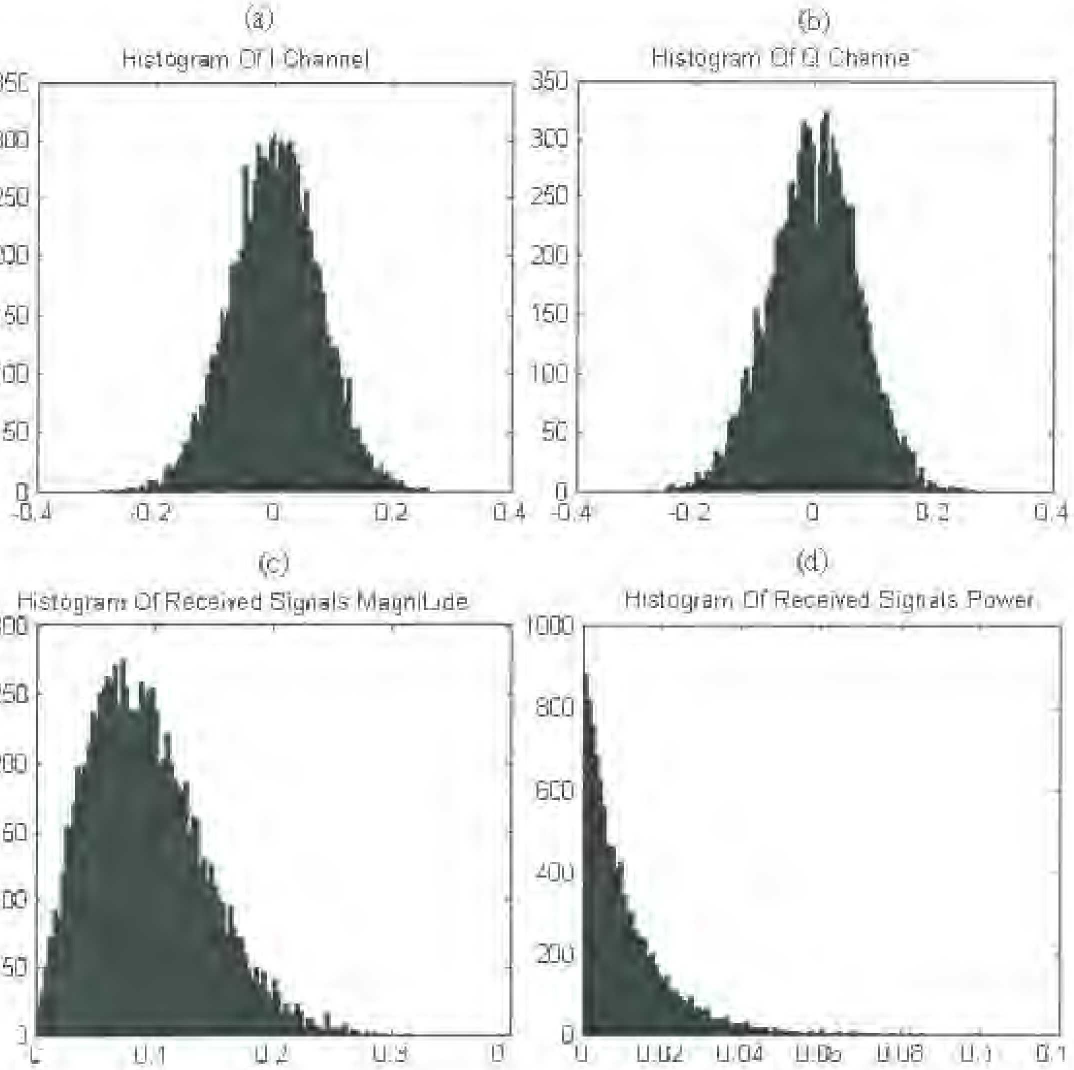

Figure 5.11 Histograms of signal distributions of a small portion enclosed by the rectangular region in Figure 5.10. (a) in-phase component, (b) quadrature-phase component, (c) amplitude component and (d) power component.

- Figure 5.10 illustrates the expected received power image of SAR and the I-Q components of the returned signal. Again, the real and imaginary images appear noisy; the source of this noisy appearance is due to the Gaussian random distribution nature of the returns, as described in Chapter 3. Notice that the samples within the rectangular region in Figure 5.10(a) were used for the signal distribution histograms in Figure 5.11.

- The signal distributions of the simulated satellite case were shown in Figure 5.11 using the information contained in the rectangular region in Figure 5.10(a). The resulting histograms shown in Figure 5.11 have the same distribution properties as described in Chapter 3, namely zero-mean Gaussian distribution for the in-phase and quadrature-phase component, Rayleigh distribution for the magnitude and negative exponential distribution for the received power.

The simulation log file of this satellite simulation can be found at Appendix A with complete simulated images at Appendix B.

5.3 Comparison of Simulated and Real SAR Image

To evaluate the accuracy and functionality of the simulator, comparison of the actual SAR image with the simulated one is necessary. The Cape Peninsula region was chosen to demonstrate the correctness of the simulator.

In order to accomplish the job, the state vectors from the "C-band ERS-2 satellite Gamma Interferometric SAR" real data from the European Space Agency were employed, as indicated in Table 5.2(a). The parameter t1 to t5 indicated 5 consecutive time intervals with the corresponding antenna position in (x, y, z). This state vector set were Earth-centered co-ordinate system, i.e. with the origin of the axes at the centre of Earth. Since the simulator was written to uses the ordinary xyz co-ordinate system as its default co-ordinate system, conversion of the state vectors should apply to the real data if one were to make use of them. A software named "XForm" was employed to achieve the co-ordinate system conversion. "XForm" is a multi-purpose co-ordinate transformation package designed for the African environment that was written by Charles Merry and Bruce Merry. The state vectors were transformed using XForm from Earth-centred Ellipsoidal system into the Gauss Conform Orthometric system.

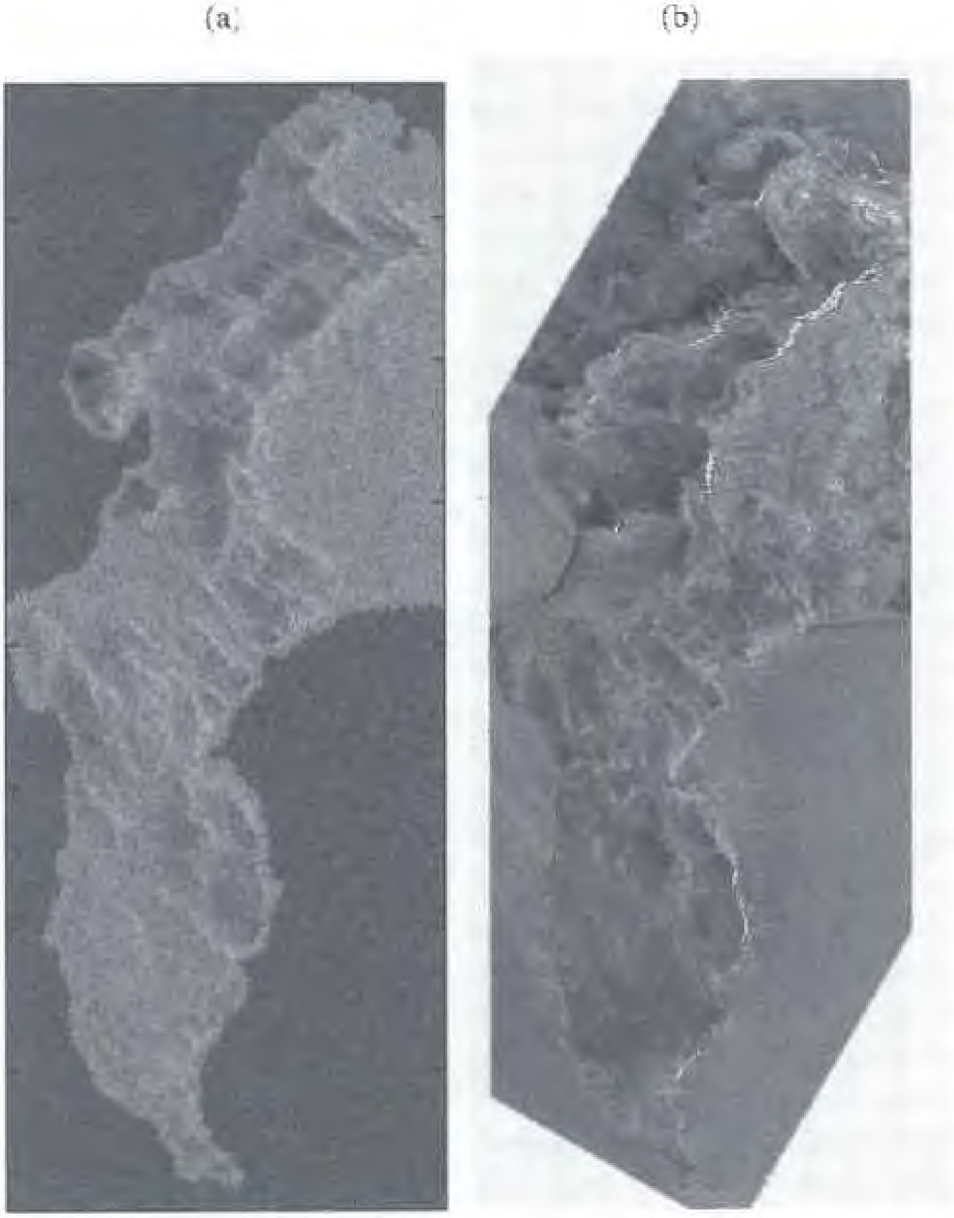

Figure 5.12 Comparison of the simulated and real ERS-2 SAR power image. (a) simulated image (b) real ERS-2 power image.

(a)

State Vectors	x	y	z
t1	5684736.2750	2425713.9060	-3631991.1970
t2	5599691.2570	2333105.1320	-3820173.3290
t3	5508814.7420	2238622.0430	-4004628.5590
t4	5412188.0470	2142381.9840	-4185177.8480
t5	5309898.5320	2044503.5910	-4361646.0640

(b)

State Vectors	x	y	z (Height)
T1	-394191.997	3392708.472	796139.194
T2	-340747.133	3586944.709	796871.602
T3	-287472.132	3781093.976	797616.969
T4	-234434.567	3975189.211	798399.041
T5	-181701.239	4169262.902	799154.839

Table 5.2 State vectors of antenna positions. (a) Earth-centered coordinates from ERS-2 and (b) converted "Lo" system, with the height above the sea level.

The converted state vectors were shown in Table 5.2(b) with the parameters T1 to T5 indicated 5 consecutive time intervals and the corresponding antenna coordinates arranged in (y ,x ,z [height]) above the sea level. This co-ordinate system was also known as the "Lo" co-ordinate system according to the software "XForm".

Figure 5.12 illustrates the simulated and the real ERS-2 SAR power images. Due to the assumption that the simulated region was covered by one single homogeneous distributed target (in this case, the imaging terrain type is rock and soil surface), the urban area at north-east part of the real SAR image does not appear in the simulated image. Furthermore, the appearance (image colour and the speckle effect) of two images are slight different, probably because the real data image was under some image processing routine to decrease the speckle effect and enhance the colour contraction.

5.4 Simulated SAR Images with Noise Effect

In this section, we will examine SAR images with the noise effect. Consider Figure 5.13 which shows the simulated speckle-free power (RCS $\sigma = \sigma^0 A_{GR}$) image with the receiver noise at the Cape Peninsula region in South Africa. The signal-to-noise (SNR) ratio at the mid-swath of these images are 100 (20 dB), 10 (10 dB) and 1 (0 dB) respectively. Below each simulated power images are a zoomed-in area enclosed by the rectangular region in the large simulated images.

As expected, the simulated image appears noisier as the signal-to-noise ratio at mid-swath drop dramatically. One important feature to notice on these images is that the additive noise since didn't follows the discussion presented in Chapter 4. That is, very noisy appearance at Far Range field and less noisy at the Near Range field due to the range compensation effect R^3 (where R is the range) which increases or decreases the additive noise. To answer this question, consider the range distance at the near field R_{near} and at the far field R_{far}. With the imaging sensor 800 km above the Earth surface, the mid-swath incident angle at approximately 23 degree and 1 degree beamwidth, the distance of the near range R_{near} and the far range R_{far} can be worked out by trigonometry as $R_{near} = 0.997\ R_{mid}$ (~866 km) and $R_{far} = 1.003 R_{mid}$ (~872 km), where R_{mid} (~869 km) is the range from radar to the mid-swath. The result shows that even the range compensation was applied, the additive noise power at the near range and the far range are only at $E\{|n(t)|^2\}_{\mathrm{near}} = (R_{near})^3\ E\{|n(t)|^2\}_{mid} = 0.991\ E\{|n(t)|^2\}_{mid}$ and $E\{|n(t)|^2\}_{far} = (R_{far})^3\ E\{|n(t)|^2\}_{mid} = 1.009\ E\{|n(t)|^2\}_{mid}$, with respect to the mid-swath noise power $E\{|n(t)|^2\}_{mid}$. Hence the resulting images show a nearly constant noise across the range.

Figure 5.14 illustrates the simulated speckled power images and three zoomed-in images with noise effect at SNR = 100 (20 dB), SNR = 10 (10 dB) and SNR = 1 (0 dB) respectively. Again as the SNR at the mid-swath drops, the image appears more noisy. Also notice that areas with weak received backscattered power were starts to being covered by the noise effect as SNR drops. This effect is particularly clear in Figure 5.14(c) as the appearance of the mountain ridges opposed to their brighter part becomes fainter and darker.

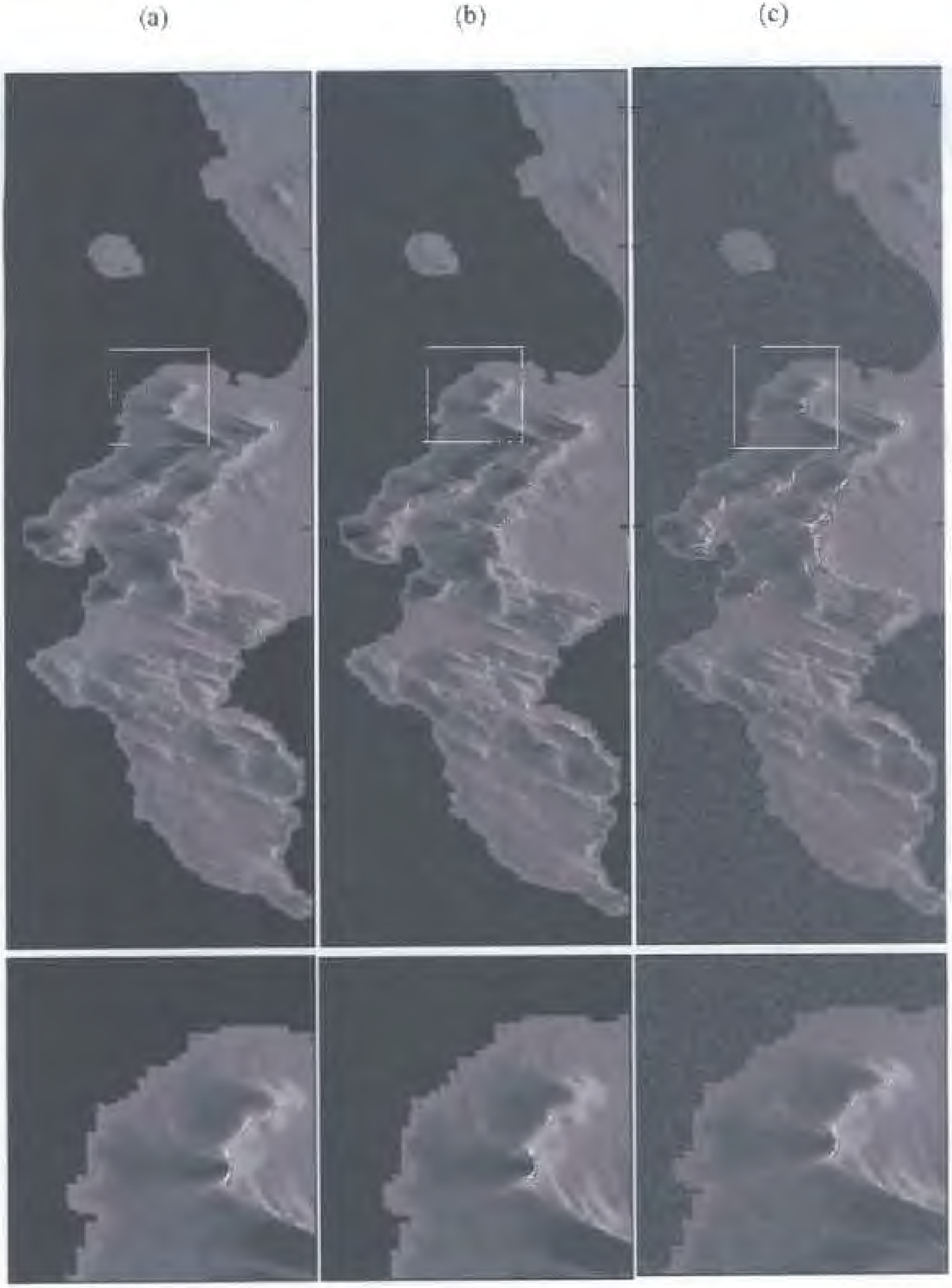

Figure 5.13 Speckle-free power (RCS $\sigma = \sigma^0 A_{GR}$) images with noise effect (σ^2_{noise}).
(a) $\mathrm{SNR}_{\text{mid-swath}} = 100$ (b) $\mathrm{SNR}_{\text{mid-swath}} = 10$ (c) $\mathrm{SNR}_{\text{mid-swath}} = 1$.

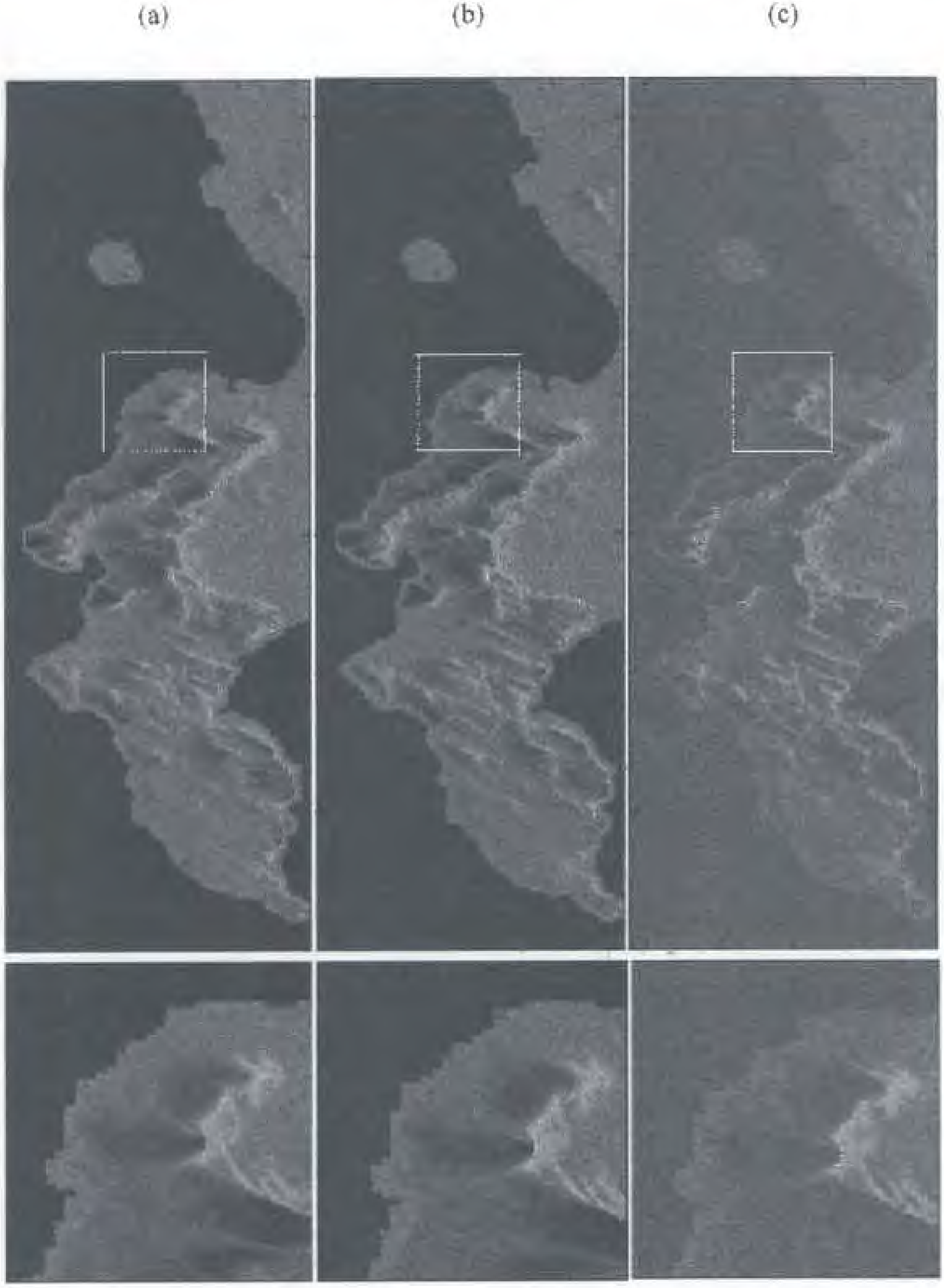

Figure 5.14 Speckled power images with noise effect (σ^2_{noise}). (a) $\mathrm{SNR}_{\text{mid-swath}} = 100$ (b) $\mathrm{SNR}_{\text{mid-swath}} = 10$ (c) $\mathrm{SNR}_{\text{mid-swath}} = 1$.

5.5 Effect of Antenna Flight Path on Produced Images

The effects of radar fly trajectory on the outcomes of Synthetic Aperture Radar images in the zero-Doppler plane can vary significantly even for imaging the same ground area. The purpose of this section is to examine this effect.

Figure 5.15 illustrates three backscattering coefficient σ^0 images and their corresponding antenna flight path. The size of the source DEM is 2200×440 pixels (azimuth ×range, this was interpolated from the original DEM with size 550×110 pixels) which correspond to geographical length of 111×22 km. The length deviations of the antenna flight path were also shown in Figure 5.15. Although the images were taken at more or less on the same ground area, the features on the large scale terrain appears differently. One can clear see from the images that some terrain features has been squeezed or stretched in length. These variations were caused by the simulated antenna when the radar sensor fly in a curved manner as indicated in Figure 5.15.

5.6 Conversion of Simulation Software from Matlab to C

In this section, we will examine the program execution times of the SAR simulator written in two different programming environments.

The original algorithms and calculations were done in the Matlab programming environment. This is because Matlab was convenient for mathematic and matrix calculation and allowed fast development of the code. However to improve the speed of the simulator, the software was rewritten into the C programming environment.

The running time of the simulator for each program language were shown in Table 5.3. The size of the simulation source DEM is 2200×440 pixels (azimuth ×range, this was interpolated from the original DEM with size 550×110 pixels) which correspond to geographical length of 111×22 km. The SAR simulations were completed on the same personal computer under two different operating system (OS), with the Matlab simulation runs under Windows 2000 OS and the C program simulation under Debian

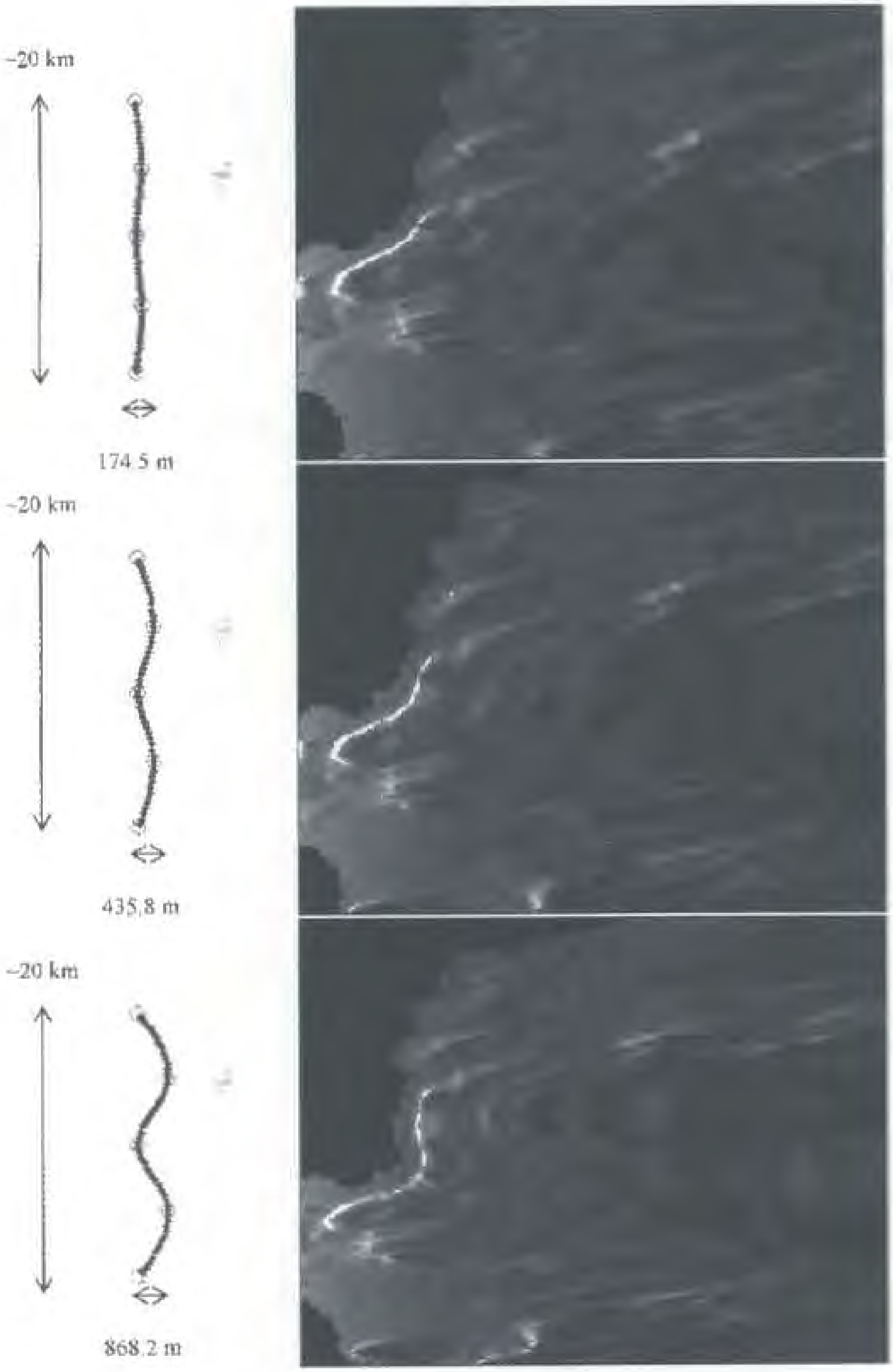

Figure 5.15 Antenna flight paths with the corresponding simulated backscattering coefficient σ^0 images.

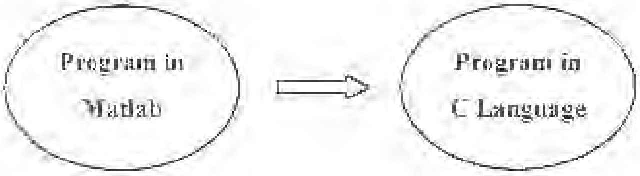

	Produced Image Size (Azimuth-Range)	**Simulation Execution Time**
Matlab 6.5	980×850	~45000 seconds
Linux gcc	980×850	~700 seconds

Table 5.3 Comparison of the software execution times for the simulator written in two different programming environments and runs on the same PC platform.

Linux 3. The personal computer uses an Intel Celeron 333 MHz CPU with 192 MB of RAM and 6.5 GB hard drive space (including two OS). The result shows that C has improved the execution time of the simulator for a factor of about 64 times.

If one considered, for example, an aircraft fling at the speed of 200 m/s (720 km/h) and operating with a PRF of 40 pulses per second (5 m azimuth sample spacing), the simulation times indicated in Table 5.3 (i.e. processing 1 range line per second for the C code) were not fast enough to achieve the "real-time" simulation. However, the simulator was tested and proved to run faster if one moves the simulation into a faster computer. In fact, the SAR simulator coded in Matlab programming environment runs at about 18000 second for the same simulation described in Table 5.3 (2.5 times faster) by using a computer with Intel Pentium III 700 MHz CPU and 320 Mb memories. This immediately gives us a way to improve the simulation speed. For a modern PC with a CPU at 3 GHz, it is possible to achieve 10 times fast simulation speed for the values indicated in Table 5.3. This will make both SAR simulators run faster and closes to the "real-time" simulation. Increasing the azimuth sample spacing to 50 metres (i.e. PRF = 4) which, for a large scale terrain imaging that yields visually similar results as the previous example, the simulator can easily achieves "real-time" simulation by using the existing code on a modern 3 GHz computer.

Chapter 6

Conclusions and Future Works

Conclusions

Based on the research and findings of this dissertation, the following conclusions may be drawn:

- The theories related to Synthetic Aperture Radar simulation have been studied; in particular, the geometric layout of the radar sensor and the observed scene: the signal processing and synthesis technique of SAR as well as the speckle interference effect of mapping areas with distributed target. The radar cross section of an object has great influence on the simulated power images, and accurate computation of its components, the backscattering coefficient and the slant range area, are critical to the success of simulation. The backscattering coefficient σ^0 was calculated from the empirical model (Ulaby and Dobson [8]) of real world radar observations and the slant range area of a ground patch was determined by vector geometry of the radar parameters.

- The simulation algorithms were derived from the geometry of the SAR observation system. In this dissertation a technique for scene-intersection was examined, which locates a set of sample points in the zero-doppler plane. Correct execution of this technique is important because the remainders of the simulation algorithms depend upon the accuracy of this sample taking method. Techniques to obtain the limitations of radar side-looking geometry such as layover and shadowing were also reviewed which further characterize the produced SAR images.

- A Synthetic Aperture Radar software program was created based on the algorithms derived and the simulated SAR images were presented for the case of airborne and spaceborne geometries. The backscattering coefficient σ^0 image reflects the strength of the return signals on the observed scene and provides as a basis to simulate SAR power image. The simulation images are evaluated by comparing the actual SAR images. It was confirmed that even a geometrical approach to the SAR system can produced accurate and visually realistic magnitude and power images. The statistics distributions of the images correspond to the theoretical speckle distribution.

- The effect of antenna flight path on the outcomes of the simulated SAR images was examined. It is found that the produced images tend to stretch or squeeze the large scale terrain features on the ground if a non-straight curved fly trajectory were presented. It further found that even straight fly trajectories with different approaching path will results different geographical arrangement of objects on the ground.

- The simulation software was prototyped in the Matlab programming language and later rewritten in the C programming environment to enhance the execution speed. It is found that the simulator runs comparatively faster (approximately 64 times faster) under the C environment. A processing speed of at least 10 range lines per second (containing 850 range samples) can be achieved on a modern 3 GHz computer. This is fast enough for real time simulation application.

Future Works

Based on the findings and conclusions of this dissertation, the future study of this project can be extended to include the following work:

- **Faster Algorithms** - evaluate possible improvements of the SAR simulation software to increases the speed and performance of the simulator. These include development of simpler and faster algorithms for the SAR simulator and better programming coding.

- **Incorporate the simulator with a flight simulator** – one could integrate the SAR simulator with a flight simulator (such as Microsoft Flight Simulator), which links the aircraft fly trajectory and the Earth's DEM in the flight simulator with the SAR simulator and produces real-time simulated SAR images as the user flies over the digitally stored terrain.

- **Synthetic Aperture Radar Interferometry (InSAR)** - the SAR simulator could be expended to include a SAR interferometric facility.

Appendix A

Simulation Log File

The simulation log file is a text file that produced by the simulator after simulation and display information concern about the simulation.

Simulation log file:

```
Observed scene image size:   441 - 2229     pixels

Image spacing:   50     metres

%%%%%%%%%%%%%%%%%%%%%%%%%%%%%%%%%%%%

Number of state vector:   5

State vector interval:   30     second

Time of first state vector:   31050.00000     second

Time state vector start:   31100.22405     second

Time state vector end:   31112.77195     second

%%%%%%%%%%%%%%%%%%%%%%%%%%%%%%%%%%%%
```

state_vector_position 1 = [-287472.132 ,3392708.472 ,796139.194] meter
state_vector_position time 1: 31050 - 31080 second

state_vector_position 2 = [-287472.132 ,3586944.709 ,796871.602] meter
state_vector_position time 2: 31080 - 31110 second

state_vector_position 3 = [-287472.132 ,3781093.976 ,797616.969] meter
state_vector_position time 3: 31110 - 31140 second

state_vector_position 4 = [-287472.132 ,3975189.211 ,798399.041] meter
state_vector_position time 4: 31140 - 31170 second

state_vector_position 5 = [-287472.132 ,4169262.902 ,799154.839] meter
state_vector_position time 5: 31170 second

%%%%%%%%%%%%%%%%%%%%%%%%%%%%%%%%%

Antenna near angle: 22.76 degree

Mid-Swath angle: 23.2738 degree

Antenna far angle: 23.7875 degree

Pulse repetition frequency: 100 Hz

Pulse repetition time: 0.01 second

Signal-to-Noise Ratio at mid-swath: 100

Terrain type: Soil and Rock Surface

Carrier frequency: C band

%%%%%%%%%%%%%%%%%%%%%%%%%%%%%%%%%

Shadow occur: Yes

Layover occur: Yes

Simulation time: 2.2906e+004 second

Produced image size: 850 - 1255 pixels (Range - Azimuth)

Slant range spacing: 8 metres

Asimuth spacing: 65 metres

End of simulation log file

Appendix B

Complete Simulation Results

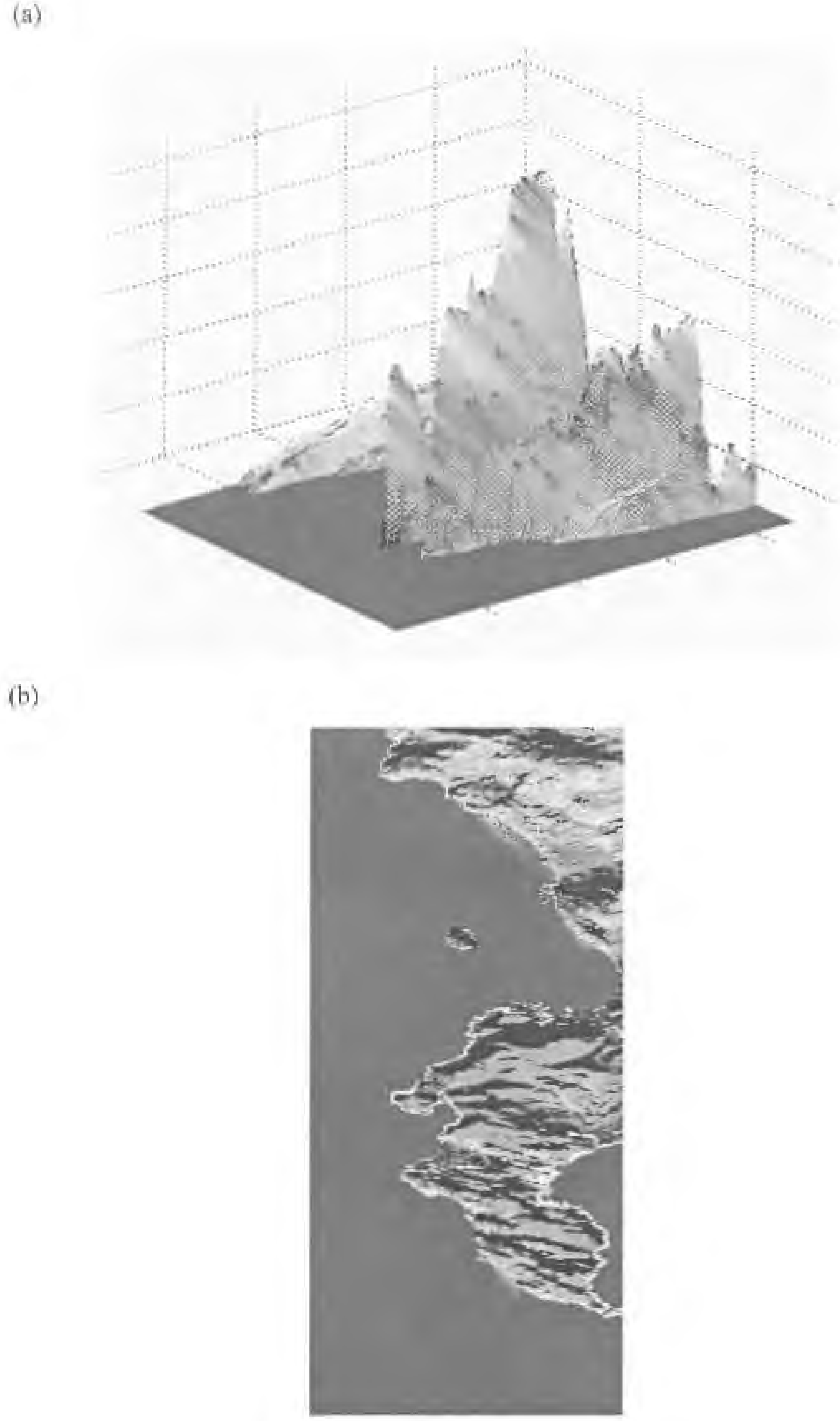

Figure B.1 Digital Elevation Model of Cape Peninsula (a) 3D side view (b) top view.

Figure B.2 Area of scanning of the SAR for the simulation.

Figure B.3 Map of shadowing area of the simulated scene.

Figure B.4 Map of the layover region.

Figure B.5 Simulated backscattering coefficient in decibel scale.

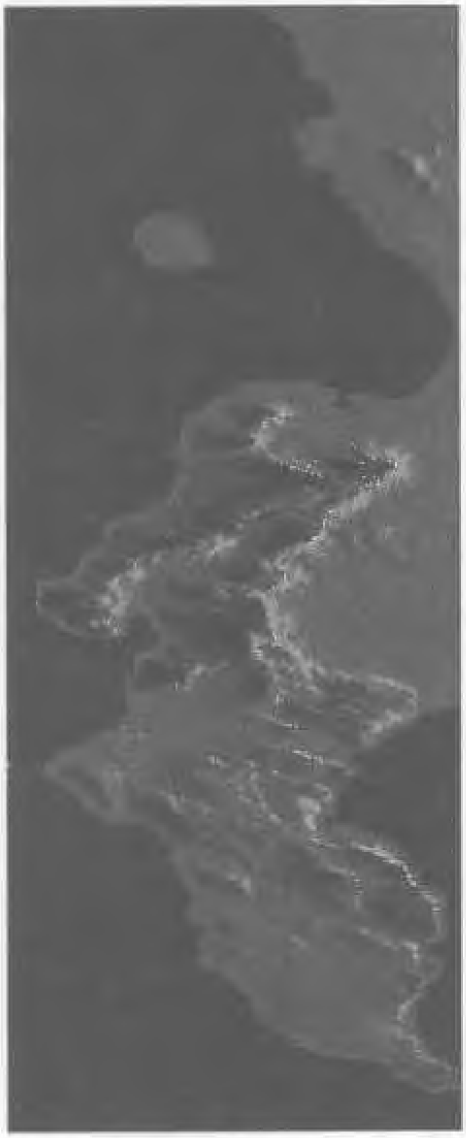

Figure B.6 Map of backscattering coefficient (sigma naught), unit-less.

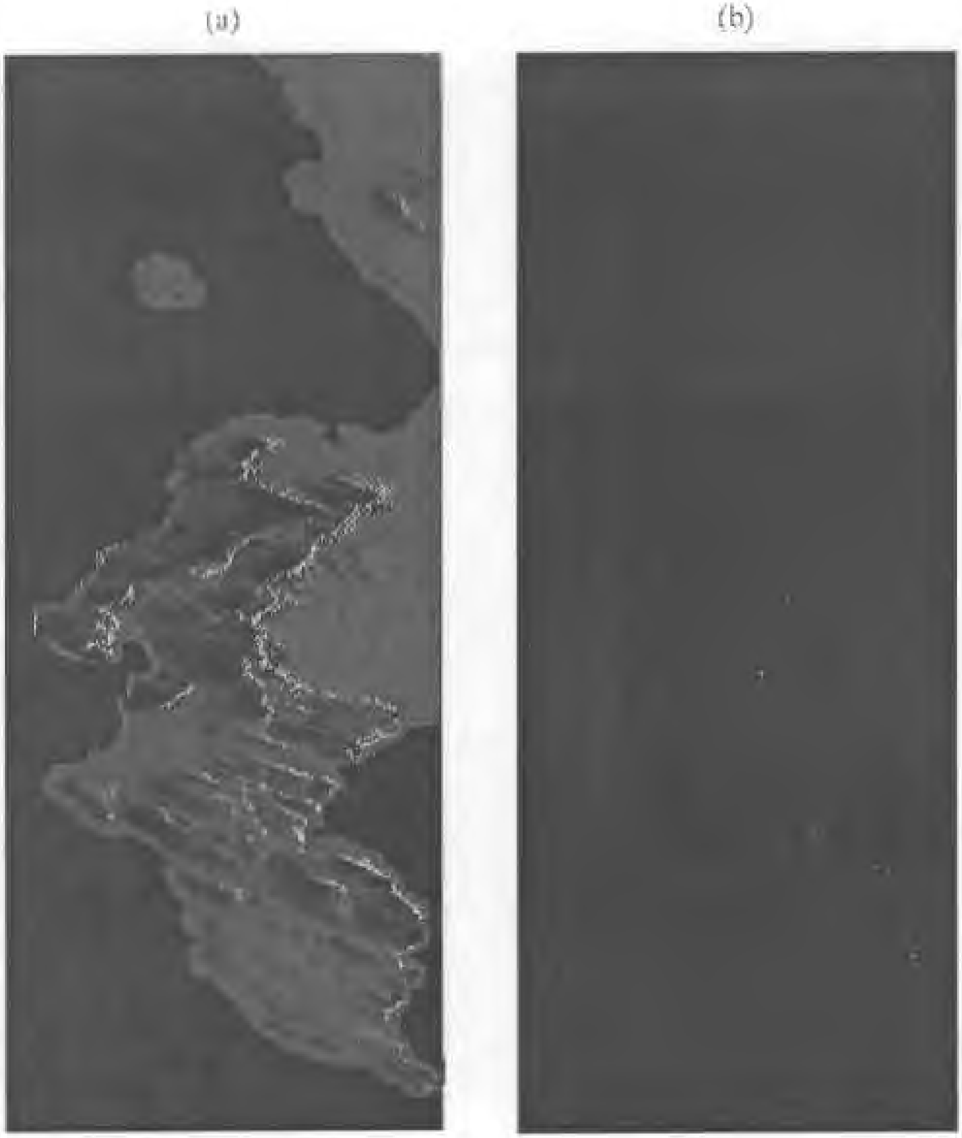

Figure B.7 Simulated speckle-free power image. (a) A forth rooted version of the original power image to show a better terrain aspect (b) original power image.

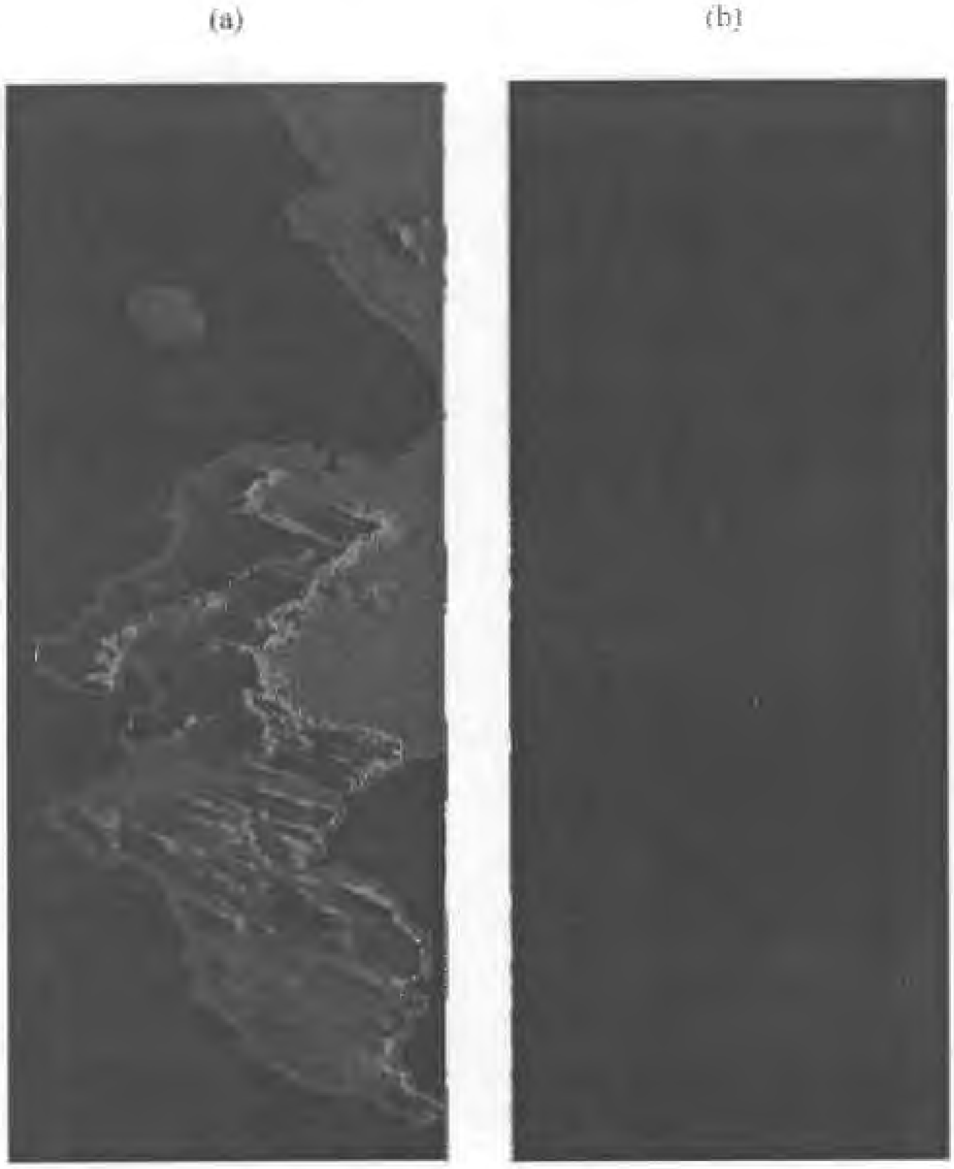

Figure B.8 Simulated speckle-free power image compensated with the range effect. (a) A forth rooted version to display a better land aspect (b) original power image.

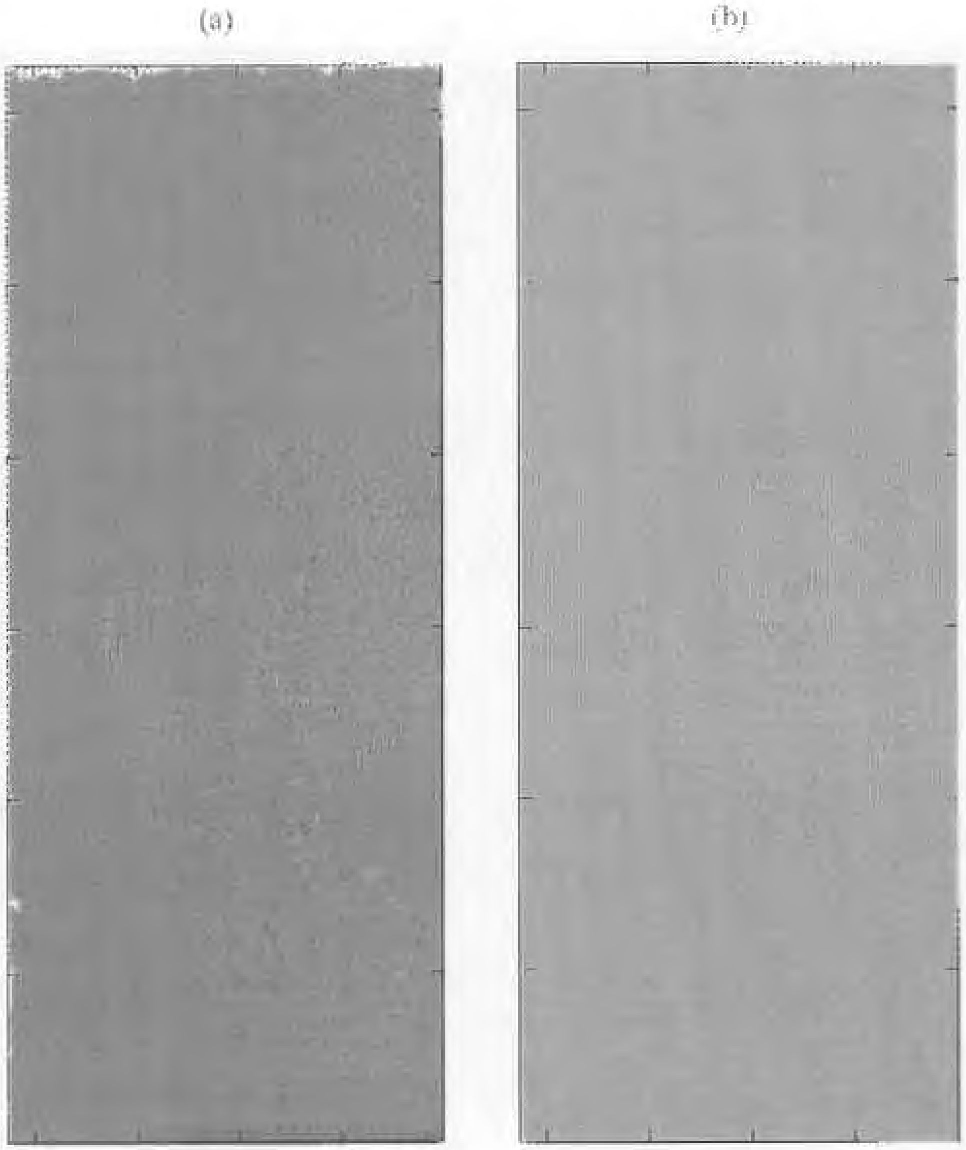

Figure B.9 Complex SAR images for the I-Q channel. (a) In-phase component (b) Quadrature-phase component.

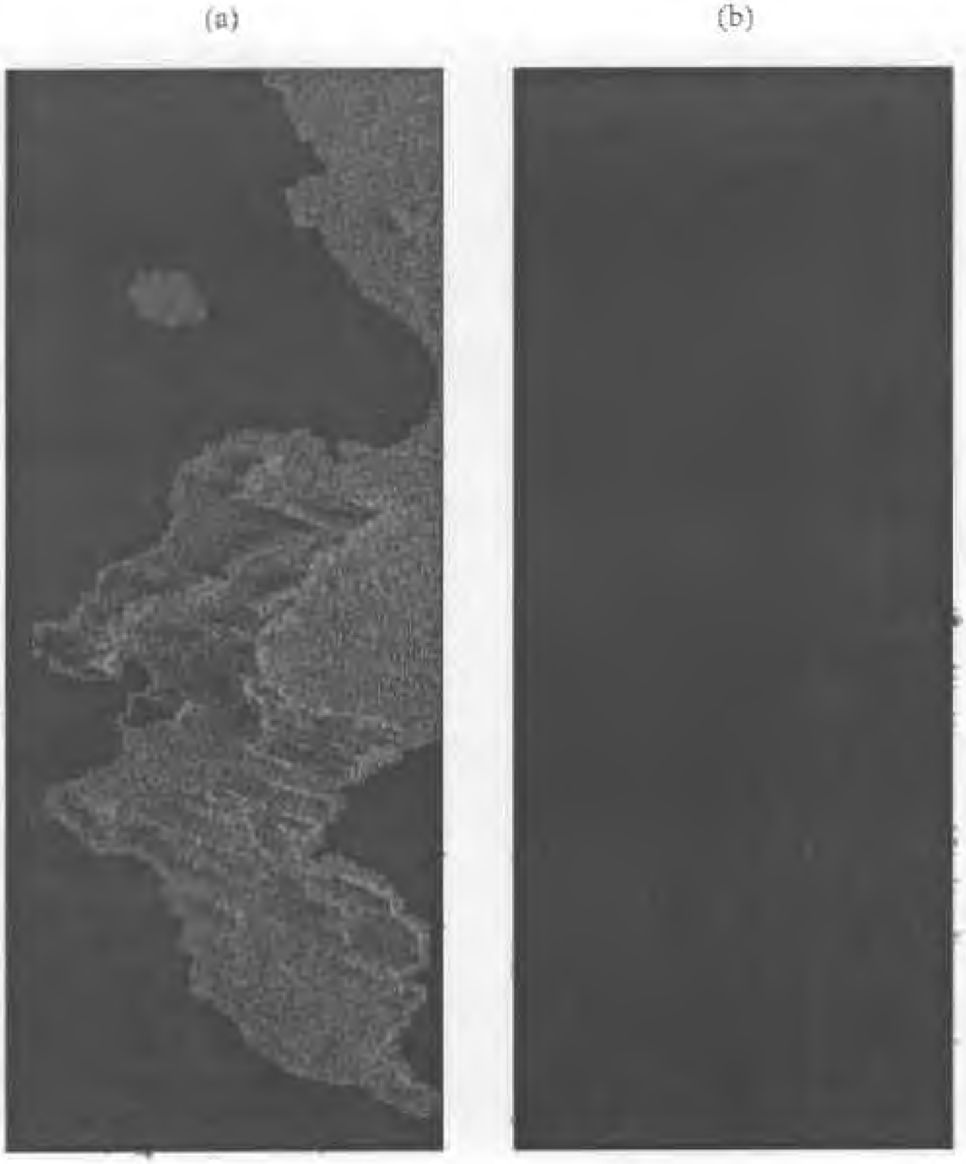

Figure B.10 Simulated SAR magnitude images. (a) Forth rooted version of original image (b) original magnitude image.

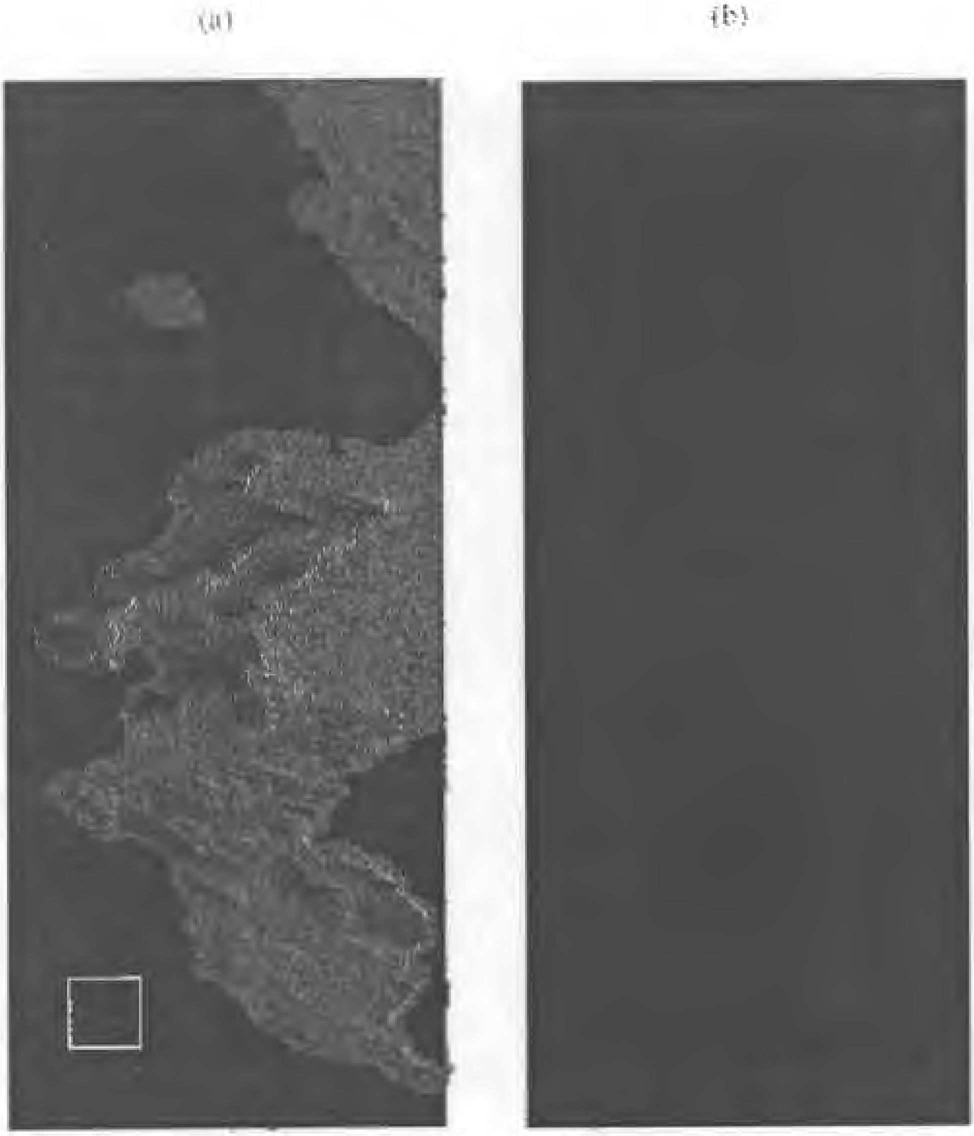

Figure B.11 Simulated SAR power images. (a) Forth rooted version of original image to display a better land aspect (the enclosed rectangular region is used for the signal distributions for the following four figures) (b) original power image.

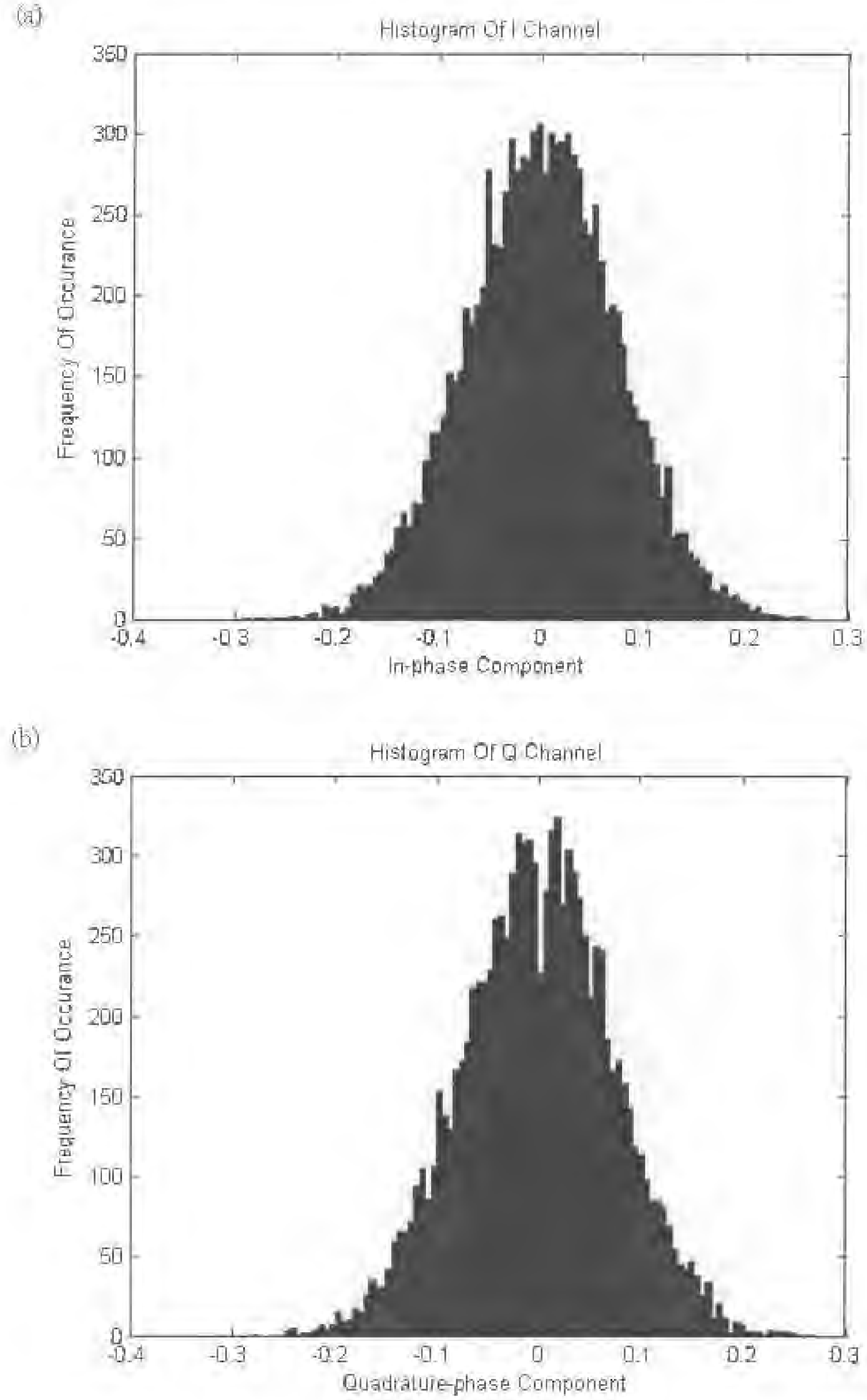

Figure B.12 Histogram of (a) In-phase component (b) Quadrature-phase component.

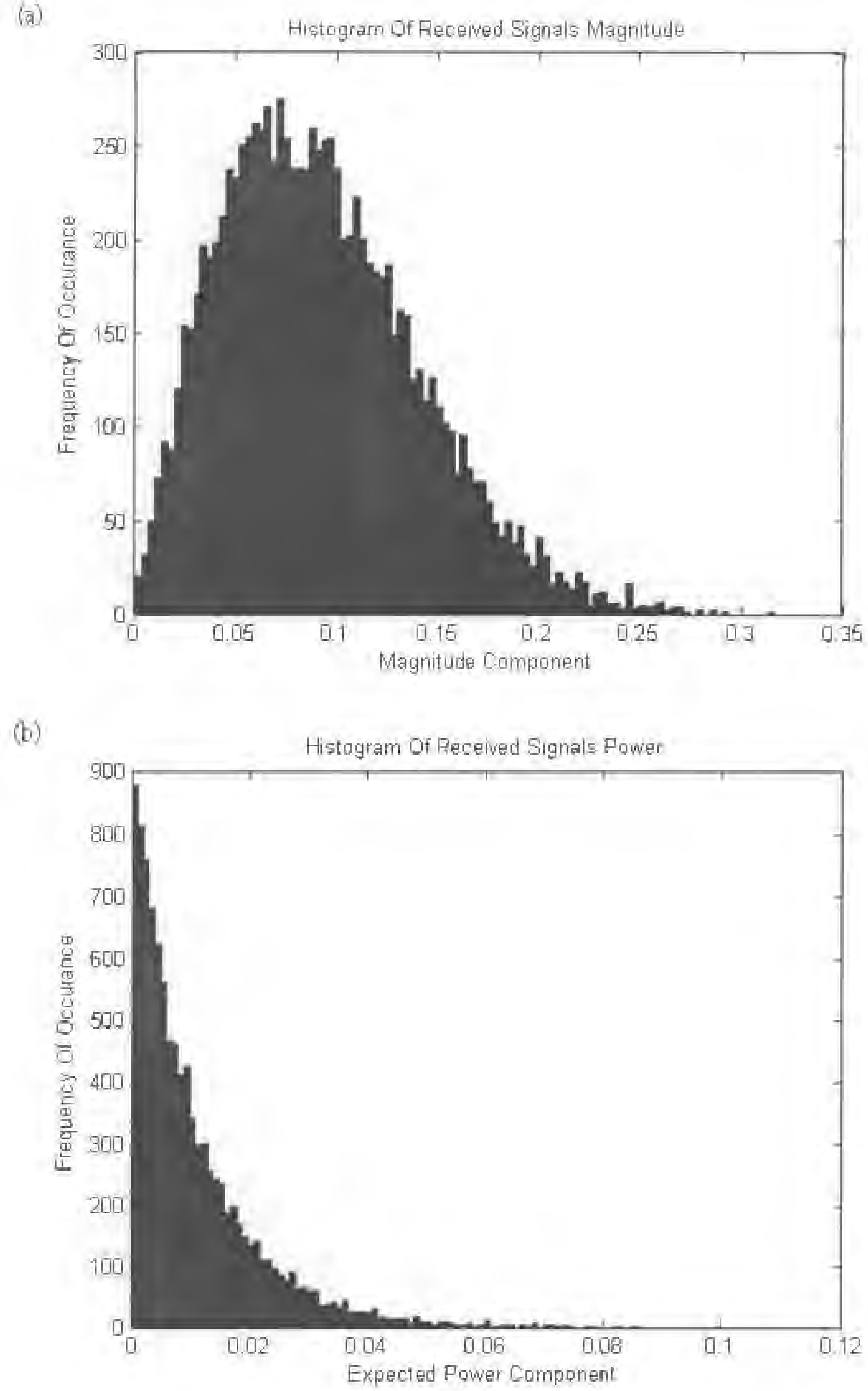

Figure B.13 Histogram of (a) Amplitude and (b) Intensity.

Appendix C

Empirical Model of Backscattering Coefficient

This section displays the empirical model of the backscattering coefficient σ^0 from Handbook of Radar Scattering Statistics for Terrain [8], a model that has been used throughout the simulation of this dissertation. The figures were generated by Matlab program using linear interpolation, with the circles represents the values obtained from [8].

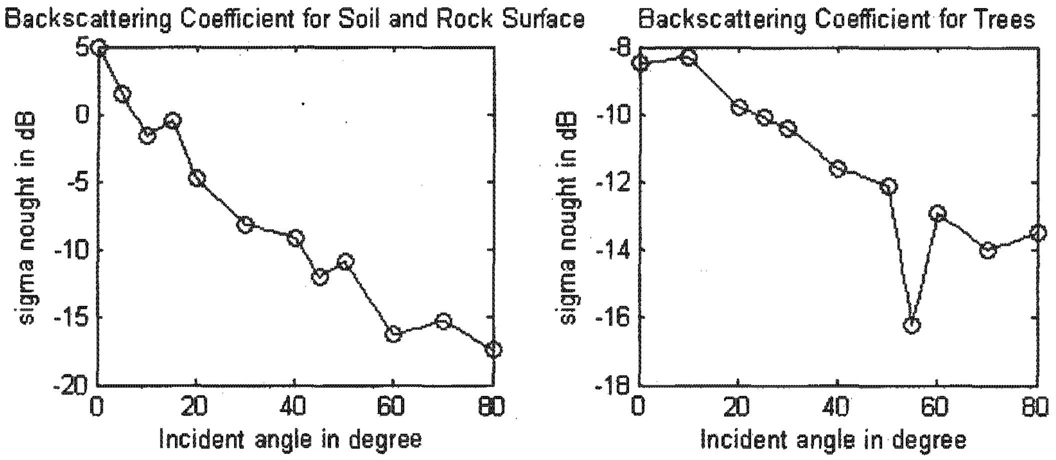

(a)

(b)

Figure C.1 Backscattering Coefficient at X band, HH polarization. (a) Soil and Rock Surface (b) Tree Surface.

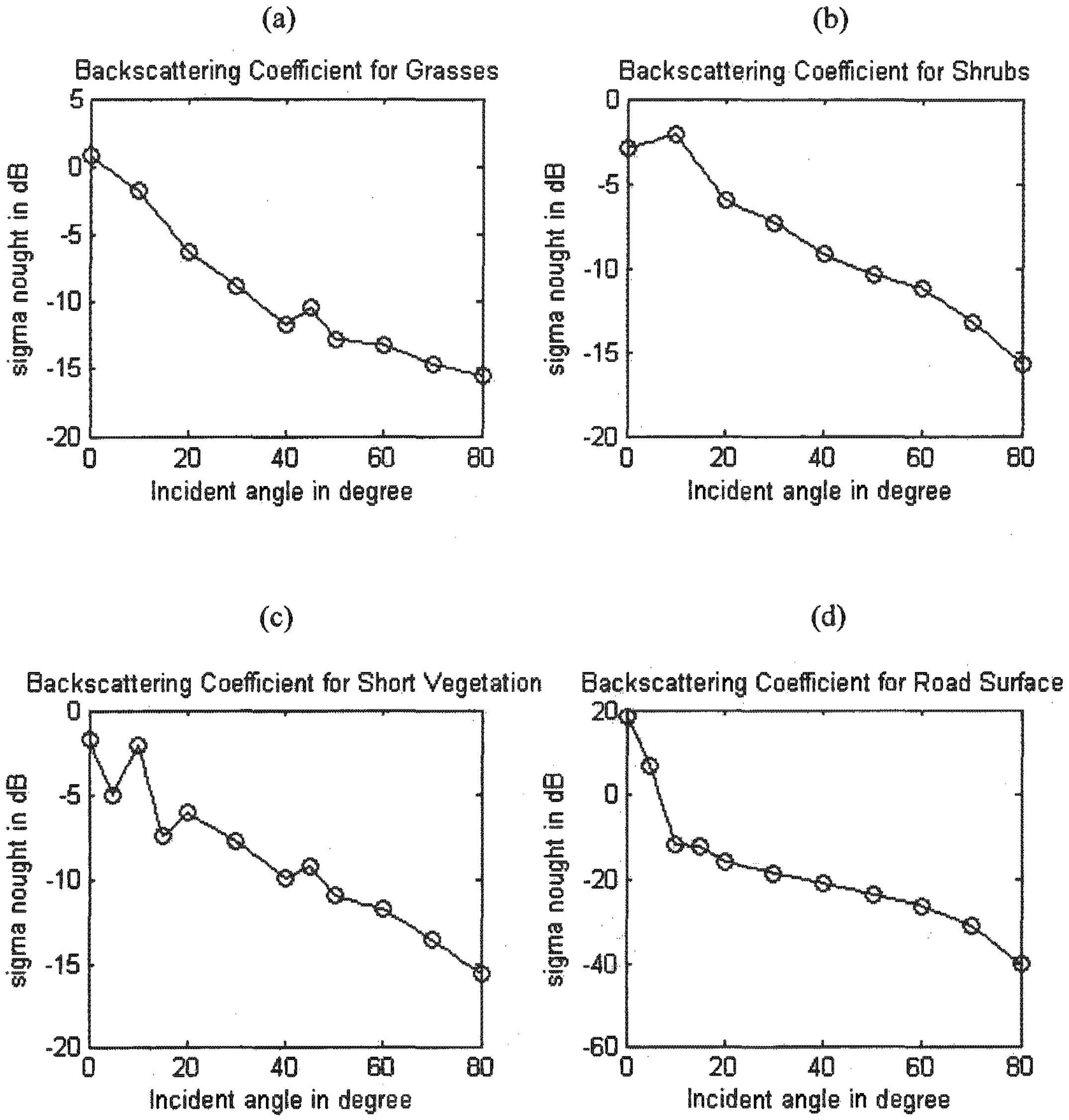

Figure C.2 Backscattering Coefficient at X band, HH polarization. (a) Grass Land (b) Shrub Surface (c) Short Vegetation (d) Road Surface.

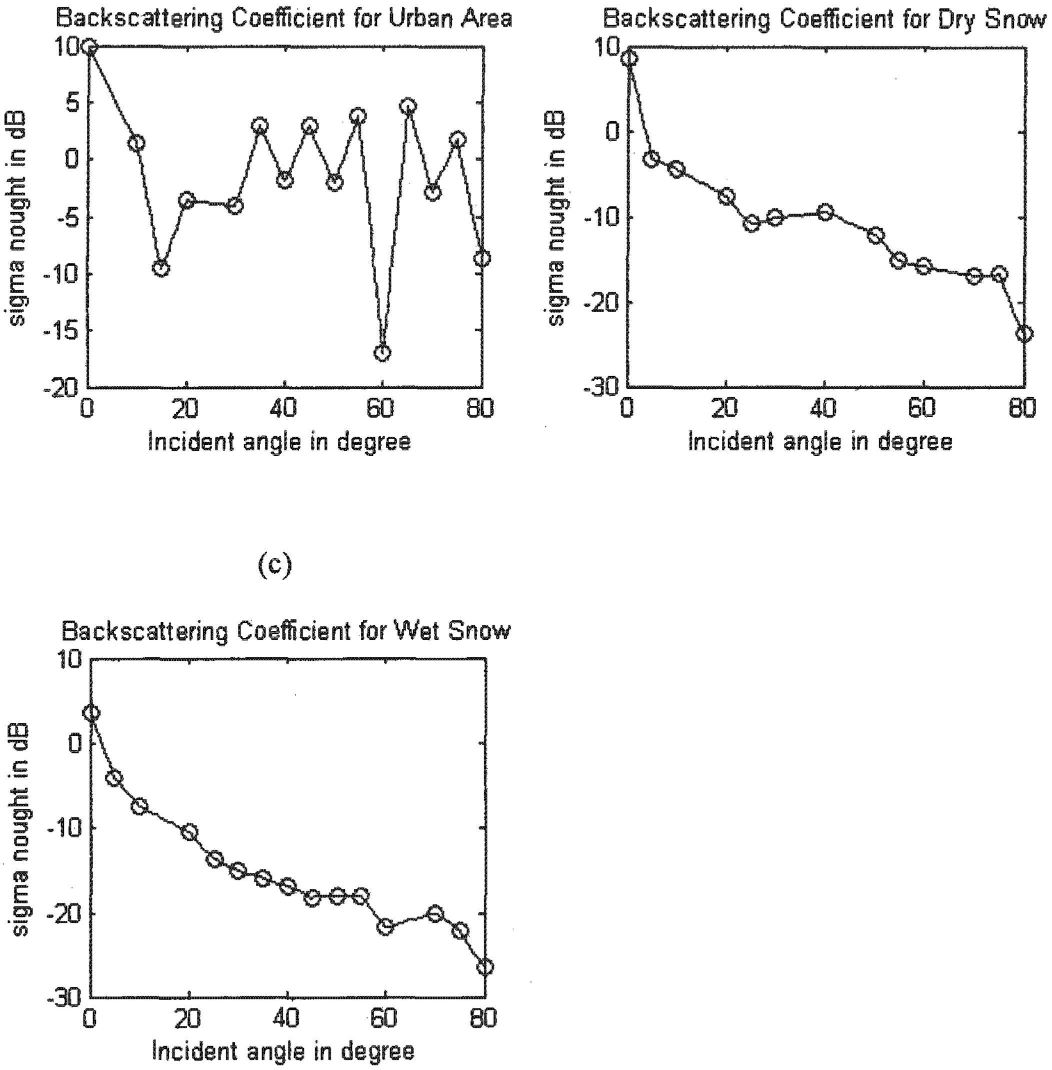
(a)

Backscattering Coefficient for Urban Area

(b)

Backscattering Coefficient for Dry Snow

(c)

Backscattering Coefficient for Wet Snow

Figure C.3 Backscattering Coefficient at X band, HH polarization. (a) Urban Area (b) Dry Snow Surface (b) Wet Snow Surface.

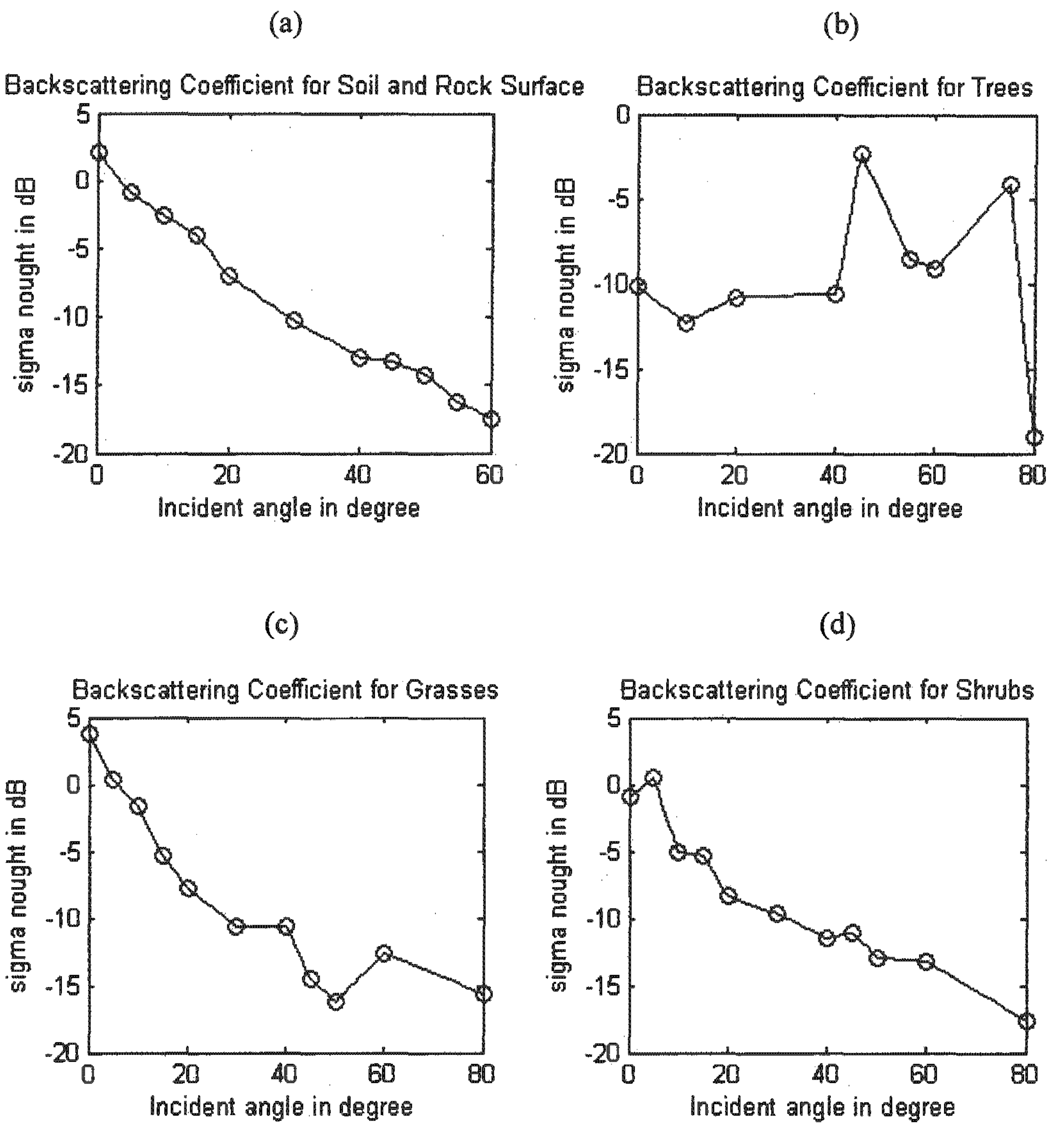

Figure C.4 Backscattering Coefficient at C band, VV polarization. (a) Rock and Soil Surface (b) Trees (c) Grass Land (d) Shrub Surface.

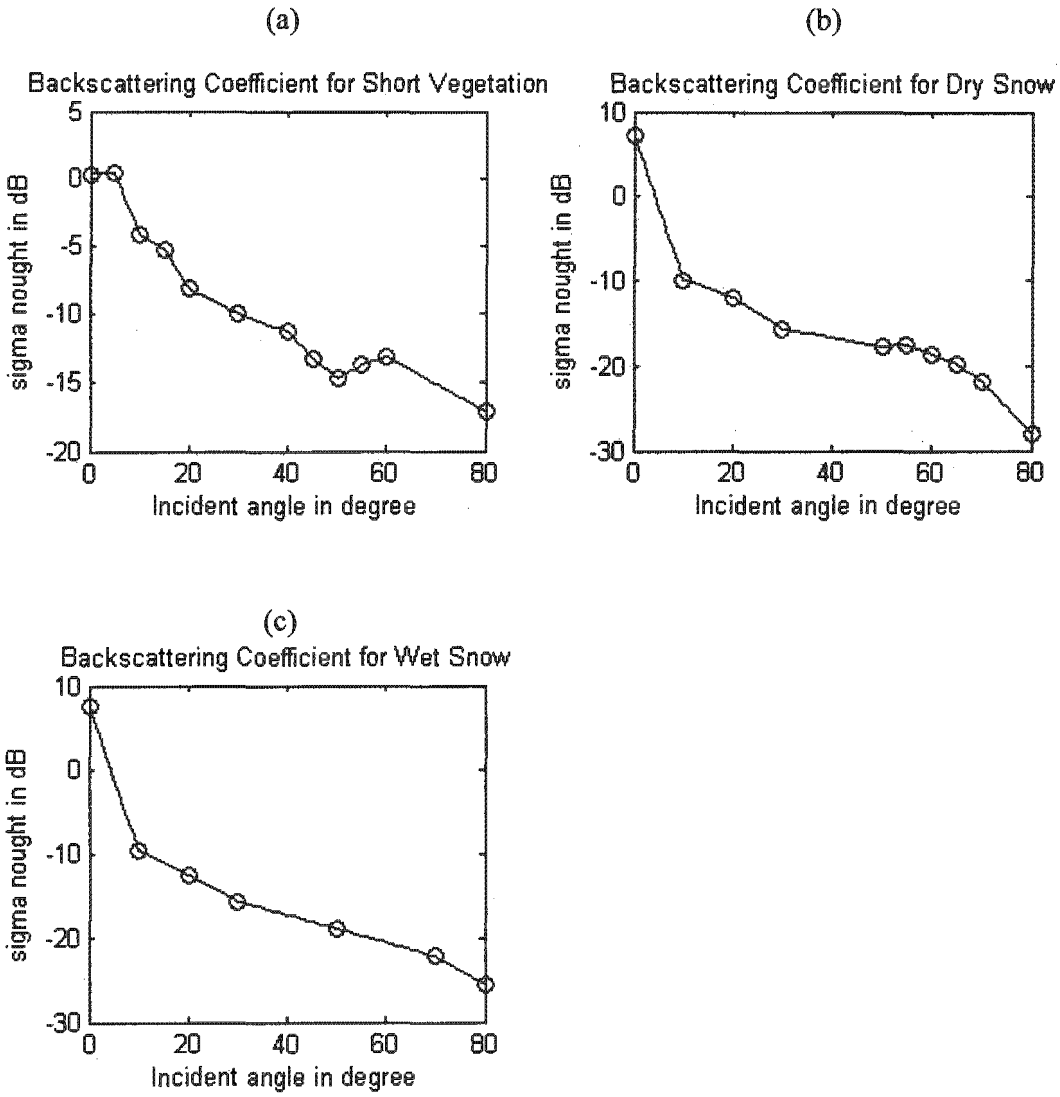

Figure C.5 Backscattering Coefficient at C band, VV polarization. (a) Short Vegetation (b) Dry Snow Surface (c) Wet Snow Surface.

Bibliography

[1] J. Curlander and R. McDonough. Synthetic Aperture Radar Systems and Signal Processing. John Wiley and Sons, New York, 1991.

[2] C. Oliver and S. Quegan. Understanding Synthetic Aperture Radar Images. Artech House Remote Sensing Library. Artech House, Norwood, MA, 1998

[3] Lisa S Wray. Synthetic Aperture Radar Image Simulator for Interferometry. Master's Thesis, Department of Electrical Engineering, University of Cape Town, February 2001.

[4] C. Olmsted. Alaska SAR Facility Scientific SAR User's Guide. July 1993.

[5] F. Ulaby, R. Moore and A. Fung. Microwave Remote Sensing – Active and Passive Volume I - II, I: Microwave Remote Sensing Fundamentals and Radiometry, II: Radar Remote Sensing and Surface Scattering and Emission Theory. Addison-Wesley Publishing, 1982.

[6] Eugene F. Knott, John F. Shaeffer and Michael T. Tuley. Radar Cross Section – Second Edition. Artech House, 1993.

[7] R. Balmer and P. Hartl. Synthetic Aperture Radar Interferometry. February 1998.

[8] F. Ulaby and M. Dobson. Handbook of Radar Scattering Statistics for Terrain. Artech House, 1989.

[9] Andrew J Wilkinson. Note on Radar Signal Processing. University of Cape Town, October 2001.

[10] P. M. Woodward. Probability and Information Theory, with Application to Radar – Second Edition. Pergamon Press, 1964.

[11] Nicholas Currie. Radar Reflectivity Measurement: Techniques & Applications. Artech House, 1989.

[12] L. Alexander. The Planning of a South African Airborne Synthetic Aperture Radar Measuring Campaign. Master's thesis, Department of Electrical Engineering, University of Cape Town, 1994.

[13] S. A. Hovanessian. Radar System - Design and Analysis. Artech House, Norwood, MA, 1984

[14] Andrew J Wilkinson. SAR - Summary. University of Cape Town.

[15] Private Conversation to Dr. Andrew J Wilkinson

[16] Freek van Leijen. The Simulation of Radar Interferograms. Report of Internship at Radar Remote Sensing Group, Department of Electrical Engineering, University of Cape Town, January 2001.

[17] Andrew J Wilkinson. Short Note on the Projection from Slant Range to Ground Range. University of Cape Town, October 1999.

[18] Asoke K. Bhattacharyya and D. L. Sengupta. Radar Cross Section Analysis & Control. Artech House, 1991.

[19] Hui-Shun Kao. Radar Interferometry - 3D Height Reconstruction. Bachelor's Thesis, Department of Electrical Engineering, University of Cape Town, 2001.

[20] Amit Ashok. Implementation and Analysis of a Bayesian Approach to Topographic Reconstruction with Multiple Antenna Synthetic Aperture Radar Interferometry. Master's thesis, Department of Electrical Engineering, University of Cape Town, February 2000.

[21] These figures were provided by Shamiel Adams, Master of Science in Electrical Engineering, University of Cape Town.

[22] Goj. Walter W. Synthetic Aperture Radar and Electronic Warfare. Artech House, 1993.

[23] G. Franceschetti, M. Migliaccio, D. Riccio and G. Schirinzi. SARAS: A Synthetic Aperture Radar (SAR) Raw Signal Simulator. IEEE Transaction on Geoscience and Remote Sensing, 30(1): 110-123, January 1992.

[24] M. Gelautz, H. Frick, J. Raggam, J. Burgstaller and F. Leberl. SAR Image Simulation and Analysis of Alpine Terrain. ISPRS Journal of Photogrammetry and Remote Sensing, 53: 17-38, 1998.

[25] G. Franceschetti, M. Migliaccio and D. Riccio. On Ocean SAR Raw Signal Simulation. IEEE Transaction on Geoscience and Remote Sensing, 36(1): 84-100, January 1999.

[26] G. Domik and F. Leberl. Image Based SAR Product Simulation. In Proc. American Society of Photogrammetry and Remote Sensing, P355 – 364, 1987.

[27] R. Bamler and B. Schattler. Geocoding: ERS-1 SAR Data and Systems. P81, 1993.

[28] J. C. Curlander and R. N. McDonough. Synthetic Aperture Radar Systems and Signal Processing. P120-124, John Wiley & Sons, 1991.